

A STUDY OF PARAMETRIC EXCITATION APPLIED TO A MEMS TUNING FORK GYROSCOPE

A Dissertation
Presented to
the Faculty of the Graduate School
University of Missouri-Columbia

In Partial Fulfillment
of the Requirements for the Degree
Doctor of Philosophy

By
YONGSIK LEE

Dr. Frank Z. Feng, Dissertation Supervisor

AUGUST 2007

The undersigned, appointed by the Dean of the Graduate School, have examined the dissertation entitled

**A STUDY OF PARAMETRIC EXCITATION APPLIED
TO A MEMS TUNING FORK GYROSCOPE**

presented by Yongsik Lee

a candidate for the degree of Doctor of Philosophy

and hereby certify that in their opinion it is worthy of acceptance

Professor Dr. Frank Z. Feng

Professor Dr. Craig A. Kluever

Professor Dr. Yuyi Lin

Professor Dr. P. Frank Pai

Professor Dr. Tushar Ghosh

ACKNOWLEDGEMENTS

I would like to sincerely and wholeheartedly thank my advisor Dr. Frank Z. Feng for his close guidance, kindness, encouragements, patience, and supervision throughout various stages of the dissertation. Without his help and encouragement, this dissertation would not be possible.

I thank Dr. Craig A. Kluever, Dr. Yuyi Lin, Dr. P. Frank Pai, and Dr. Tushar Ghosh for making time in their busy schedules to serve on my dissertation committee, giving me advice, and examining my dissertation. Moreover, I would also like to thank Dr. P. Frank Pai for letting me use his experimental equipments and helping me to use them.

I wish to express my sincere thanks to Korea Army Headquarters for selecting me for the overseas study and supporting me and my family. Thanks are also due to Duck-bong, Su-han, Jung-woo, Mingxuan, and many others for their friendship and encouragement.

Most importantly, I would like thank my parents, my wife, Soon-ok, and my lovely kids, Chan-hee and Ye-rim, for their unconditional support, love, and affection. Their encouragement and endless love made everything easier to achieve. I really appreciate Soon-ok's patience and sacrifices that she made all this while. Also, my special thanks go to my mother who was really eager to see my homecoming but passed away last year. Even though she could not see me again, she will be memorized in my heart forever.

This work is supported by the National Science Foundation under Grant CMS0115828. The support is gratefully acknowledged.

TABLE OF CONTENTS

ACKNOWLEDGEMENTS	ii
LIST OF FIGURES	vii
LIST OF TABLES	xi
ABSTRACT	xii
Chapter 1 Introduction.....	1
1.1 MEMS Gyroscopes	1
1.2 Operation Principles of Vibratory Micro Gyroscope.....	4
1.3 Tuning Fork Micro Gyroscopes	5
1.4 Research Motivation	7
1.5 Literature Review	8
1.6 Overview	13
Chapter 2 Parametric Excitation	15
2.1 Introduction	15
2.2 Parametric Excitation	18
2.3 Mathieu Equation	20
2.4 Literature Review	22
2.5 Special Properties of the Parametric Excitation	24
2.6 Nonlinearities	25
Chapter 3 Feasibility Study of Parametric Excitation Using Pendulum Model.....	29

3.1	Dynamic Configuration.....	29
3.2	Dimensionless Equations	34
3.3	Results of Simulation	35
3.3.1	Dependence on Initial Condition.....	35
3.3.2	Effects of Imperfection.....	40
3.4	Effect of Stiffness of The Coupling Support.....	44
3.5	Summary	46
Chapter 4 Calculation of Coefficients Using Finite Element Method.....		47
4.1	Introduction	47
4.2	Critical Buckling Load Analysis	48
4.3	Effectiveness of Parametric Excitation	50
4.4	Derivation of the Nonlinear Term.....	53
4.5	Boundary Condition Effect	58
4.6	Comparison of Averaging Method and Simulation	60
4.7	Summary	66
Chapter 5 Experiments with a Tuning Fork Beam.....		67
5.1	Experimental Setup	67
5.2	Natural Frequencies and Mode Shapes	68
5.3	Experiment Method.....	70
5.3.1	The 3D Motion Analysis System	70
5.3.2	Eagle Digital Camera	72
5.3.3	Eagle Hub.....	74

5.3.4	EVaRT.....	74
5.3.5	Ling Dynamics LDS V408 Shaker.....	74
5.4	Experiment Procedure.....	74
5.5	Excitation Force Amplitude Scale.....	75
5.6	Experimental Results.....	76
5.6.1	Parametric Resonance Phenomenon	76
5.6.2	Swing in Symmetric Motion	79
5.6.3	Softening Nonlinearity	81
5.6.4	Damping Effect to the Base Beam	83
Chapter 6 Practical Problems		85
6.1	Limited Shaker Power.....	85
6.1.1	Dependence on Parameter c	89
6.1.2	Dependence on Parameter \bar{h}	90
6.1.3	Dependence on Parameter d	91
6.1.4	Comparison Between Experiment and Theory	92
6.2	Gravity Effect.....	99
6.2.1	Downward Pendulum.....	100
6.2.2	Inverted Pendulum	102
6.3	Summary	104
Chapter 7 Conclusions and Recommendation for Future Work		105
Appendix Parametrically excited pednulum by prescribed force amplitude.....		107
A.1	Equation of motion	107

A.2 Steady state response	109
A.3 Programs used in the simulation.....	116
A.3.1 Mathematica program for the analytic solution	116
A.3.2 MATLAB programs for the numerical solution	120
References	123
VITA	128

LIST OF FIGURES

Figure	Page
1. 1 Bandwidth in analog signals	3
1. 2 Operating principle of vibratory gyroscopes	5
1. 3 A tuning fork gyroscope with comb drive for commercial application by Draper Lab	6
2. 1 The classes of external resonance	17
2. 2 The classes of internal resonance.....	17
2. 3 Uniform rod pendulum oscillating as a result of giving the horizontal platform a harmonic vertical excitation.....	21
2. 4 Stable and unstable regions in the parameter plane for the Mathieu equation	22
3. 1 Schematic model of gyroscope motion.....	30
3. 2 Response of the pendulum when $m_1 = m_2$ and $l_1 = l_2$ (* : swing in the same direction, o : swing in the opposite direction, x : decaying).....	36
3. 3 Anti-Symmetric (in phase) motion ($\omega / \omega_1 = 1.85$)	37
3. 4 Symmetric (out of phase) motion ($\omega / \omega_1 = 2$)	37
3. 5 Anti-symmetric motion with symmetric IC ($\theta_1 = -\theta_2 = 0.05 \omega / \omega_1 = 1.85$).....	38
3. 6 Symmetric motion with asymmetric IC ($\theta_1 = \theta_2 = 0.05$, $\omega / \omega_1 = 2$).....	39
3. 7 The responses when $m_1 = m_2$ and $l_1 = l_2$: (a) Amplitudes of angular displace- ment of pendulums; (b) Displacement along the x-direction of the suspension mass; (c) Phase difference between the two pendulums	39
3. 8 Response of the pendulum when $m_1 = m_2$ and $0.95l_1 = l_2$ (* : swing in the same direction, o : swing in the opposite direction, x : decaying).....	41

3. 9	The responses when $m_1 = m_2$, $0.95l_1 = l_2$, $\gamma = 0.95$, $p = 0.23$: (a) Amplitudes of angular displacement of pendulums; (b) Displacement along the x-direction of the suspension mass; (c) Phase difference between the two pendulums	42
3. 10	The responses when $m_1 = m_2$, $0.95l_1 = l_2$, $\gamma = 0.95$, $p = 0.15$: (a) Amplitudes of angular displacement of pendulums; (b) Displacement along the x-direction of the suspension mass; (c) Phase difference between the two pendulums	43
3. 11	Response of the pendulum: $x=0$, $\gamma = 0.95$, $\theta_1 = 0.05$, $\theta_2 = -0.01$	45
3. 12	Response of the pendulum: $x=0$, $\gamma = 0.95$, $\theta_1 = 0.05$, $\theta_2 = 0.01$	45
4. 1	Cantilever beam with lumped load	49
4. 2	Cantilever beam with distributed load	49
4. 3	Relationship between natural frequency and axial force for the 1 st mode of the beam with the boundary condition clamped-free	52
4. 4	Relationship between natural frequency and axial force for the 2 nd mode of the beam with the boundary condition clamped-free	53
4. 5	Cantilever beam with parametric excitation	54
4. 6	Relationship between external load and displacement for the 1 st mode of the cantilever beam	56
4. 7	Relationship between external load and displacement for the 2 nd mode of the cantilever beam	57
4. 8	Relationship between natural frequency and axial force for the 1 st mode of the beam with the boundary condition clamped-clamped	59
4. 9	Relationship between natural frequency and axial force for the 2 nd mode of the beam with the boundary condition clamped-clamped	59
4. 10	Results of averaging method of the beam	63
4. 11	Pitchfork bifurcation at $\bar{a} = d$	64
4. 12	Displacement of the beam : Simulation result using Runge Kutta method	64

5. 1 Experimental model: (a) tuning fork type beam (b) reflection marks on the model .	67
5. 2 Natural frequencies and the mode shapes.....	69
5. 3 Experimental set up using EAGLE-500 digital real-time motion analysis system: (a) actual experimental set up (b) schematic set up of experiment.....	71
5. 4 Response at node #13 in vertical direction when $\Omega=80.40$ Hz and $a=-3$ dB (a) time trace (b) FFT	77
5. 5 Response at node #13 in horizontal direction when $\Omega=80.40$ Hz and $a=-3$ dB (a) time trace (b) FFT	78
5. 6 Time trace of the response at node #1 and # 25 when $\Omega=80.40$ Hz and $a=-3$ dB..	79
5. 7 Response curves at node #1 and # 25 when $a=0$ dB.....	80
5. 8 The swing patterns captured by a digital camera when the parametric force $a=0$ dB.....	80
5. 9 Experimental capture showing large displacement when 1 mm excitation is applied	81
5. 10 Response of the beam with different excitation amplitude at node #1	82
5. 11 Displacement of the base of the beam with different force amplitudes.....	83
6. 1 Results of averaging method of the beam : $\bar{a}=0.05$, $d=0.01$, $\bar{h}=-0.25$	87
6. 2 Dependence of the beam response on parameter c : $\bar{f}=0.02$ $d=0.01$ $\bar{h}=-0.35$	89
6. 3 Dependence of the beam response on parameter \bar{h} (when $\bar{h}>0$) : $\bar{f}=0.02$, $d=0.01$, $c=0.02$	90
6. 4 Dependence of the beam response on parameter \bar{h} (when $\bar{h}<0$) : $\bar{f}=0.02$, $d=0.01$, $c=0.005$	91
6. 5 Dependence of the beam response on parameter d : $\bar{f}=0.02$ $c=0.005$ $\bar{h}=-0.35$...	91

6. 6 Lateral vibration at the tip of the tine (a) and corresponding base excitation (b) when experimental force -6.0 dB and $\bar{f}=0.0040$	94
6. 7 Lateral vibration at the tip of the tine (a) and corresponding base excitation (b) when experimental force -4.5 dB and $\bar{f}=0.0048$	95
6. 8 Lateral vibration at the tip of the tine (a) and corresponding base excitation (b) when experimental force -3.0 dB and $\bar{f}=0.0056$	96
6. 9 Lateral vibration at the tip of the tine (a) and corresponding base excitation (b) when experimental force -1.5 dB and $\bar{f}=0.0068$	97
6. 10 Lateral vibration at the tip of the tine (a) and corresponding base excitation (b) when experimental force 0 dB and $\bar{f}=0.0080$	98
6. 11 Pendulum with spring	100
6. 12 Inverted pendulum with spring	103
A. 1 Simplified pendulum model.....	107
A. 2 the response of the pendulum with a large pendulum mass: $\rho=1$, $\zeta=0.05$, $\tilde{c}=0.1$, $k=0.01$, force amplitude =0.40 and 0.41.....	112
A. 3 the base acceleration amplitude when pendulums are swinging with a large pendulum mass: $\rho=1$, $\zeta=0.05$, $\tilde{c}=0.1$, $k=0.01$, force amplitude =0.40.....	112
A. 4 the base acceleration amplitude when pendulums are swinging with a large pendulum mass: $\rho=1$, $\zeta=0.05$, $\tilde{c}=0.1$, $k=0.01$, force amplitude =0.41.....	113
A. 5 the response of the pendulum with a small pendulum mass: $\rho=9$, $\zeta=0.05$, $\tilde{c}=0.1$, $k=0.01$, force amplitude =2.5.....	113
A. 6 the base acceleration amplitude when pendulums are swinging with a small pendulum mass: $\rho=9$, $\zeta=0.05$, $\tilde{c}=0.1$, $k=0.01$, force amplitude =2.5.....	114
A. 7 the MATLAB simulation results from the original equations used in Chapter 3; (a) pendulum displacement (b) base acceleration: $\alpha = \beta = 0.09$, $\zeta = 0.05$, $A = 0.25$	114

LIST OF TABLES

Table	Page
1. 1 Performance requirements for different classes of gyroscopes	1
1. 2 Resolution requirement of gyroscope for typical high performance application	9
4. 1 Buckling load of the beam	50
4. 2 Natural frequency with load stiffening for the 1 st mode	52
4. 3 Natural frequency with load stiffening for the 2 nd mode	53
4. 4 Displacement for several different horizontal forces using FEM	54
4. 5 Displacement when lateral uniform load was applied	56
4. 6 Two regression parameters and nonlinear term	57
5. 1 Material property of Aluminum 6061-T651	68
5. 2 Comparison of natural frequencies	70
5. 3 The ratio of the output voltage to the input voltage	76

A Study of Parametric Excitation Applied To A MEMS Tuning Fork Gyroscope

Yongsik Lee

Dr. Frank z. Feng, Dissertation Supervisor

ABSTRACT

The current MEMS (Micro-Electro-Mechanical System) gyroscopes which normally use the electro static force to excite the comb drive are faced with the limitations such as low precision, coupling problem, and poor robustness. They need an order of magnitude improvement in their performance, stability, and robustness. Our main idea is that if the comb drive can be driven to much larger vibrating amplitude than the current one so that the signal at the comb drive can be easily measured, then, consequently, the precision of the MEMS gyroscope shall be improved. We propose to use parametric forcing as excitation.

However, since the two proof masses must be driven into motion in opposite directions, this imposes restrictions on the external forcing. A feasibility study of the parametric excitation using a two-pendulum model is presented. Governing equations are derived by Lagrange equation, and the results are simulated using MATLAB program. Two swing patterns, symmetric and anti-symmetric motion, are illustrated and investigated with different initial conditions.

To predict the beam response with the parametric excitation, a novel approach is

presented, which allows calculating the coefficients in the governing equation of a cantilever beam using FEM (Finite Element Method). The results are compared with the analytical result obtained by method of averaging.

An experimental study of a tuning fork beam is presented. For non-contact motion analysis, an Eagle 3-D motion analysis digital camera system is employed. We discuss the practical problems such as limited shaker power, which is caused by open-loop excitation method. A governing equation including the damping effect by the lateral vibration of the tines is presented, and its analytical solution is compared with the experimental results. A good qualitative agreement is obtained. Moreover, a sensitivity study of the parameters in the governing equation is also presented. To clarify the softening nonlinearity of the tuning fork beam, the gravity effect is described for both vertical and inverted pendulum cases.

Chapter 1

Introduction

1.1 MEMS Gyroscopes

MEMS (Micro-Electro-Mechanical System) gyroscopes have many advantages such as low cost, small size, and negligible weight compared to the conventional mechanical gyroscopes. Furthermore, they have a wide range of applications including navigation and guidance systems, automobiles, and consumer electronics, so that many researchers have focused on them for the last decades. However, some drawbacks of the MEMS gyroscopes, such as low precision due to very small vibrating amplitude, very narrow bandwidth, and imperfection problem in fabrication are remaining challenges to be solved.

Yazdi, Ayazi, and Najafi [1] have given a review of the research on micro-machined vibratory gyroscopes. In general, gyroscopes can be classified into three categories based on their performance: inertial grade, tactical grade, and rate grade [2,3]. Table 1.1 summarizes the requirements for each of these categories.

Table 1. 1 Performance Requirements for Different Classes of Gyroscopes

Parameter	Rate Grade	Tactical Grade	Inertial Grade
Angle Random Walk ($^{\circ}/\sqrt{hr}$)	>0.5	0.5-0.05	<0.001
Bias Drift ($^{\circ}/hr$)	10-1000	0.1-10	<0.01
Scale Factor Accuracy (%)	0.1-1	0.01-0.1	<0.001
Full scale range($^{\circ}/s$)	50-1000	>500	>400
Max. Shock in 1ms ($g's$)	10^3	10^3 - 10^4	10^3
Bandwidth (Hz)	>70	~100	~100

For the past decade, much of the effort in developing micro-machined gyroscopes has concentrated on *rate grade* devices, primarily because of their use in automobile applications. This application requires a full scale range of at least 50 °/s and bias drift of 10-1000 °/hr in a bandwidth of 70 Hz. However, gyroscopes for the tactical grades or the inertial grades require improved performance such as a full scale range of 500 °/s and a bandwidth of 100 Hz. Bias drift for the inertial grades is even less than 0.01 °/hr.

In order to ensure the appropriateness of a gyroscope for a specific application, the application's performance requirements have to be fulfilled. This can be achieved in turn by quantifying the parameters or characteristics describing the performance of each particular inertial sensor through a series of lab tests. The most important among those characteristics are resolution, bias, scale factor, and bandwidth. [4]

Resolution

In the absence of rotation, the output signal of a gyroscope is a random function which is the sum of white noise and a slowly varying function. The white noise defines the resolution of the sensor and is expressed in $^{\circ}/s/\sqrt{Hz}$ or $^{\circ}/hr/\sqrt{Hz}$, which means the standard deviation of equivalent rotation rate per square root of bandwidth of detection. The so-called "angle random walk" in $^{\circ}/\sqrt{hr}$ may be used instead.

Bias

A sensor bias is always defined by two components: A deterministic component called *bias offset* which refers to the offset of the measurement provided by the sensor from the true input; and a stochastic component called *bias drift* which refers to the rate at which the error in an inertial sensor accumulates with time. The bias offset is deterministic and can be quantified by calibration while the bias drift is random in nature

and should be treated as a stochastic process. Bias drift is the short or long term drift of the gyroscope and is usually expressed in $^{\circ}/s$ or $^{\circ}/hr$.

Scale factor

The scale factor is the relationship between the output signal and the true physical quantity being measured. It is defined as the amount of change in the output voltage per unit change of rotation rate and is expressed in $V/^{\circ}/s$. The scale factor is deterministic in nature and can be quantified or determined through lab calibration.

Bandwidth

For analog signals, which can be mathematically viewed as a function of time, bandwidth Δf is the width, measured in hertz, of the frequency range in which the signal's Fourier transform is nonzero. As shown in Fig. 1.1, since this range of non-zero amplitude may be very broad, this definition is often relaxed so that the bandwidth is defined as the range of frequencies where the signal's Fourier transform has a power above a certain amplitude threshold, commonly half the maximum value (half power ≈ -3 dB, since $10\log_{10}(1/2) \approx -3$).

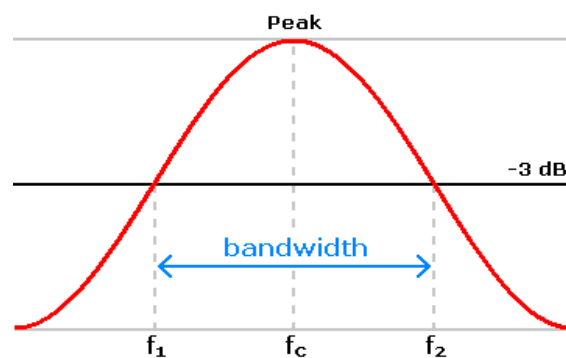


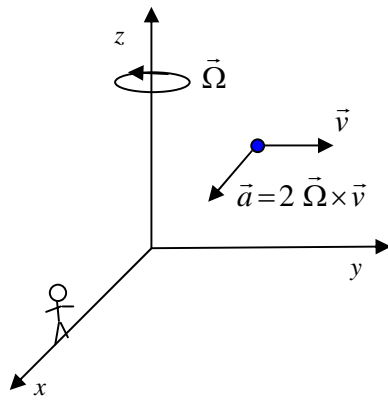
Figure 1. 1 Bandwidth in analog signals

As a result of active research in the past few years, “rate grade” gyroscopes have been developed successfully and applied in many commercial applications, such as automobiles and some consumer electronics. However, there are also several other applications that require improved performance, including inertial navigation systems, guidance weapon systems, and some precise robotics.

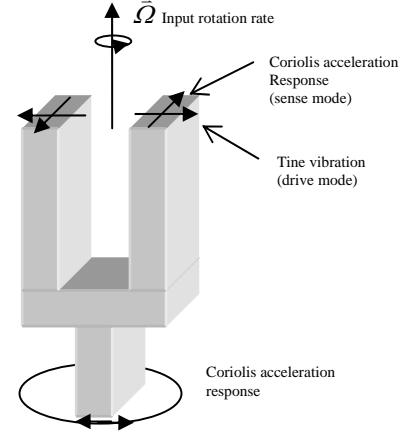
1.2 Operation Principles of Vibratory Micro Gyroscope

Vibratory micro-gyroscopes are non-rotating devices and use the Coriolis acceleration effect to detect inertial angular rotation. The Coriolis acceleration that arises in rotation reference frames to sense angular rotation is one of the accelerations that are used to describe motion in a rotating reference frame and accounts for radial motion. Its effects are found in many phenomena where rotation is involved and can even account for the air flow over the earth’s surface in the northern and southern hemispheres.

To understand the Coriolis effect, imagine a particle traveling in space with a velocity vector \vec{v} as illustrated in Fig. 1.2 (a). There is an observer who is sitting on the x -axis of the xyz coordinate system. If the coordinate system starts to rotate around the z -axis with an angular velocity, $\vec{\Omega}$, the observer thinks that the particle is changing its trajectory toward the x -axis with an acceleration equal to $2\vec{\Omega} \times \vec{v}$. Although no real force has been applied on the particle, to an observer, attached to the rotating reference frame an apparent force has resulted that is directly proportional to the rate of rotation. This effect is the basic operating principle underlying all vibratory structure gyroscopes.



(a) The Coriolis effect



(b) A tuning-fork gyroscope

Figure 1. 2 Operating principle of vibratory gyroscopes

Many researchers have designed vibratory micro gyroscopes which use Coriolis acceleration in the past decade. The vibratory micro gyroscopes normally fall into three categories: tuning fork micro gyroscope [5,6,7,8], vibrating prismatic beam gyroscope [9], and vibrating shell or ring gyroscope[10]. In this dissertation, the scope is limited to the tuning fork micro-gyroscope and we devote more space in the next section for better understanding.

1.3 Tuning Fork Micro Gyroscopes

Tuning fork gyroscopes are a typical example of vibratory gyroscopes. As shown in Fig. 1.2 (b), the tuning fork gyroscope consists of two tines that are connected to a junction bar. In operation, the tines are differentially resonated to a fixed amplitude, and when rotated, Coriolis force causes a differential sinusoidal force to develop on the individual tines, orthogonal to the main vibration. This force is detected either as differential bending of the tuning fork tines or as a torsional vibration of the tuning fork stem. The actuation mechanisms used for driving the vibrating structure into resonance

are primarily electrostatic, electromagnetic, or piezoelectric. To sense the Coriolis force in the sensing mode, capacitive, piezoresistive, or piezoelectric detection mechanisms can be used.

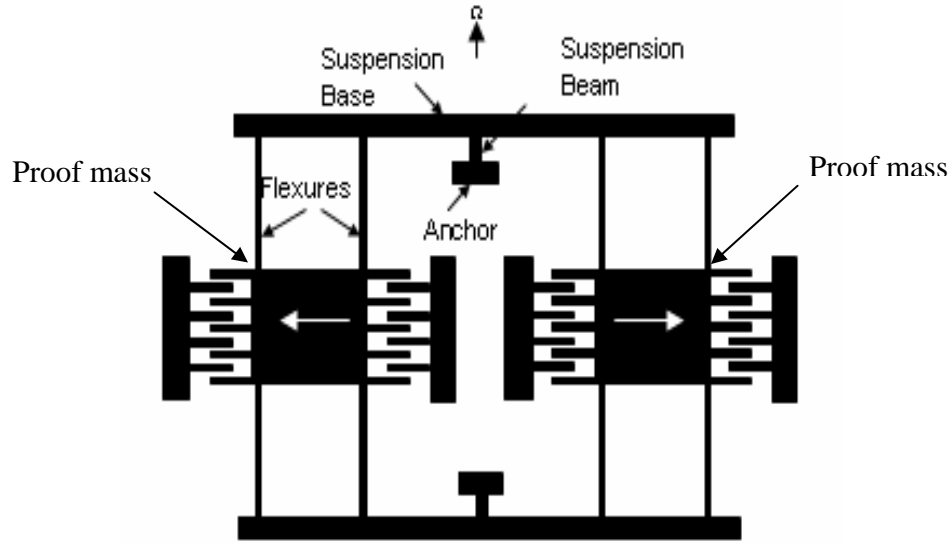


Figure 1. 3 A tuning fork gyroscope with comb drive for commercial application by Draper Lab

Draper Lab [6] proposed the first silicon micro machined vibratory rate gyroscope in 1991. In 1994, they developed micro gyroscope to the level of commercial applications [8]. As shown in Fig. 1.3, the two proof masses are driven into oscillations by the interdigitated fingers. Corresponding to an externally imposed angular rotation along the vertical axis, the Coriolis force on the two proof masses causes them to deflect in and out of the plane. The Coriolis force which is given by

$$\vec{F} = 2m\vec{\Omega} \times \vec{V}$$

where m denotes the proof mass, \vec{V} the velocity of the proof mass, and $\vec{\Omega}$ the angular velocity to be measured.

1.4 Research Motivation

The common factor of vibratory gyroscopes is that they require resonant frequency tuning of the driving and sensing modes to achieve high sensitivity. A number of studies have been performed to optimize those two frequencies. Xie and Fedder [11] designed a CMOS(complementary metal oxide semiconductor)-MEMS lateral-axis gyroscope using the out-of-plane actuation. They integrated a poly silicon heater inside the spring beams and realized the resonant frequency matching between the drive and sense modes.

These tuning conditions depend on each micro gyroscope fabricated, even though the micro gyroscopes are identically designed. Because of the small size of the structure and the limitation of the fabrication, the imperfection is unavoidable. Because of fabrication imperfections, significant errors can occur during the operation, which have to be compensated by advanced control techniques. Fabrication imperfections can also induce anisotropy, even though the imbalances in the gyroscope suspension are extremely small. This results in mechanical interference between the modes and undesired mode coupling are often much larger than the Coriolis motion. In order to reduce coupled oscillation and drift, various devices have been reported employing independent suspension beams for the drive and sense modes [12-16]. To increase the gyroscope's performance many researchers have studied various designs with different fabrication methods.

On the other hand, for the tuning fork gyroscope to work, the proof mass must be “energized,” that is, it must be driven into motion. Since the Coriolis force is proportional to the velocity, better sensitivity can be achieved by increasing the “driven” velocity of

the proof masses. However, electrostatic force through the interdigitated finger structure has a limitation to produce large velocity. Consequently, the current state of the micro machined gyroscopes requires an order of magnitude improvement in performance, stability, and robustness.

Our main idea is that if the comb drive can have bigger vibrating amplitude than previous one so that the signal at the comb drive can be easily measured, then the precision of MEMS gyroscopes can be much higher than the current one. We propose to drive the proof masses into oscillation using external means. Since the two proof masses must be driven into motion in opposite directions, this imposes restrictions on the external forcing. We propose to use parametric forcing as excitation. Imagine that the whole structure in Fig. 1.2 (b) which resides in a package is subjected to vibration along the direction of $\bar{\Omega}$. The direction of the forcing is perpendicular to the desired direction of motion of the proof masses. Based on the well-known parametric instability mechanism, the proof masses can be excited to vibrate in the desired direction (perpendicular to the forcing direction) when the forcing frequency is near twice of the natural frequency of the proof masses.

1.5 Literature Review

Inspired by the promising success of micro machined accelerometers in the same era, extensive research efforts towards commercial micro machined gyroscopes led to several innovative gyroscope topologies, fabrication and integration approaches, and detection techniques. Although there were extensive efforts from the researchers, the performance of the micro gyroscope is not enough to apply for some applications which

require high precision. Table 1.2 shows that there are some limitations with current technology in micro gyroscope for typical high performance applications.

Table 1. 2 Resolution requirement of gyroscope for typical high performance application [17]

Application	Resolution required (deg/hr)	Current capability of MEMS technology to provide this resolution
Inertial navigation	0.01 – 0.001	Impossible
Tactical weapon guidance	0.1 – 1.0	Impossible
Heading and altitude reference	0.1 - 10	Challenging

As mentioned prior, Greiff et al. [6] from Draper Lab reported the first micro machined gyroscope in 1991, utilizing double gimbal single crystal silicon structure suspended by torsional flexures. The resolution was $4^{\circ}/s/\sqrt{Hz}$ in a 60-Hz bandwidth. Since the first demonstration of micro machined gyroscope by the Draper Laboratory, a variety of micro-machined gyroscope designs fabricated in surface micromachining, bulk micromachining, hybrid surface bulk micromachining technologies or alternative fabrication techniques have been reported.

In 1993, Bernstein et al. [7] from Draper Lab reported an improved silicon-on-glass tuning fork gyroscope. The glass substrate is aimed at low stray capacitance. This gyroscope was electrostatically vibrated in its plane using a set of interdigitated comb drives. They could get the amplitude of 10 μm , and the performance was 1000 $^{\circ}/hr$ resolution and $1.52^{\circ}/\sqrt{hr}$ angle random walk in a 60 Hz bandwidth.

Weinberg et al. [8] from Draper Lab developed silicon-on-glass tuning fork gyroscope in 1994 for commercial application. A perforated mass was used to minimize damping. The in-plane motion of the structure is lightly damped by air, while out-of-

plane motion is strongly damped due to squeeze film effects. Therefore, for out-of-plane modes, Q rises rapidly when pressure is reduced, in contrast to the in-plane Q , which shows a small increase when the pressure drops. They reported $470^\circ/hr$ resolution in a 60 Hz bandwidth.

Clark et al. [18] used the integrated surface micromachining process to develop an integrated z axis gyroscope in 1996. In the paper, a resolution of $1^\circ/s/\sqrt{Hz}$ was demonstrated. They employed single proof mass driven into resonance in plane, and sensitive to Coriolis force in the in-plane orthogonal direction. Drive and sense modes were electrostatically tuned to match, and the quadrature error due to structural imperfections were compensated electro statically.

On the other hand, Juneau et al. [19] reported an xy dual axis gyroscope in 1997. The xy dual axis gyroscope with 2μ thick poly silicon rotor disc used torsional drive mode excitation and two orthogonal torsional sense modes to achieve resolution of $0.24^\circ/s/\sqrt{Hz}$.

In 1997, Lutz et al. [20] reported z axis micro machined tuning fork gyroscope design that utilizes electro magnetic drive and capacitive sensing for automotive applications, with resolution of $0.4^\circ/s/\sqrt{Hz}$. This device was fabricated using a combination of bulk and surface micro machining processes. Through the use of permanent magnet inside the sensor package, drive mode amplitudes in the order of 50 μm were achieved. Although such a large amplitude of oscillation can increase the output signal level, it increases total power consumption and may cause fatigue problems over long term operation.

Voss et al. [21] reported an SOI (Silicon-on-Insulator) based bulk micro machined tuning fork gyroscope with piezoelectric drive and piezo resistive detection in 1997. Piezoelectric aluminum nitride was deposited on one of the tines as the actuator layer, and the rotation induced shear stress in the step of the tuning fork was piezo resistively detected.

In 1998, Kourepenis et al. [22] from Draper Lab reported 10 μ m thick surface micro machined poly silicon gyroscope. The resolution was improved to $10^{\circ}/hr/\sqrt{Hz}$ at 60 Hz bandwidth in 1998, with temperature compensation and better control techniques.

In 1999, Mochida et al. [23] developed DRIE based 50 μ m thick bulk micro machined single crystal silicon gyroscope with independent beams for drive and detection modes, which aimed to minimize undesired coupling between the drive and sense modes. Resolution of $0.07^{\circ}/s/\sqrt{Hz}$ was demonstrated at 10 Hz bandwidth.

Park et al. [24] from Samsung demonstrated wafer level vacuum packaged 40 μ m thick bulk micro machined single crystal silicon sensor with mode decoupling in 2000, and reported resolution of $0.013^{\circ}/s/\sqrt{Hz}$.

Lee et al. [25] from Seoul National University reported hybrid surface bulk micromachining process in 2000. The device with 40 μ m thick single crystal silicon demonstrated resolution of $9^{\circ}/hr/\sqrt{Hz}$ at 100 Hz bandwidth.

Geiger et al. [26] reported in 2002 gyroscope with excellent structural decoupling of drive and sense modes, fabricated in the standard Bosch fabrication process featuring 10 μ m thick poly silicon structural layer. Resolution of $25^{\circ}/hr/\sqrt{Hz}$ with 100 Hz bandwidth was reported.

Geen et al. [27] developed dual resonator z axis gyroscope in 2002, fabricated in the iMEMS process with 4 μm thick poly silicon structural layer. The device utilized two identical proof masses driven into resonance in opposite directions to reject external linear accelerations, and the differential output of the two Coriolis signals was detected. On chip control and detection electronics provided self oscillation, phase control, demodulation and temperature compensation. This first commercial integrated micro machined gyroscope had measured noise floor of $0.05^\circ/\text{s}/\sqrt{\text{Hz}}$ at 100 Hz bandwidth.

In 2003, Xie and Fedder [28] demonstrated DRIE (deep reactive ion etching) CMOS (complementary metal oxide semiconductor) MEMS lateral axis gyroscope with measured noise floor of $0.02^\circ/\text{s}/\sqrt{\text{Hz}}$ at 5 Hz, fabricated by post CMOS micromachining that uses interconnect metal layers to mask the structural etch steps. The device employs combination of 1.8 μm thin film structures for springs with out of plane compliance and 60 μm bulk silicon structures defined by DRIE for the proof mass and springs with out of plane stiffness, with on chip CMOS circuitry. Complete etch removal of selective silicon regions provides electrical isolation of bulk silicon to obtain individually controllable comb fingers. Excessive curling is eliminated in the device, which was problematic in prior thin film CMOS MEMS gyroscopes.

1.6 Overview

In this dissertation, we study the parametric excitation which can be used to drive micro tuning fork gyroscope to increase the sensitivity. In Chapter 2, we briefly describe the categories of the resonance oscillations and the general information of the parametric excitation. Parametric excitation characteristics and nonlinearities are described as well as the history of the related research.

Feasibility study is implemented using parametrically excited pendulum model in Chapter 3. The governing equations of model are derived using Lagrange equation and simulation is carried out using the Runge-Kutta integration method. Initial condition dependence and imperfection problem are discussed also. The emphasis is on whether the two masses swing in the opposite direction or not.

In Chapter 4, we introduce a novel approach to get two unknown coefficients of the governing equation using ALGOR, a commercial program by which one can perform various structure analyses, and finite element method (FEM). In addition to the calculation of the coefficients, we obtain the analytical solutions using method of averaging and compare with numerical results.

An experimental study of the response of the tuning fork beam to the parametric excitation is presented in Chapter 5. A non-contact motion analysis system, Eagle 3-D motion analysis camera system, is introduced. Using this method, it is shown that the parametric excitation is a very effective way to increase the amplitude of the vibration, which may increase the sensitivity of the tuning fork gyroscope.

Practical problems are discussed in Chapter 6. We discuss the limited shaker power,

which led to open-loop control method for the shaker. An assumption is introduced, and the analytical solution based on the assumption is presented. We also investigate the sensitivities of the parameters in the governing equations. Moreover, gravity effect for the pendulum is studied both the normal and the inverted pendulums to explain discrepancies of nonlinear phenomenon shown in the experiments.

As a conclusion, in Chapter 7, we restate our contribution to the nonlinear and sensor communities. Also, future work is addressed briefly.

Chapter 2

Parametric Excitation

2.1 Introduction

In this chapter we briefly review the types of mechanical vibrations for a better understanding of parametric excitation. We classify the vibrations into several classes with respect to the relationship between the external forcing frequency and the natural frequencies of the structure. In fact, the dynamical analysis of the most real structures is based on multiple-degree-of-freedom models. Let us assume a general form of the equations of motion of a non-linear N -DOF structure.

$$M\ddot{\vec{x}} + C\dot{\vec{x}} + K\vec{x} + \vec{F}(\vec{x}) = \vec{P}_1(t) + P_2(t)\vec{x} \quad (2.1.1)$$

where, M is the mass matrix, C is the damping matrix, K is the stiffness matrix, and $\vec{F}(\vec{x})$ is the nonlinear vector embedded in the structure. The right side of the equation represents the external force acting on the structure. In Eq. (2.1.1), M , C , K , and $P_2(t)$ are $(N \times N)$ matrixes. On the other hand, the displacement vector $\vec{x}(t)$, nonlinear term $\vec{F}(\vec{x})$, and direct force vector $\vec{P}_1(t)$ are all $(N \times 1)$ vectors. Furthermore, the applied force vector $\vec{P}_1(t)$ and matrix $P_2(t)$ are periodic functions of time, $f_1 \cos \Omega_1 t$ and $f_2 \cos \Omega_2 t$ respectively.

First of all, in Eq. (2.1.1), if we have zero values for $\vec{P}_1(t)$ and $P_2(t)$, the vibration is called *free*. For the case, all the terms in the equation include the displacement vector $\vec{x}(t)$ or its derivatives, and the coefficients of the equation do not depend on time. Free

vibrations in a real system gradually decay because of the energy dissipation, and the system eventually comes to rest at an equilibrium position.

On the other hand, the vibration is called *forced* when one or more external periodic forces are applied to the system. In this case, the equation of motion can be expressed by a given periodic function of time. When the frequency of external periodic force is at certain frequency, the system oscillates in maximum amplitude, which is referred to as *resonance*. As shown in Fig. 2.1, the external resonance can be classified into three classes; *primary resonance*, *secondary resonance*, and *parametric resonance*.

In many mechanical systems, we focus on the primary resonance for which the frequency of the external force is close to one of the natural frequencies of the system. When one designs structures and mechanical systems, this phenomenon is either exploited or avoided. On the other hand, when a system has certain nonlinearities, the system may oscillate at a frequency different from the primary resonances, which is referred to as *secondary resonance*. It can be again divided into three categories depending on the relationship among the natural frequencies of the system; *sub-harmonic resonance*, *super-harmonic resonance*, and *super-sub-harmonic resonance* [29].

Another resonance besides primary and secondary resonances is *parametric resonance*. It occurs either by an external force or a periodic variation of some parameters of the system to which the motion of the system is sensitive. When the external force is applied for the parametric resonance, while external forcing direction is the same as the direction of oscillation in the primary and the secondary resonances, the forcing direction should be orthogonal to the direction of oscillation. The parametric resonance can be divided into two classes; *fundamental parametric resonance* and *principal parametric*

resonance. There will be more detailed explanation about the parametric excitation in the next section.

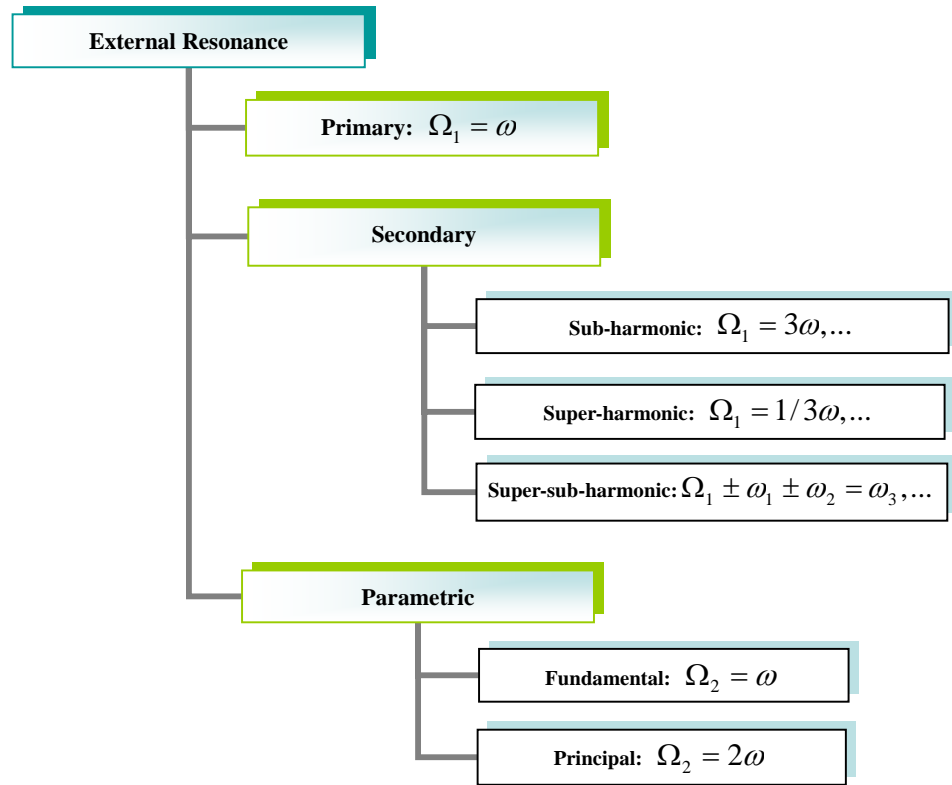


Figure 2. 1 The classes of external resonance

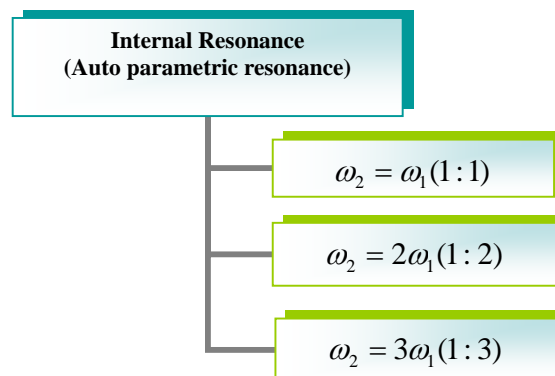


Figure 2. 2 The classes of internal resonance

In addition to the external resonances, there exists another resonance called *internal resonance*. It is often referred to as *auto-parametric resonance* because the system tends to be resonant by some specific relationship among the natural frequencies of the system. As shown in Fig. 2.2, when the natural frequencies have a simple integer ratio relationship, the energy transfer occurs from the high-frequency mode to the low-frequency mode [30].

2.2 Parametric Excitation

Nayfeh and Mook (1979) [29] and Butikov (2005) [42] gave detailed explanation about parametric excitation. Parametric excitation is quite different from normal direct force. All systems we are familiar with are modeled using equations in which the homogeneous part did not contain functions of time. Even if an excitation is introduced into the model, an external excitation is added to a system in a separate term. However, there are many systems for which this type of equation is not applicable. Let us assume a simple differential equation which contains time variable coefficients.

$$\ddot{x} + p_1(t)\dot{x} + p_2(t)x = f(t) \quad (2.2.1)$$

In Eq. (2.2.1), although the external excitation is set to zero, i.e., $f(t) = 0$, the time dependant terms in the equation can act as an excitation. Because this type of excitation acts from within the parameters of the system, as we already mentioned in section 2.1, it is usually referred to as *parametric excitation*. As shown in Eq. (2.2.1), parametric excitation can coexist with external excitation.

Equation (2.2.1) is linear, even though its coefficients are not constant, and its

general solution can be obtained by adding a particular solution of the complete equation to the general solution of the homogeneous equation. If $x_1(t)$ and $x_2(t)$ are two independent solutions of the homogeneous equation, its general solution can be obtained by the linear combination $x(t) = C_1 x_1(t) + C_2 x_2(t)$.

Consider a system modeled with a linear second-order differential equation of the type of Eq. (2.2.1) but without external excitation and with functions $p_1(t)$ and $p_2(t)$, which are periodic in time with period T . The study of equation of this type was published by Floquet in 1883, and, hence, is usually referred to as *Floquet theory*.

$$\ddot{x} + p_1(t)\dot{x} + p_2(t)x = 0 \quad (2.2.2)$$

By introducing the transformation

$$x = \tilde{x} \exp\left[-\frac{1}{2} \int p_1(t) dt\right]$$

Equation (2.2.2) can be rewritten as

$$\ddot{\tilde{x}} + p(t)\tilde{x} = 0 \quad (2.2.3)$$

where

$$p(t) = p_2 - \frac{1}{4} p_1^2 - \frac{1}{2} \dot{p}_1$$

For this transformation to be valid $p_1(t)$ is differentiable with respect to time.

This means that the free behavior of the damped system can be obtained from that of an undamped system by multiplying the time history of the latter by an appropriate decaying factor and slightly modifying the frequency by a change of the stiffness. It can be also applied for linear systems with constant parameter. Equation (2.2.3) is usually referred to as *Hill's equation*, because it was first studied by Hill in 1886 in the

determination of the perigee of lunar orbit. Vibrations in a system described by Hill's equation are called *parametrically excited* or simply *parametric*.

As we mentioned before, the responses from the parametrically excited systems are different from both *free* vibrations, which occur when the coefficients in the homogeneous differential equation of motion are constant, and *forced* vibrations, which occur when an additional time dependent forcing term is added to the right side of the equation of motion with constant coefficients. More detailed explanation about the characteristics of the parametric excitation will be addressed in Section 2.5.

The most common resonances in parametrically excited systems are the principal parametric resonance, which occurs when the excitation frequency is nearly equal to twice the natural frequency. We study the principal parametric resonance in this dissertation, in which we explore the governing equation using analytical and numerical method and prove by experiments.

2.3 Mathieu Equation

A particular form of Hill's equation is the Mathieu equation, for which

$$p(t) = \delta + 2\varepsilon \cos(2t) \quad (2.2.4)$$

Substituting Eq. (2.2.4) into Eq. (2.2.3) leads to

$$\ddot{x} + [\delta + 2\varepsilon \cos(2t)]x = 0. \quad (2.2.5)$$

The Mathieu equation governs the response of many physical systems to a sinusoidal parametric excitation. An example is a pendulum consisting of a uniform rod pinned at a point on a platform that is made to oscillate sinusoidally in the vertical direction as shown in Fig. 2.3.

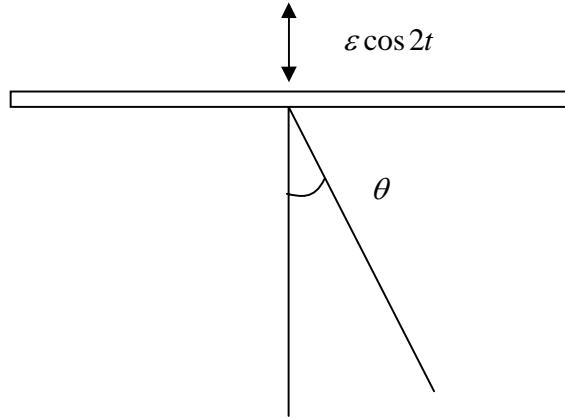


Figure 2. 3 Uniform rod pendulum oscillating as a result of giving the horizontal platform a harmonic vertical excitation [29]

Even though the Mathieu equation is a linear differential equation, it cannot be solved analytically in terms of standard functions. The reason is that one of the coefficients isn't constant but *time-dependent*. Fortunately, the coefficient is periodic in time. This allows applying the Floquet theorem. It says that in a linear differential equation there exists a set of *fundamental solutions* from which we can build all other solutions. Therefore, the solution of Eq. (2.2.5) can be written by

$$x(t) = \exp(\gamma t)\phi(t),$$

where γ is called a characteristic exponent and $\phi(t) = \phi(t + \pi)$. When the real part of one of the γ s is positive definite, x is unstable, which is unbounded with time, while when the real parts of all the γ s are zero or negative, x is stable, which is bounded with time. The vanishing of the real parts of the γ s separates stable from unstable motions. The loci of the corresponding values of ε and δ are called transition curves. They divide the ε - δ plane into regions corresponding to unstable motions and stable motions as shown in Fig. 2.4.

There are a number of techniques for determining the characteristic exponents and the transition curves separating stable from unstable motions. One method combines Floquet theory with a numerical integration of Eq. (2.2.5). To determine the transition curves by this technique, one divides the ε - δ plane into a grid and checks the solution at each grid point, which is quite a costly procedure. A second method involves the use of Hill's infinite determinant. When ε is small but finite, one can use perturbation methods such as the method of multiple scales and the method of averaging.

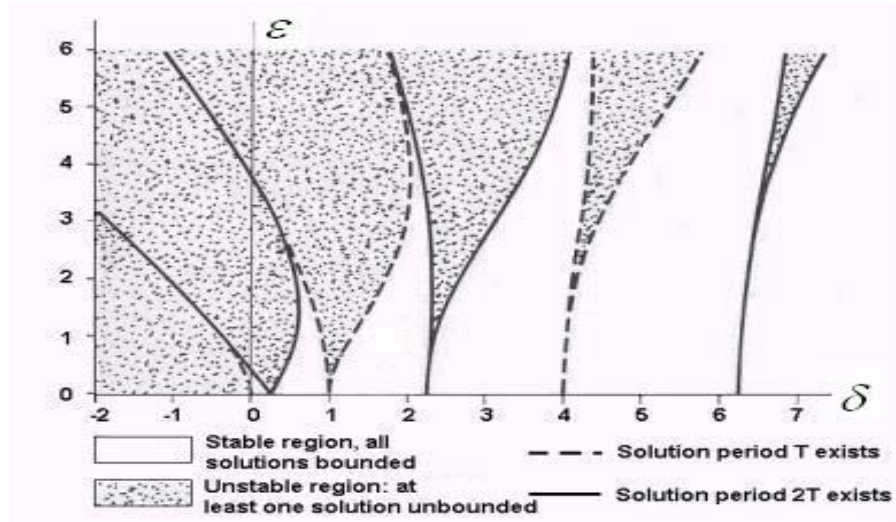


Figure 2. 4 Stable and unstable regions in the parameter plane for the Mathieu equation [29]

2.4 Literature Review

The observation of the first parametric resonance phenomenon goes back to 1831 as mentioned before. Faraday [31] observed that surface waves in a fluid in a vertically oscillating cylinder have one-half the frequency of the excitation.

Stephenson (1908) [32] pointed out that a column under the influence of a periodic load may be stable even though the steady value of the load is twice that of the Euler load.

Beliaev (1924) [33] analyzed the response of a straight elastic hinged-hinged column to an axial periodic load of the form $p(t) = p_0 + p_1 \cos \Omega t$. He obtained a Mathieu equation for the dynamic response of the column and determined the principal parametric resonance frequency of the column. The results show that a column can be made to oscillate with the frequency $\frac{1}{2}\Omega$ if it is close to one of the natural frequencies of the lateral motion even though the axial load may be below the static buckling load of the column.

Even though the history of the problem of parametric excitations is not too long, there are a number of books devoted to the analysis and applications of this problem. McLachlan (1947) [34] discussed the theory and applications of the Mathieu functions, while Bondarenko (1936) [35] and Magnus and Winkler (1966) [36] discussed Hill's equation and its applications in engineering vibration problems. Bolotin (1964) [37] discussed the influence of parametric resonances on the dynamic stability of elastic systems and Shtokalo (1961) [38] discussed linear differential equations with variable coefficients. Furthermore, a comprehensive review of the response of single and multi degree freedom systems to parametric excitations was discussed by Nayfeh and Mook [29] and Ibrahim [39].

M. Gürgöze [40] analyzed parametric vibrations of a restrained beam with an end mass under a displacement excitation at the other end. Using a one-mode approximation, he reduced the governing partial differential equation to a Mathieu equation containing cubic nonlinearities. He obtained an approximate solution for the case of principal parametric resonance.

Although there have been some papers regarding parametric excitation problem, only a few studies were performed to use parametric excitation to the practical system. Vyas and Bajaj [41] proposed auto parametric vibration absorbers which use multiple pendulums in 2001. The vibration of each pendulum can reduce the displacement of the primary system mass.

2.5 Special Properties of the Parametric Excitation

There are several important differences that distinguish parametric resonance from the ordinary resonance caused by external force acting directly on the system. Butikov (2005) [42] described the special characteristics of the parametric excitation in his paper.

The growth of the amplitude of the vibrations during parametric excitation is provided by the force that periodically changes the parameter. Parametric resonance is possible when one of the following conditions for the frequency ω (or for the period T) of modulation is fulfilled;

$$\omega = 2\omega_0 / n, \quad T = nT_0/2 \quad (n = 1, 2, 3, \dots).$$

In other words, parametric resonance occurs when the parameter changes twice during one period, once during one period, twice during three periods, and so on. However, the maximum energy transfer to the vibrating system occurs when the parameter is changed twice during one period of the natural frequency. In this dissertation, we are interested in the case, in which parametric force has the frequency of twice the natural frequency of the system.

Another important distinction between parametric excitation and forced vibration is the dependence of the growth of energy on the energy already stored in the system. While

for forced excitation the increment of energy during one period is proportional to the amplitude of vibrations, i.e., to the square root of the energy, at parametric resonance the increment of energy is proportional to the energy stored in the system. Also, energy losses caused by damping are also proportional to the energy already stored.

In the case of direct forced excitation energy losses restrict the growth of the amplitude because these losses grow with the energy faster than does the investment in energy arising from the work done by the external force. In the case of parametric resonance, both the investment in energy caused by the modulation of a parameter and the losses by damping are proportional to the energy stored, and so their ratio does not depend on the amplitude. Therefore, parametric resonance is possible only when a *threshold* is exceeded, that is, when the increment in energy during a period (caused by the parameter variation) is larger than the amount of energy dissipated during the same time. The critical (threshold) value of the modulation depth depends on damping. However, if the threshold is exceeded, the losses of energy by damping in a linear system cannot restrict the growth of the amplitude.

2.6 Nonlinearities

As mentioned earlier, parametrically excited linear, undamped systems have solutions that grow indefinitely with time. In other words, if the system is truly linear, the amplitude grows until the system is destroyed. Mandelstam and Papalexi (1934) [43] had proved this phenomenon by a specially designed linear oscillating circuit whose amplitude of oscillation grew until the insulation was destroyed by excessive voltage.

However, most systems have some degree of nonlinearity which comes into play as soon as the amplitude of the motion becomes appreciable, and it modifies the response. For instance, as the amplitude grows, the nonlinearity limits the growth, resulting in a limit cycle, as happened in the specially designed nonlinear oscillating circuit of Mandelstam and Papalexi (1934). Thus although the linear theory is useful in determining the initial growth or decay, it may be inadequate if the system possesses any nonlinearity. Hence, nonlinearity identification of the system is a very important problem.

In theory, nonlinearity exists in a system whenever there are products of dependent variables and their derivatives in the equations of motion, boundary conditions, and/or constitutive laws, and whenever there are any sort of discontinuities or jumps in the system. Evan-Iwanowski (1976) [30], Nayfeh and Mook (1979) [29], and Moon (1987) [44] explain the various types of nonlinearities in detail along with examples. Also, Pramod Malatkar (2003) [45] has briefly explained a variety of nonlinearities in his dissertation. Here are some nonlinearities that need to be considered when we design mechanical systems.

Damping dissipation is essentially a nonlinear phenomenon. Linear viscous damping is an idealization. Coulomb friction, aerodynamic drag, hysteretic damping, etc. are examples of nonlinear damping.

Geometric nonlinearity exists in systems undergoing large deformations or deflections. This nonlinearity arises from the potential energy of the system. In structures, large deformations usually result in nonlinear strain- and curvature-displacement

relations. This type of nonlinearity is present, for example, in the equation governing the large-angle motion of a simple pendulum, in the nonlinear strain-displacement relations due to mid-plane stretching in strings, and due to nonlinear curvature in cantilever beams.

Inertia nonlinearity derives from nonlinear terms containing velocities and/or accelerations in the equations of motion. It should be noted that nonlinear damping, which has similar terms, is different from nonlinear inertia. The kinetic energy of the system is the source of inertia nonlinearities. Examples include centripetal and Coriolis acceleration terms. It is also present in the equations describing the motion of an elastic pendulum (a mass attached to a spring) and those describing the transverse motion of an inextensional cantilever beam.

When the constitutive law relating the stresses and strains is nonlinear, we have the so-called material nonlinearity. Rubber is the classic example. Also, for metals, the nonlinear Ramberg-Osgood material model is used at elevated temperatures. The nonlinearity between stress and strain described by Ramberg and Osgood is as follows.

$$\varepsilon = \frac{\sigma}{E} + K\left(\frac{\sigma}{E}\right)^n$$

where ε is strain, σ is stress, E is Young's modulus, and K and n are constants that depend on the material being considered.

Nonlinearities can also appear in the boundary conditions. For example, a nonlinear boundary condition exists in the case of a pinned-free rod attached to a nonlinear torsional spring at the pinned end.

Many other types of nonlinearities exist: like the ones in systems with impacts, with backlash or play in their joints, etc. It is interesting to note that the majority of physical systems belong to the class of weakly nonlinear (or quasi-linear) system. For certain phenomena, these systems exhibit a behavior only slightly different from that of their linear counterpart. In addition, they also exhibit phenomena which do not exist in the linear domain. Therefore, for weakly nonlinear structures, the usual starting point is still the identification of the linear natural frequencies and mode shapes. Then, in the analysis, the dynamic response is usually described in terms of its linear natural frequencies and mode shapes. The effect of the small nonlinearities is seen in the equations governing the amplitude and phase of the structure response.

Chapter 3

Feasibility Study of Parametric Excitation Using Pendulum Model

3.1 Dynamic Configuration

Pendulum model is a good model to evaluate and simulate the dynamic responses of a tuning fork beam because it is simpler than a beam structure but has a good qualitative agreement with the beam dynamics.

For the tuning fork micro gyroscope to work, the two proof masses must be driven into oscillations in the opposite directions. We use parametrically excited pendulums as a model of a tuning fork micro gyroscope to explore the feasibility of exciting the symmetric mode of two coupled oscillators.

Our schematic model is shown in Fig. 3.1. Consider two pendulums hanging from a “suspension mass.” One particle having mass m_1 is connected to the massless rod whose length is l_1 and the other one is connected to l_2 . The external forcing along the vertical direction, $f(t)$, is on the suspension mass M . We define θ_1 and θ_2 as an angle of each pendulum and x and y as a displacement of the suspension mass along the horizontal and vertical direction, respectively. The suspension mass M is constrained along the horizontal direction and the vertical direction by the springs with the total spring constant k_x and k_y for each direction as shown in Fig. 3.1.

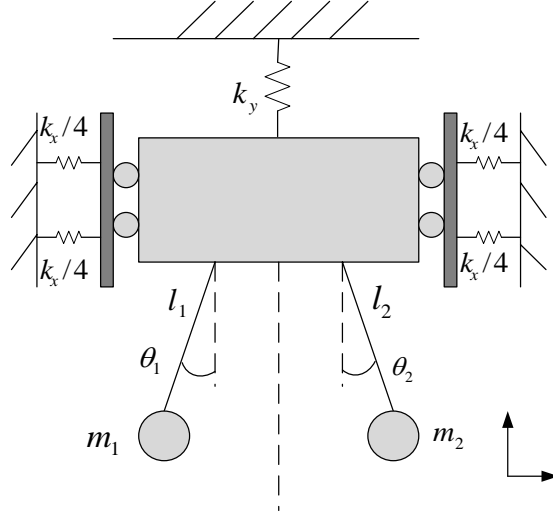


Figure 3. 1 Schematic model of gyroscope motion

The governing equations are derived by Lagrange equation that is

$$\frac{d}{dt} \left(\frac{\partial L}{\partial \dot{q}_i} \right) - \frac{\partial L}{\partial q_i} = Q_i \quad i = 1, 2, 3, \dots, n. \quad (3.1.1)$$

where $\dot{q}_i = \partial q_i / \partial t$ is the generalized velocity, L is the difference between the kinetic and potential energies, $L = (T - V)$, and Q_i represents all the non-conservative forces corresponding to q_i . For conservative systems, $Q_i = 0$ and equation (3.1.1) becomes

$$\frac{d}{dt} \left(\frac{\partial L}{\partial \dot{q}_i} \right) - \frac{\partial L}{\partial q_i} = 0 \quad i = 1, 2, 3, \dots, n. \quad (3.1.2)$$

Equations (3.1.1) and (3.1.2) represent one equation for each generalized coordinate. These expressions allow the equation of motion of complicated systems to be derived without using free-body diagrams and summing forces and moments.

We consider one part at a time for the calculation of kinetic energy and potential energy. To begin with, let us consider the suspension mass M . The kinetic energy T_M yields

$$T_M = \frac{1}{2} M v^2 = \frac{1}{2} M (\dot{x}^2 + \dot{y}^2) \quad (3.1.3)$$

In addition, the potential energy becomes

$$V_M = Mgy + \frac{k_y}{2} y^2 + \frac{1}{2} \left\{ \frac{k_x}{2} x^2 + \frac{k_x}{2} (-x)^2 \right\} = Mgy + \frac{k_y}{2} y^2 + \frac{k_x}{2} x^2 \quad (3.1.4)$$

The next part to be considered is a small particle having mass m_1 . In the same way as the suspension mass, the kinetic energy for mass m_1 can be expressed as

$$T_{m_1} = \frac{1}{2} m_1 v_1^2 \quad (3.1.5)$$

Because the particle is on the suspension mass, we need to consider the horizontal and vertical movement as well. We let $\vec{v}_1 = \vec{v} + \vec{\omega} \times \vec{r}$, where $\vec{\omega} = \dot{\theta}_1 \vec{k}$, and $\vec{r} = l_1 \sin \theta_1 \vec{i} - l_1 \cos \theta_1 \vec{j}$, we have

$$\begin{aligned} \vec{v}_1 &= \dot{x} \vec{i} + \dot{y} \vec{j} + l_1 \cos \theta_1 \dot{\theta}_1 \vec{i} + l_1 \sin \theta_1 \dot{\theta}_1 \vec{j} \\ &= (\dot{x} + l_1 \cos \theta_1 \dot{\theta}_1) \vec{i} + (\dot{y} + l_1 \sin \theta_1 \dot{\theta}_1) \vec{j} \end{aligned} \quad (3.1.6)$$

Substituting (3.1.6) into (3.1.5) leads to

$$\begin{aligned} T_{m_1} &= \frac{1}{2} m_1 \{ (\dot{x} + l_1 \cos \theta_1 \dot{\theta}_1)^2 + (l_1 \sin \theta_1 \dot{\theta}_1 + \dot{y})^2 \} \\ &= \frac{1}{2} m_1 \{ \dot{x}^2 + \dot{y}^2 + l_1^2 \dot{\theta}_1^2 + 2l_1 \dot{\theta}_1 (\cos \theta_1 \dot{x} + \sin \theta_1 \dot{y}) \} \end{aligned} \quad (3.1.7)$$

On the other hand, the potential energy for the pendulum yields

$$V_{m_1} = m_1 g y - m_1 g l_1 \cos \theta_1. \quad (3.1.8)$$

We get the equations for the other mass m_2 similarly

$$T_{m_2} = \frac{1}{2} m_2 \{ \dot{x}^2 + \dot{y}^2 + l_2^2 \dot{\theta}_2^2 + 2l_2 \dot{\theta}_2 (\cos \theta_2 \dot{x} + \sin \theta_2 \dot{y}) \} \quad (3.1.9)$$

$$V_{m_2} = m_2 g y - m_2 g l_2 \cos \theta_2 \quad (3.1.10)$$

Combining equations (3.1.3), (3.1.7), and (3.1.9) leads to the total kinetic energy of the system given by

$$\begin{aligned} T = & \frac{1}{2} M_t \dot{x}^2 + \frac{1}{2} M_t \dot{y}^2 + m_1 l_1 \dot{\theta}_1 (\cos \theta_1 \dot{x} + \sin \theta_1 \dot{y}) \\ & + m_2 l_2 \dot{\theta}_2 (\cos \theta_2 \dot{x} + \sin \theta_2 \dot{y}) + \frac{1}{2} (m_1 l_1^2 \dot{\theta}_1^2 + m_2 l_2^2 \dot{\theta}_2^2) \end{aligned} \quad (3.1.11)$$

where $M_t = M + m_1 + m_2$. Furthermore, the total potential energy V becomes

$$V = M_t g y - (m_1 l_1 \cos \theta_1 + m_2 l_2 \cos \theta_2) g + \frac{k_y}{2} y^2 + \frac{k_x}{2} x^2. \quad (3.1.12)$$

Lagrangian, L , from (3.1.1) becomes

$$\begin{aligned} L = & \frac{1}{2} M_t \dot{x}^2 + \frac{1}{2} M_t \dot{y}^2 + m_1 l_1 \dot{\theta}_1 (\cos \theta_1 \dot{x} + \sin \theta_1 \dot{y}) + m_2 l_2 \dot{\theta}_2 (\cos \theta_2 \dot{x} + \sin \theta_2 \dot{y}) \\ & + \frac{1}{2} (m_1 l_1^2 \dot{\theta}_1^2 + m_2 l_2^2 \dot{\theta}_2^2) - M_t g y + (m_1 l_1 \cos \theta_1 + m_2 l_2 \cos \theta_2) g - \frac{k_y}{2} y^2 - \frac{k_x}{2} x^2 \end{aligned} \quad (3.1.13)$$

From Eqs. (3.1.1) and (3.1.13), and if we let $q_1 = x$, $q_2 = y$, $q_3 = \theta_1$, $q_4 = \theta_2$, the governing equation for each variable can be obtained by simple algebraic steps.

For the case of $q_1 = x$,

$$\frac{\partial L}{\partial \dot{x}} = M_t \dot{x} + m_1 l_1 \dot{\theta}_1 \cos \theta_1 + m_2 l_2 \dot{\theta}_2 \cos \theta_2 \quad (3.1.14)$$

$$\frac{d}{dt} \left(\frac{\partial L}{\partial \dot{x}} \right) = M_t \ddot{x} + m_1 l_1 \cos \theta_1 \ddot{\theta}_1 - m_1 l_1 \sin \theta_1 \dot{\theta}_1^2 + m_2 l_2 \cos \theta_2 \ddot{\theta}_2 - m_2 l_2 \sin \theta_2 \dot{\theta}_2^2 \quad (3.1.15)$$

$$\frac{\partial L}{\partial x} = -k_x x \quad (3.1.16)$$

Substituting Eqs. (3.1.15) and (3.1.16) into Eq. (3.1.1) leads to the equation for x variable such as

$$M_t \ddot{x} + m_1 l_1 \cos \theta_1 \ddot{\theta}_1 - m_1 l_1 \sin \theta_1 \dot{\theta}_1^2 + m_2 l_2 \cos \theta_2 \ddot{\theta}_2 - m_2 l_2 \sin \theta_2 \dot{\theta}_2^2 + k_x x = Q_x \quad (3.1.17)$$

Next consider the case of $q_2 = y$.

$$\frac{\partial L}{\partial \dot{y}} = M_t \dot{y} + m_1 l_1 \dot{\theta}_1 \sin \theta_1 + m_2 l_2 \dot{\theta}_2 \sin \theta_2 \quad (3.1.18)$$

$$\frac{d}{dt} \left(\frac{\partial L}{\partial \dot{y}} \right) = M_t \ddot{y} + m_1 l_1 \sin \theta_1 \ddot{\theta}_1 + m_1 l_1 \cos \theta_1 \dot{\theta}_1^2 + m_2 l_2 \sin \theta_2 \ddot{\theta}_2 + m_2 l_2 \cos \theta_2 \dot{\theta}_2^2 \quad (3.1.19)$$

$$\frac{\partial L}{\partial y} = -M_t g - k_y y \quad (3.1.20)$$

Substituting Eqs. (3.1.19) through (3.1.20) into Eq. (3.1.1), we obtain the equation for y variable

$$M_t \ddot{y} + m_1 l_1 \sin \theta_1 \ddot{\theta}_1 + m_1 l_1 \cos \theta_1 \dot{\theta}_1^2 + m_2 l_2 \sin \theta_2 \ddot{\theta}_2 + m_2 l_2 \cos \theta_2 \dot{\theta}_2^2 + M_t g + k_y y = Q_y \quad (3.1.21)$$

If we let $q_3 = \theta_1$,

$$\frac{\partial L}{\partial \dot{\theta}_1} = m_1 l_1 (\cos \theta_1 \dot{x} + \sin \theta_1 \dot{y}) + m_1 l_1^2 \dot{\theta}_1 \quad (3.1.22)$$

$$\frac{d}{dt} \left(\frac{\partial L}{\partial \dot{\theta}_1} \right) = m_1 l_1 \cos \theta_1 \ddot{x} + m_1 l_1 \sin \theta_1 \ddot{y} - m_1 l_1 \sin \theta_1 \dot{\theta}_1 \dot{x} + m_1 l_1 \cos \theta_1 \dot{\theta}_1 \dot{y} + m_1 l_1^2 \ddot{\theta}_1 \quad (3.1.23)$$

$$\frac{\partial L}{\partial \theta_1} = -m_1 l_1 \sin \theta_1 \dot{\theta}_1 \dot{x} + m_1 l_1 \cos \theta_1 \dot{\theta}_1 \dot{y} - m_1 g l_1 \sin \theta_1 \quad (3.1.24)$$

Substituting the equation (3.1.23) through (3.1.24) into (3.1.1) leads to

$$m_1 l_1 \cos \theta_1 \ddot{x} + m_1 l_1 \sin \theta_1 \ddot{y} + m_1 l_1^2 \ddot{\theta}_1 + m_1 g l_1 \sin \theta_1 = Q_{\theta_1} \quad (3.1.25)$$

In the same way we obtain the equation for θ_2 variable such as

$$m_2 l_2 \cos \theta_2 \ddot{x} + m_2 l_2 \sin \theta_2 \ddot{y} + m_2 l_2^2 \ddot{\theta}_2 + m_2 g l_2 \sin \theta_2 = Q_{\theta_2} \quad (3.1.26)$$

We assume that the suspension mass is driven into sinusoidal oscillations along the y -direction. Thus we let

$$\ddot{y} = a \cos \omega t \quad (3.1.27)$$

Substituting (3.1.27) into (3.1.17), (3.1.21), (3.1.25), and (3.1.26) leads to the equations of motion for the three remaining degrees-of-freedom. Moreover, if we assume generalized forces acting on the system in the form of viscous damping, we obtain

$$M_t \ddot{x} + m_1 l_1 \cos \theta_1 \ddot{\theta}_1 - m_1 l_1 \sin \theta_1 \dot{\theta}_1^2 + m_2 l_2 \cos \theta_2 \ddot{\theta}_2 - m_2 l_2 \sin \theta_2 \dot{\theta}_2^2 + c_x \dot{x} + kx = 0 \quad (3.1.28)$$

$$m_1 l_1 \cos \theta_1 \ddot{x} + m_1 l_1^2 \ddot{\theta}_1 + m_1 l_1 \sin \theta_1 a \cos \omega t + c_1 \dot{\theta}_1 + m_1 g l_1 \sin \theta_1 = 0 \quad (3.1.29)$$

$$m_2 l_2 \cos \theta_2 \ddot{x} + m_2 l_2^2 \ddot{\theta}_2 + m_2 l_2 \sin \theta_2 a \cos \omega t + c_2 \dot{\theta}_2 + m_2 g l_2 \sin \theta_2 = 0 \quad (3.1.30)$$

From the equations, each damping term can be described as

$$c_x = 2\zeta M_t \omega_x, \quad c_1 = 2\zeta m_1 l_1^2 \omega_1, \quad c_2 = 2\zeta m_2 l_2^2 \omega_2 \quad (3.1.31)$$

where ζ denotes damping ratio and $\omega_x = \sqrt{\frac{k}{M_t}}$, $\omega_1 = \sqrt{\frac{g}{l_1}}$, $\omega_2 = \sqrt{\frac{g}{l_2}}$.

3.2 Dimensionless Equations

The equations obtained in the previous section can be written in dimensionless forms by letting l_1 be a characteristic length and $\frac{1}{\omega_1}$ be a characteristic time,

$$x = l_1 \tilde{x} \quad \text{and} \quad t = \frac{\tilde{t}}{\omega_1}, \quad (3.2.1)$$

$$\text{thus, the derivatives become } \ddot{x} = \omega_1^2 l_1 \tilde{x}'' , \quad \ddot{\theta}_1 = \omega_1^2 \tilde{\theta}_1'' , \quad \ddot{\theta}_2 = \omega_1^2 \tilde{\theta}_2'' \quad (3.2.2)$$

where, $\tilde{x}'' = \frac{d^2 \tilde{x}}{d\tilde{t}^2}$ and $\tilde{\theta}'' = \frac{d^2 \tilde{\theta}}{d\tilde{t}^2}$, respectively.

Substituting (3.2.1) and (3.2.2) into (3.1.27) through (3.1.29) leads to

$$M_t \omega_1^2 l_1 \tilde{x}'' + m_1 \omega_1^2 l_1 \cos \theta_1 \tilde{\theta}_1'' + m_2 \omega_1^2 l_2 \cos \theta_2 \tilde{\theta}_2'' + 2\zeta M_t \sqrt{\frac{k}{M_t}} \omega_1 l_1 \tilde{x}' - m_1 \omega_1^2 l_1 \sin \theta_1 \tilde{\theta}_1'^2 - m_2 \omega_1^2 l_2 \sin \theta_2 \tilde{\theta}_2'^2 + k l_1 \tilde{x} = 0 \quad (3.2.3)$$

$$m_1 \omega_1^2 l_1^2 \cos \theta_1 \tilde{x}'' + m_1 \omega_1^2 l_1^2 \tilde{\theta}_1'' + 2\zeta m_1 \omega_1^2 l_1^2 \tilde{\theta}_1' + m_1 l_1 \sin \theta_1 (a \cos \frac{\omega}{\omega_1} \tilde{t} + g) = 0 \quad (3.2.4)$$

$$m_2 \omega_1^2 l_1 l_2 \cos \theta_2 \tilde{x}'' + m_2 \omega_1^2 l_2^2 \tilde{\theta}_2'' + 2\zeta m_2 l_2^2 \omega_1 \omega_2 \tilde{\theta}_2' + m_2 l_2 \sin \theta_2 (a \cos \frac{\omega}{\omega_1} \tilde{t} + g) = 0 \quad (3.2.5)$$

Simplifying (3.2.3) through (3.2.5), we obtain the final equations in dimensionless form such as

$$\tilde{x}'' + \alpha \cos \theta_1 \tilde{\theta}_1'' + \beta \gamma \cos \theta_2 \tilde{\theta}_2'' + 2\zeta \frac{\omega_x}{\omega_1} \tilde{x}' - \alpha \sin \theta_1 \tilde{\theta}_1'^2 - \beta \gamma \sin \theta_2 \tilde{\theta}_2'^2 + \frac{\omega_x^2}{\omega_1^2} \tilde{x} = 0 \quad (3.2.6)$$

$$\cos \theta_1 \tilde{x}'' + \tilde{\theta}_1'' + 2\zeta \tilde{\theta}_1' + \sin \theta_1 (p \cos \omega_r \tilde{t} + 1) = 0 \quad (3.2.7)$$

$$\frac{1}{\gamma} \cos \theta_2 \tilde{x}'' + \tilde{\theta}_2'' + 2\zeta \frac{\omega_2}{\omega_1} \tilde{\theta}_2' + \frac{\omega_2^2}{\omega_1^2} \sin \theta_2 (p \cos \omega_r \tilde{t} + 1) = 0 \quad (3.2.8)$$

where, $\alpha = \frac{m_1}{M_t}$, $\beta = \frac{m_2}{M_t}$, $\gamma = \frac{l_2}{l_1}$, $\omega_1 = \sqrt{\frac{g}{l_1}}$, $\omega_2 = \sqrt{\frac{g}{l_2}}$, $\omega_x = \sqrt{\frac{k}{M_t}}$, $\omega_r = \frac{\omega}{\omega_1}$, $p = \frac{a}{g}$.

3.3 Results of Simulation

3.3.1 Dependence on Initial Condition

In this section we explore the dynamic responses of a symmetric structure. The dimensionless parameters used are the following:

$$\alpha = \beta = 0.09, \quad \gamma = 1, \quad 1.75 < \omega / \omega_1 < 2.15, \quad 0.06 < p < 0.25$$

where, α and β denote ratio of each pendulum mass to the base mass respectively, γ is the length ratio between the two pendulums, ω / ω_1 is the ratio of the excitation

frequency to the natural frequency of the pendulum, and p is the ratio of y direction acceleration to the gravity force g .

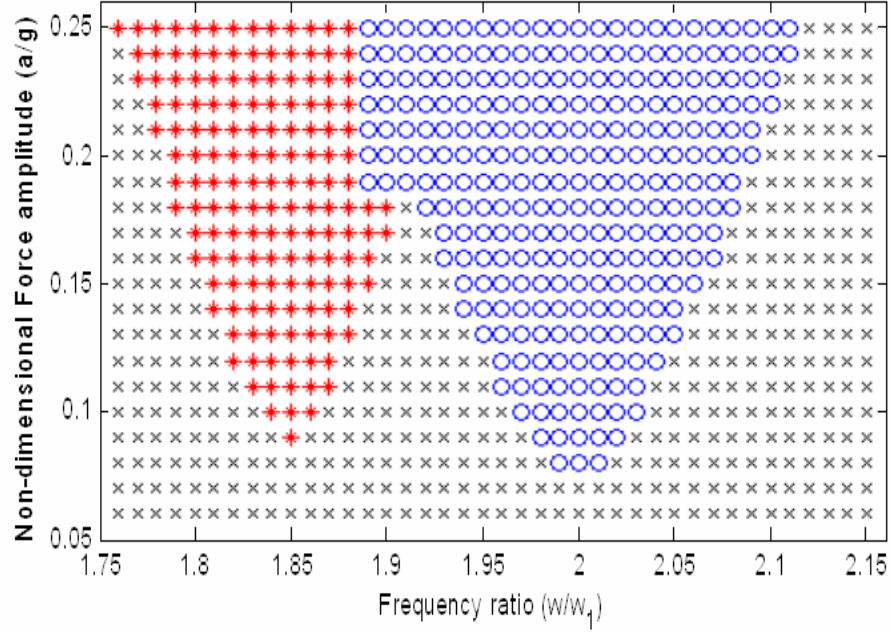


Figure 3. 2 Response of the pendulum when $m_1 = m_2$ and $l_1 = l_2$
 (* : swing in the same direction, o : swing in the opposite direction, x : decaying)

As shown in Fig. 3.2, the parametric resonance occurs when the forcing frequency is near twice the natural frequency of the pendulum. There exist three types of pendulum responses depending on the forcing frequency and amplitude. In the figure, ‘o’ marks represent the pendulum motions swinging in the opposite directions. The ‘*’ marks denote the pendulum motions which are swinging in the same direction, and the ‘x’ marks represent the pendulum motions which decay after some transient. We refer to the motion when the two pendulums move in the opposite direction with the same amplitude as *symmetric* or *out-of-phase motion*. On the other hand, we refer to the swing motion when the two pendulums swing in the same direction as *anti-symmetric* or *in-phase motion*. The border of the two types of swing motions experiences long transient time to

reach the steady state.

The parametric resonance occurs when the amplitude of dimensionless excitation p is greater than 0.07. When it is smaller than 0.07, the response dies out after some transient time.

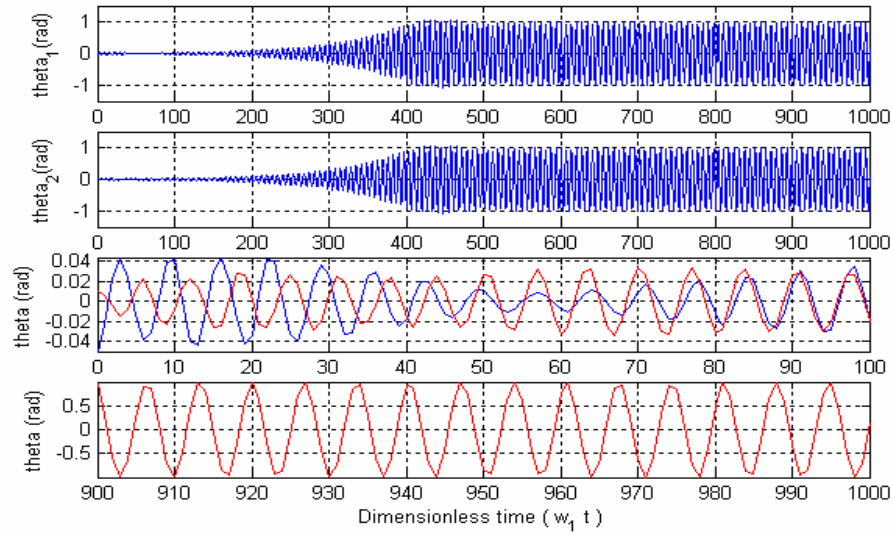


Figure 3. 3 Anti-Symmetric (in phase) motion ($\omega / \omega_1 = 1.85$)

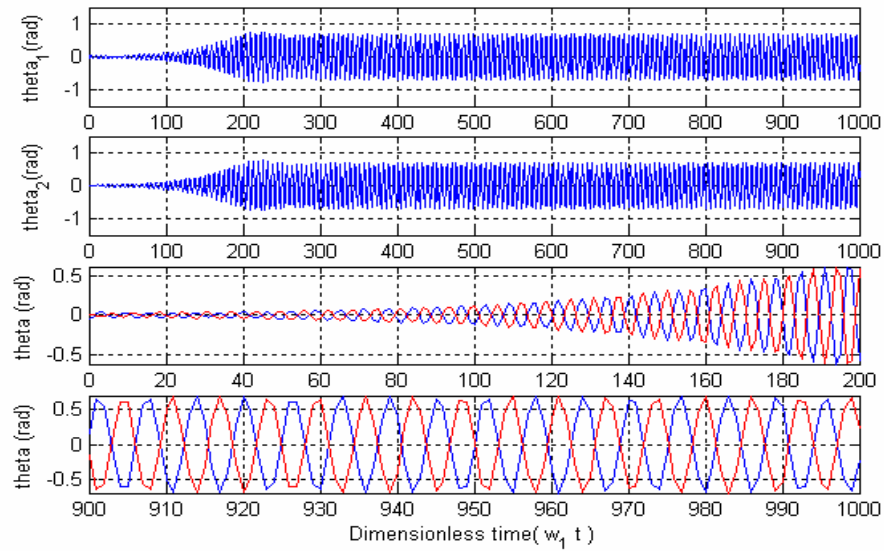


Figure 3. 4 Symmetric (out of phase) motion ($\omega / \omega_1 = 2$)

Figures 3.3 and 3.4 show that the two types of pendulum motions in more detail. The two figures are obtained by applying the same forcing amplitude, $p=0.15$, and the same initial conditions, $\theta_1 = -0.05 \text{ rad}$, $\theta_2 = 0.01 \text{ rad}$. From the figures, it is clear that the steady-state pendulum response is dictated by the frequency ratio rather than by initial condition. This observation summarizes the outcomes of several simulations we have conducted.

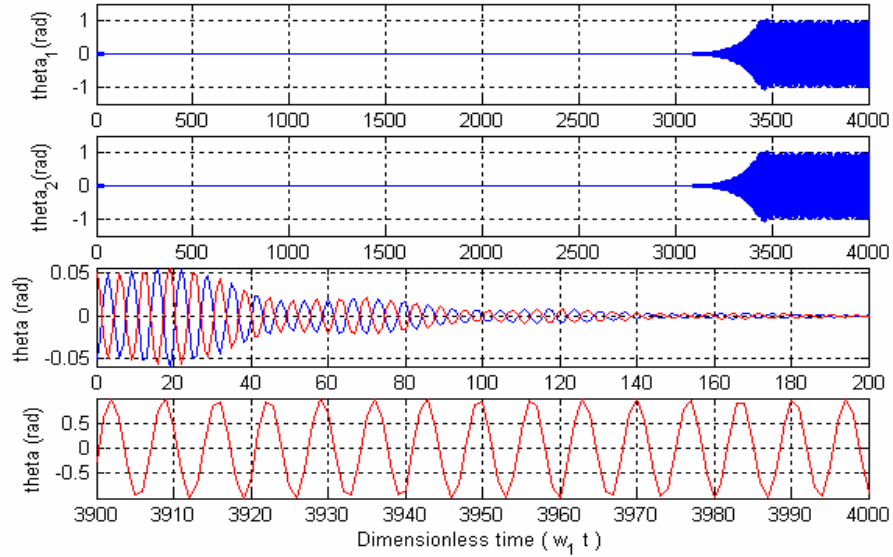


Figure 3. 5 Anti-symmetric motion with symmetric IC ($\theta_1 = -\theta_2 = 0.05 \text{ rad}$, $\omega / \omega_1 = 1.85$)

Most interestingly, we have used symmetric initial conditions to start the simulation which evolves into asymmetric steady-state. This is shown in Fig. 3.5, which is obtained for the forcing frequency ratio $\omega / \omega_1 = 1.85$ with the symmetric initial condition $\theta_1 = -\theta_2 = 0.05 \text{ rad}$. The response becomes anti-symmetric (in-phase) motion after a long transient. A similar case with anti-symmetric initial conditions $\theta_1 = \theta_2 = 0.05 \text{ rad}$ is seen to evolve into symmetric motions after a long transient in Fig. 3.6.

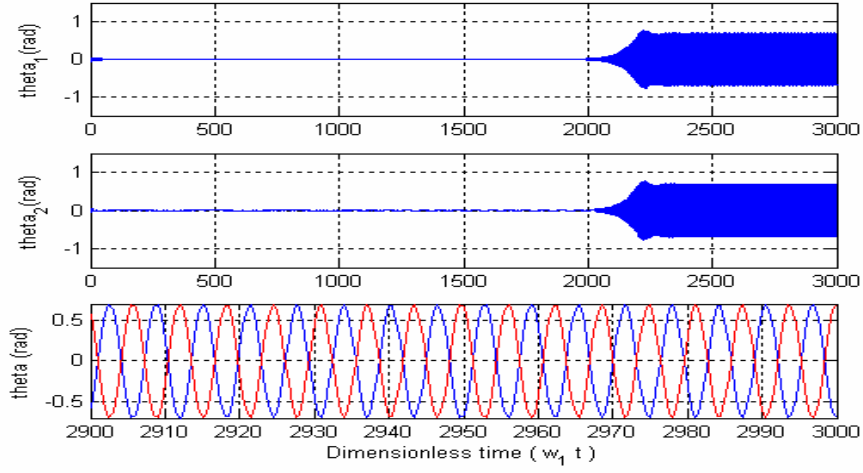


Figure 3. 6 Symmetric motion with asymmetric IC ($\theta_1 = \theta_2 = 0.05 \text{ rad}$, $\omega/\omega_1 = 2$)

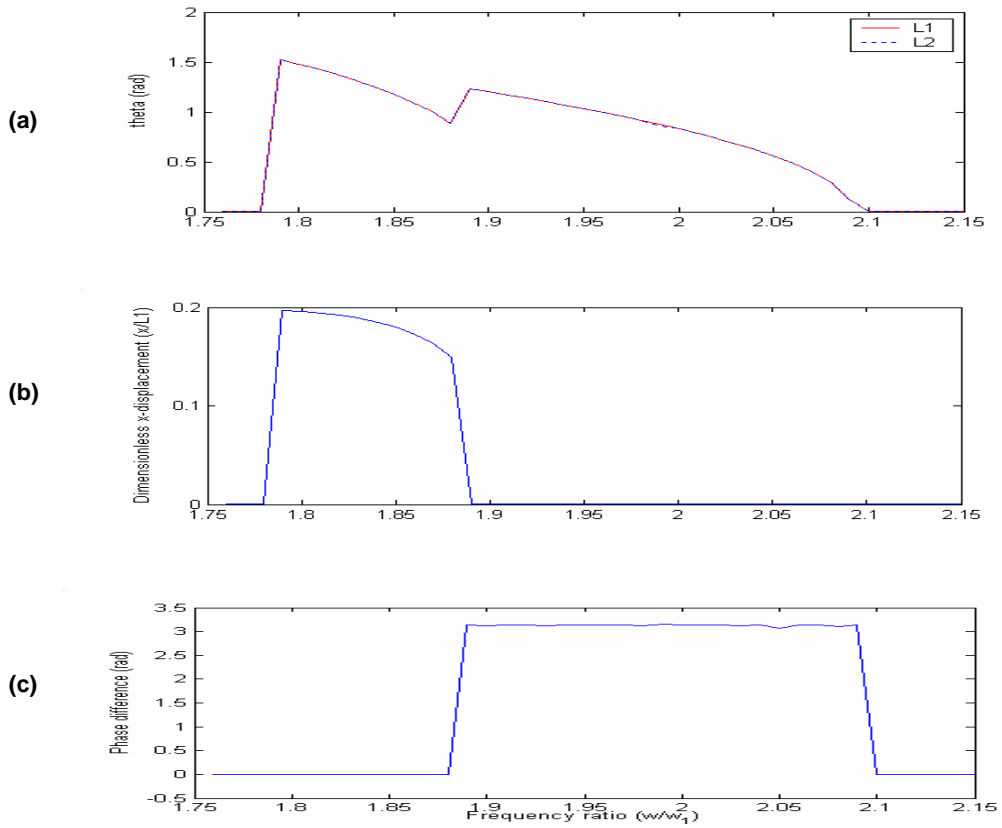


Figure 3. 7 The responses when $m_1 = m_2$ and $l_1 = l_2$: (a) Amplitudes of angular displacement of pendulums; (b) Displacement along the x-direction of the suspension mass; (c) Phase difference between the two pendulums

Figure 3.7(a) shows the amplitudes of the angular displacements of the two pendulums when they reach the steady state. The parameters used are as follows; $p=0.15$, initial conditions are $\theta_1 = -0.05 \text{ rad}$ and $\theta_2 = 0.01 \text{ rad}$. The displacement along the x-direction of the suspension mass is shown in Fig. 3.7 (b). The phase angle difference between the two pendulums is shown in Fig. 3.7 (c). The curves for the amplitudes of the two pendulums exactly overlap in Fig. 3.7 (a). The displacement along the x-direction of the suspension mass is zero when the pendulum motions have a phase difference of $\pi \text{ rad}$. That is, the suspension mass does not move in the x-direction when the motion is symmetric. The phase difference is zero when the motion is anti-symmetric. In this case, large displacement occurs in x-direction.

3.3.2 Effects of Imperfection

The study in Section 3.3 demonstrates the feasibility of using parametric excitation to generate symmetric oscillations of two identical pendulums. Our interest is to use similar parametric excitations in micro gyroscopes. One important aspect of micro gyroscope fabrication is the dimensional inaccuracy of the fabricated parts. The dimensional inaccuracy breaks the symmetry of the mechanical structure. In order to understand whether the above findings are still valid in the presence of imperfections of the mechanical structure, we study the response of the two pendulums whose lengths are slightly different. The dimensionless parameters used are the following:

$$\alpha = \beta = 0.09, \quad \gamma = 0.95, \quad 1.75 < \omega/\omega_1 < 2.15, \quad 0.06 < p < 0.25$$

Because of the length difference, each pendulum shows different magnitude of swing angle. However, the swing patterns are the same as the previous simulation in

which the two pendulums have the same mass and the same length. The two different swing patterns, *symmetric motion* and *anti-symmetric motion*, are clearly noticed. In the same way, ‘*’ symbols in Fig. 3.8 represent the anti-symmetric motion and ‘o’ symbols represent the symmetric motion.

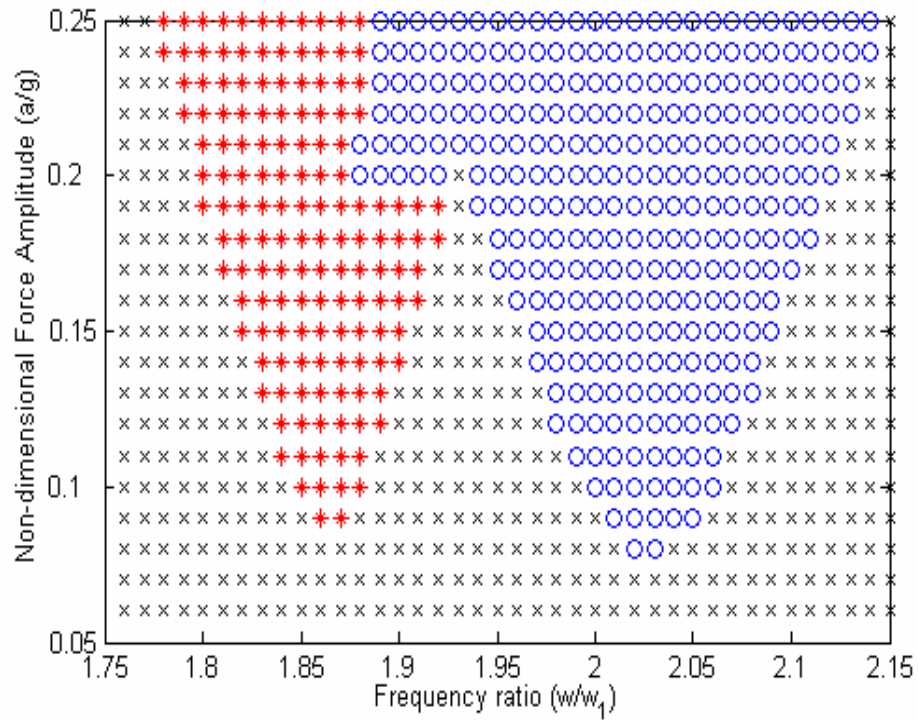


Figure 3. 8 Response of the pendulum when $m_1 = m_2$ and $0.95l_1 = l_2$
 (* : swing in the same direction, o : swing in the opposite direction, x : decaying)

Figure 3.9 was obtained with the parameters, $\gamma = 0.95$, $p = 0.23$, and the initial condition, $\theta_1 = -0.05 \text{ rad}$ and $\theta_2 = 0.01 \text{ rad}$. Recall that $\gamma = 1$ represents the case that the two pendulums are hung by the same length of massless rod. In Fig. 3.8, however, the lengths of the rods for two pendulums are no longer identical, so that the geometric symmetry is broken. The amplitudes of the two pendulums are never exactly

the same. Consequently, the displacement along the x -direction of the suspension mass cannot be zero. Still, we notice that there exist forcing parameters for which the pendulums swing in the opposite directions (phase angle is close to $\pi \text{ rad}$) and the amplitudes of the approximately “*symmetric motions*” are close to each other.

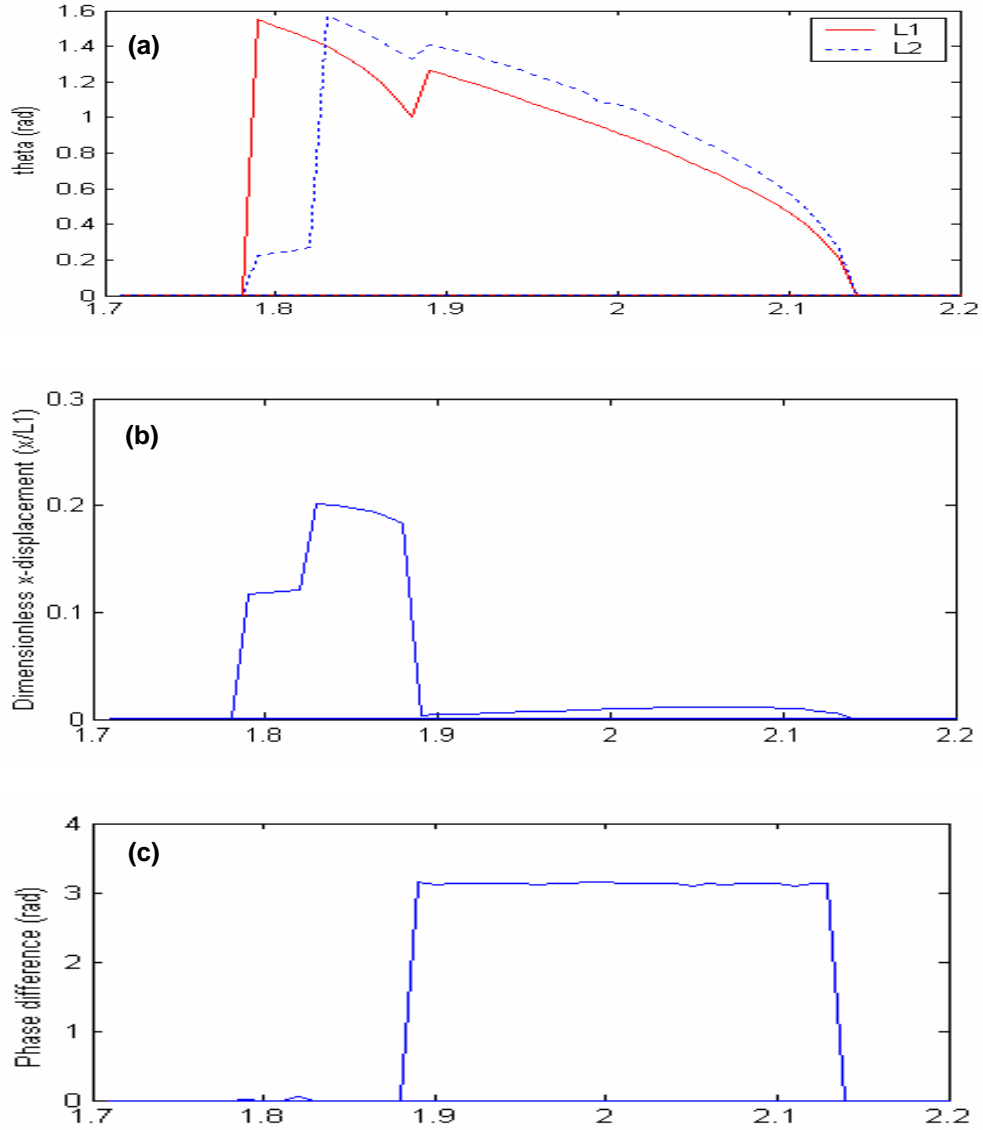


Figure 3. 9 The responses when $m_1 = m_2, 0.95l_1 = l_2, \gamma = 0.95, p = 0.23$: (a) Amplitudes of angular displacement of pendulums; (b) Displacement along the x -direction of the suspension mass; (c) Phase difference between the two pendulums

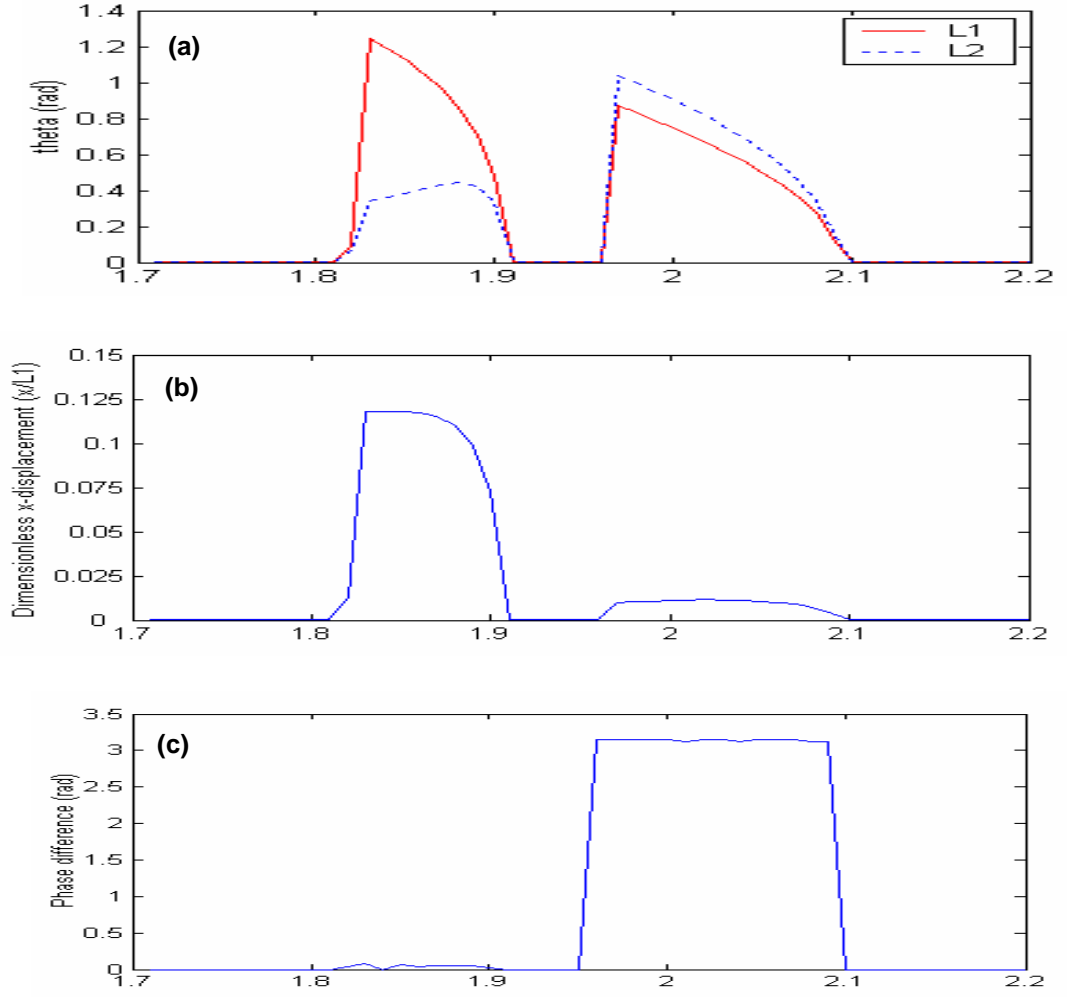


Figure 3. 10 The responses when $m_1 = m_2$, $0.95l_1 = l_2$, $\gamma = 0.95$, $p = 0.15$: (a) Amplitudes of angular displacement of pendulums; (b) Displacement along the x-direction of the suspension mass; (c) Phase difference between the two pendulums

Figure 3.10 is the case in which all the parameters are identical to those of Fig. 3.9 except the forcing amplitude, $p = 0.15$, which is smaller than the one in the previous study. At this forcing amplitude, there exists a frequency interval where the pendulums are not excited. This frequency interval separates the two frequency regions where the pendulums undergo steady oscillations under parametric excitations. When forced by a

frequency in the high frequency region, the pendulums oscillate in the opposite directions. In this case, pendulum motions are approximately “*symmetric*.” In addition, a forcing frequency in the low frequency region makes the pendulums oscillate in the same directions, *anti-symmetric*.

As shown in Figs. 3.9 and 3.10, the displacement of the pendulum swing is much more complicated when they move in the same direction than when they swing in the opposite direction. In other words, there are small displacement differences when they swing in the opposite direction, but if they swing in the same direction, the displacement gap between the two pendulums is increased.

3.4 Effect of Stiffness of the Coupling Support

In the previous section, we noticed that the pendulum swing depends on the frequency rather than the initial condition. As shown in Figs. 3.9 and 3.10, the stiffness of the x direction allows coupling between the two pendulums and hence energy transfer occurs between them.

However, when the x displacement of the support is constrained to be zero, there is no coupling between the two pendulums. In this case, shown in Figs. 3.11 and 3.12, the only thing that regulates the pendulum’s movement is initial condition. So if the initial condition is in the opposite direction, the swing reaches in the opposite direction at steady state and if the initial condition is in the same direction, then the swing is also in the same direction at steady state.

Figure 3.11 was obtained from the frequency range in which the pendulums are supposed to swing in *in-phase motion*. Frequency ratio, $\omega / \omega_1 = 1.85$, and the initial

condition, $\theta_1 = 0.05 \text{ rad}$ and $\theta_2 = -0.01 \text{ rad}$, were applied. However, x -direction movement was constrained completely. As shown in Fig. 3. 11, the two pendulums swing in *out-of-phase motion* unlike the previous simulation.

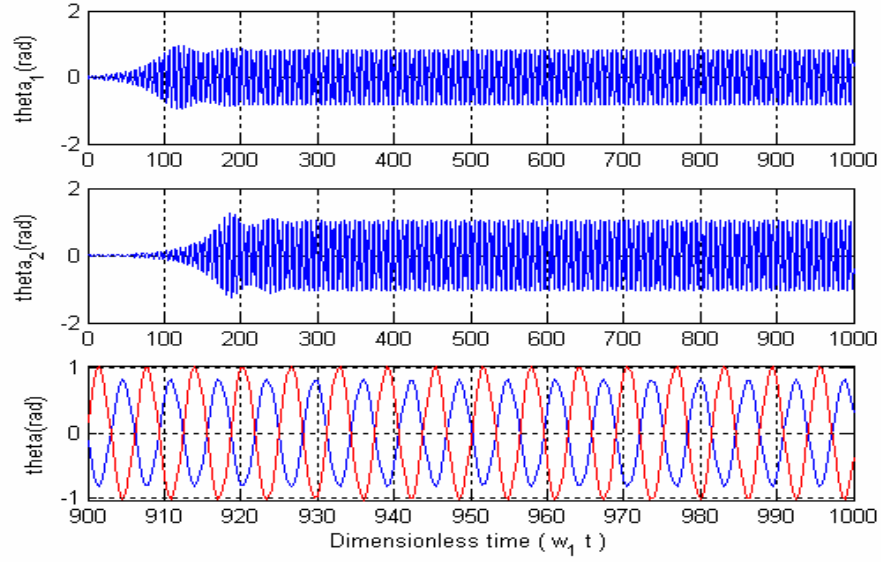


Figure 3. 11 Response of the pendulum: $x=0$, $\gamma = 0.95$, $\theta_1 = 0.05 \text{ rad}$, $\theta_2 = -0.01 \text{ rad}$

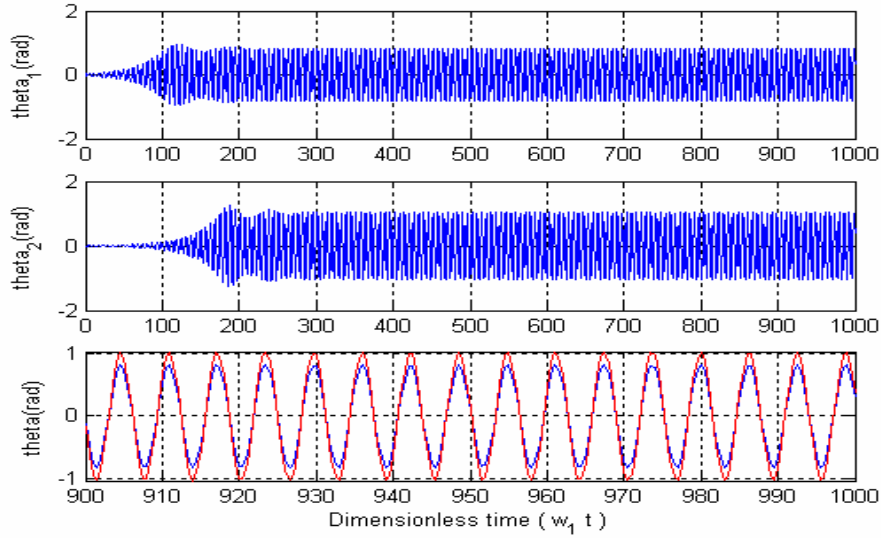


Figure 3. 12 Response of the pendulum: $x=0$, $\gamma = 0.95$, $\theta_1 = 0.05 \text{ rad}$, $\theta_2 = 0.01 \text{ rad}$

Figure 3.12 shows another example of the initial condition dependence. At this time, it was obtained from the frequency range in which the pendulum supposed to swing in the opposite direction (*out-of-phase*) motion. Frequency ratio, $\omega/\omega_1 = 2$, and the initial condition, $\theta_1 = 0.05 \text{ rad}$ and $\theta_2 = 0.01 \text{ rad}$, were used. In the same way, x direction movement was constrained. We see that the two pendulums swing in the same direction as the initial direction in Fig. 3.12.

This work is closely related to Ref. [41]. The main difference lies in the finite stiffness along the x -direction in our model. The coupling along the x -direction excludes the possibility that only one pendulum is excited at a time. However if we have very large stiffness, k , then the pendulums are decoupled completely and each pendulum follows the parametric excitation rule independently.

3.5 Summary

We studied the response of two coupled pendulums to show the feasibility of the external excitation for the micro gyroscope. We found that the system has two different swing patterns. The solution with the opposite direction allows excitation of the desired mode. This solution persists for structures with imperfection. This is advantageous for device fabrication since imperfection is unavoidable.

Our numerical study has shown that parametric excitation can cause the two pendulums to oscillate in the opposite directions stably. This property can be used to design MEMS micro gyroscopes which use parametrical forcing as excitation. The design is shown to be robust to imperfections that are unavoidable in device fabrication.

Chapter 4

Calculation of Coefficients Using Finite Element Method

4.1 Introduction

The advantage of the parametric excitation is that it can be externalized. The fabrication is thus simplified. However, there are no readily applicable tools to guide the design of these gyroscopes since the gyro structures are more complex than those structures whose responses to parametric excitations are known and since finite element analysis tools are not capable of studying parametric excitations. In this work, we adopt a novel approach to obtain a simplified model of the parametrically excited structure. Parameters in the simplified model are obtained using dynamic analysis capability of typical finite element programs and static nonlinear analysis capabilities. Nayfeh and Pai studied non-linear non-planar parametric responses of an inextensional beam in 1989 and they got analytical formula [46].

Consider a parametrically excited beam. If the forcing frequency is close to twice that of the first mode, the governing equation for the beam vibration can be written as

$$\ddot{\delta} + 2\omega_0 \zeta \dot{\delta} + \omega_0^2 (1 - \alpha \frac{P}{B_L}) \delta + \frac{h}{m} \delta^3 = 0 \quad (4.1.1)$$

where ω_0 is the natural frequency of the beam, ζ the damping coefficient, P the

parametric excitation force, m the modal mass, h the nonlinear term, and B_L the static buckling limit. The coefficient α is an important parameter that measures the effectiveness of the parametric excitation. The nonlinear coefficient h measures the geometric nonlinearity in the system.

The concept of a parametrically excited micro gyroscope is that by parametric excitation, i.e. $P = f \cos(2\omega t)$, sufficient motion is generated. For Equation (4.1.1), the steady state amplitude of δ is determined by ζ , α , and h . The parameter ζ is often known in terms of the Quality Factor, $Q = \frac{1}{2\zeta}$. However, there is no analytical method to calculate this parameter. It is often determined using empirical data.

4.2 Critical Buckling Load Analysis

The critical buckling load is the maximum load that a structure can support prior to structural instability or collapse. The collapse of the structure is reached when the displacements become relatively large for a small load increment. The critical buckling load is different depending on the boundary condition of the structure.

As shown in Fig. 4.1, if we have a cantilever beam with one end fixed and the other end free, the buckling load when axial load applies on the free end is described as

$$B_L = \frac{\pi^2 E I n^2}{4l^2} \quad n=1,2,3\ldots \quad (4.2.1)$$

where E denotes the Young's modulus, I is the moment of inertia, and l is the length of the beam [47].

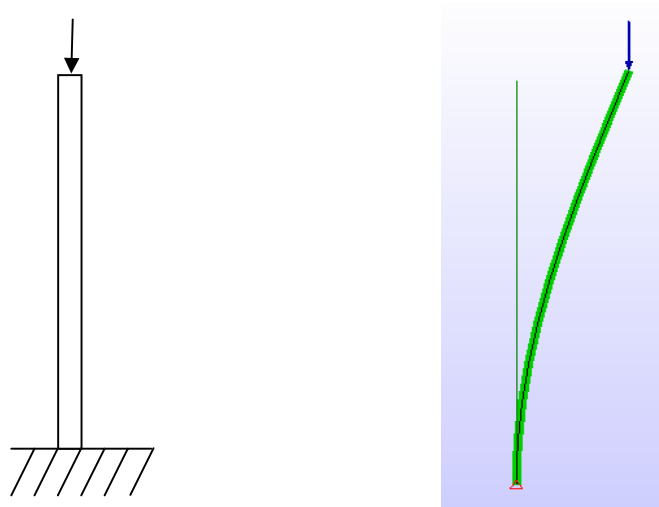


Figure 4. 1 Cantilever beam with lumped load

However, if we have a cantilever beam supplied by vertical direction excitation, axial force will be induced by its own mass as shown in Fig. 4.2. We assume that lumped mass is distributed on each node and it produces axial force on the beam. Also, clamped-free boundary condition is assumed.

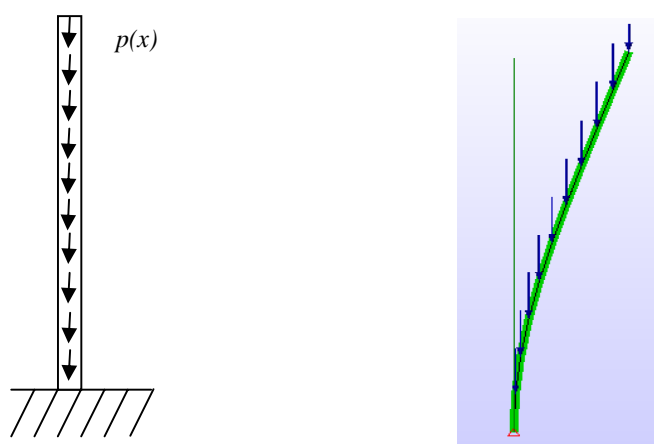


Figure 4. 2 Cantilever beam with distributed load

The critical buckling load yields

$$B_L = \frac{7.837 E I n^2}{l^2} \quad n=1,2,3... \quad (4.2.2)$$

by the study of Timoshenko in 1961.

We used Al(6061-T6) cantilever beam $10\text{cm} \times 0.1\text{cm} \times 0.1\text{cm}$ in size. Young's modulus, E , was 69.637 GPa. For the finite element analysis, the beam was divided into 10 elements as shown in Fig.4.2. We found that the critical buckling load of the beam was 454,546 dyn in theory and 452,872 dyn from ALGOR analysis [48]. The error between the theory and the simulation was only 0.37 %.

Table 4. 1 Buckling load of the beam

	Theory (dyn)	Simulation (dyn)	Error (%)
First mode	454,546	452,872	0.37
Second mode	1,818,184	-	-

Even though we can calculate the critical buckling load for the second mode by the theory, the first mode's one is still assumed to be more important in the practical system. For that reason, ALGOR simulation may give only one bucking load.

4.3 Effectiveness of Parametric Excitation

ALGOR is one of the commercial programs to analyze dynamics of structures using finite element method (FEM). The natural frequency with load stiffening processor in the program is used when axial compressive or tensile loads will affect the response of a system. This analysis type is very similar to the natural frequency processor. However, it can handle a situation when a part is under compression or tension at the same time that

vibration is induced. For instance, a violin or guitar string's tone is changed when the string is tightened or loosened even though nothing is done to the string to change its mass or length. This effect makes music possible and engineers call it *load stiffening*.

Natural frequency is changed until the structure buckles. When a structure buckles under the compression the natural frequency becomes zero. Using this phenomenon, one can calculate the relationship between the natural frequency with and without axial load.

From Eq. (4.1.1), we know the relationship between two natural frequencies with and without the axial load:

$$\omega^2 = \omega_0^2 \left(1 - \alpha \frac{P}{B_L}\right) \quad (4.3.1)$$

where ω denotes the natural frequency of the beam with axial force, and ω_0 is the natural frequency of the beam without axial force. P and B_L are the axial force acting on the beam and the critical buckling load of the beam respectively. Table 4.2 is the simulation results of the *Natural frequency with load stiffening* analysis.

Table 4.2 shows that the first natural frequency is decreased while the axial force is increased. Moreover, the squared natural frequency term is a linear function of the axial load P so that it reaches down to zero when the axial load becomes the same as the critical buckling load. As shown in Fig. 4.3, the linear equation gives the coefficient, $\alpha = 1$.

Table 4. 2 Natural frequency with load stiffening for the 1st mode

Load P (dyn)	ω (rad/s)	Load P (dyn)	ω (rad/s)
0	512.70	300000	298.31
50000	483.68	400000	175.52
100000	452.78	450000	40.92
200000	383.47	452000	22.54

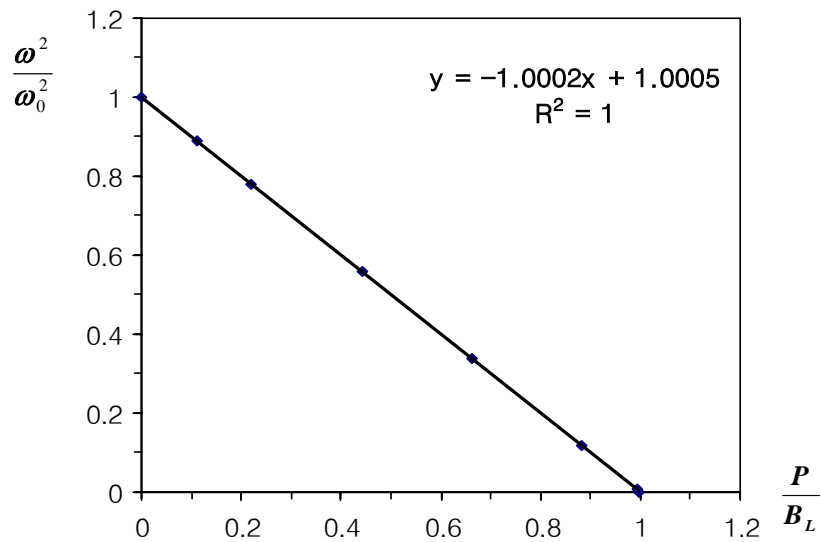


Figure 4. 3 Relationship between natural frequency and axial force for the 1st mode of the beam with clamped-free boundary condition

On the other hand, the simulation shows that the second mode frequency also has a linear relationship with axial load P . The results of the natural frequency with load stiffening analysis for the second mode are in Table 4.3. Since only one critical buckling load is available through ALGOR program, we used theoretical buckling load here. The linear coefficient, $\alpha = 0.5643$, was obtained for the second mode.

Table 4. 3 Natural frequency with load stiffening for the 2nd mode

Load P (dyn)	ω (rad/s)	Load P (dyn)	ω (rad/s)
0	3176.17	2400000	1597.76
50000	3151.61	2600000	1386.98
100000	3126.84	2800000	1139.68
1000000	2639.18	3000000	825.32
2000000	1953.31	3200000	282.01
2200000	1784.33	3220000	144.02

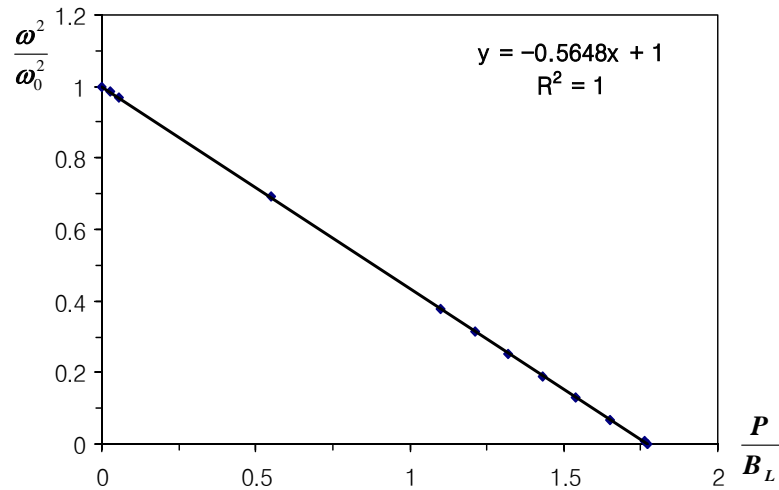


Figure 4. 4 Relationship between natural frequency and axial force for the 2nd mode of the beam with clamped-free boundary condition

4.4 Derivation of the Nonlinear Term

The parameter h in Eq. (4.1.1) represents the nonlinear load-deflection relationship of the beam. Since the material is assumed to be linear elastic, the nonlinearity is a result of the geometric nonlinearity. This can be quantified by using the static nonlinear analysis tool of the finite element packages.

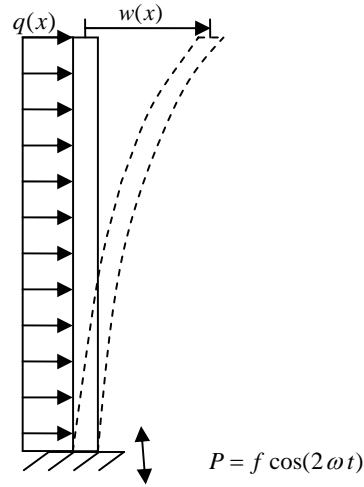


Figure 4. 5 Cantilever beam with parametric excitation

We assumed distributed load $q(x)$ acting on the beam in the horizontal direction such as shown in Fig. 4.5. Let $w(x)$ denote the displacement of the beam at a certain location x .

Table 4. 4 Displacement for several different horizontal forces using FEM

		Total horizontal force (dyn)					
		10000	100000	200000	300000	400000	500000
Nodal displacement (cm)	1	0	0	0	0	0	0
	2	0.0040	0.0396	0.0754	0.1060	0.1321	0.1545
	3	0.0151	0.1475	0.2791	0.3894	0.4806	0.5567
	4	0.0317	0.3090	0.5806	0.8028	0.9813	1.1260
	5	0.0525	0.5111	0.9541	1.3081	1.5849	1.8031
	6	0.0764	0.7427	1.3785	1.8762	2.2560	2.5480
	7	0.1026	0.9948	1.8373	2.4854	2.9698	3.3345
	8	0.1301	1.2599	2.3179	3.1199	3.7093	4.1454
	9	0.1585	1.5326	2.8107	3.7685	4.4629	4.9694
	10	0.1872	1.8086	3.3090	4.4235	5.2228	5.7992
	11	0.2160	2.0857	3.8092	5.0805	5.9847	6.6308

The coefficient, $\frac{h}{m}$, can be obtained by using the relationship between the external force acting on the beam and the displacement of the beam.

$$L = k\delta + h\delta^3 \quad (4.4.1)$$

where L is the generalized force, and δ is the generalized coordinate.

For a discretized beam, the beam displacement can be expressed in terms of its mode shapes.

$$w(x) = \sum_{i=1}^n \delta_i(t) \Phi_i(x) \quad (4.4.2)$$

where, Φ_i denotes the i th mode shape of the beam. We can use δ_i as a generalized coordinate. To obtain the nonlinear relationship between L and δ , we apply a uniform load to the beam in the direction shown in Fig. 4.5. Using the nonlinear static analysis tool in ALGOR, we obtain the nodal displacements corresponding to different total loads. These results are shown in Table 4.4. The boundary conditions at node #1 and #11 are *clamped* and *free* respectively.

From these values, we obtain the displacements of the generalized coordinate

$$\delta_i = \int_0^l w(x) \Phi_i(x) dx \quad (4.4.3)$$

and the corresponding generalized force

$$L_i = \int_0^l q(x) \Phi_i(x) dx . \quad (4.4.4)$$

Table 4. 5 Displacement when lateral uniform load was applied

Total force (dyn)	First mode		Second mode	
	L_1	δ_1	L_2	δ_2
1000	3.92	0.0055	-2.233	-0.0008
10000	39.23	0.0552	-22.330	-0.0082
100000	392.28	0.5336	-223.297	-0.0909
200000	784.57	0.9793	-446.593	-0.2228
300000	1176.85	1.3144	-669.890	-0.3946
400000	1569.13	1.5582	-893.186	-0.5849
500000	1961.41	1.7368	-1116.480	-0.7759

In Figs. 4.6 and 4.7, the red stars represent the displacements when the beam is subjected to the corresponding lateral forces. The relationship between the forces and the displacements was found using SPSS program [49], a commercial program by which one can carry out a regression analysis. Finally, we can get the unknown coefficients in Eq. (4.4.1) as shown in table 4.6.

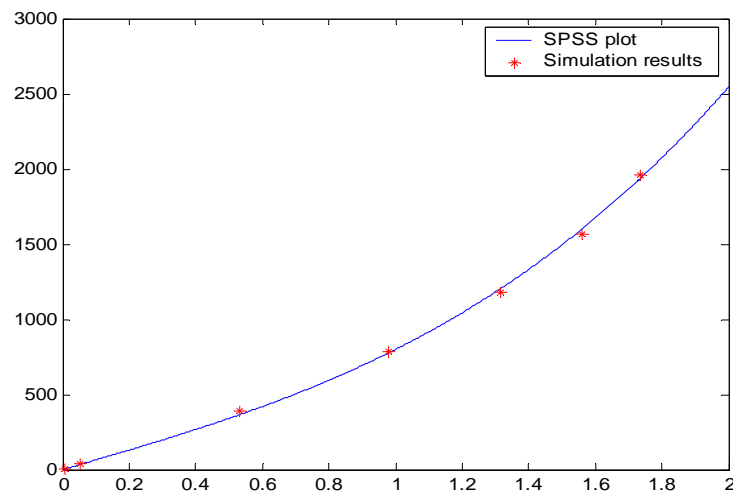


Figure 4. 6 Relationship between external load and displacement for the 1st mode of the cantilever beam

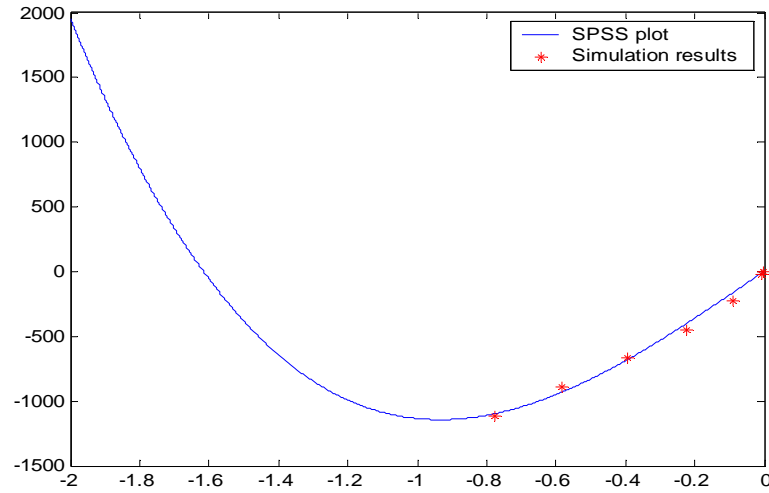


Figure 4. 7 Relationship between external load and displacement for the 2nd mode of the cantilever beam

Since only the term $\frac{h}{m}$ is needed in Eq. (4.1.1), we recall that $\frac{k}{m} = \omega_0^2$. Therefore

$$\frac{h}{m} = \frac{k}{m} \frac{h}{k} = \omega_0^2 \frac{h}{k} \quad (4.4.5)$$

In other words, the ratio of the two regression parameters is the nonlinear parameter we need to predict the beam response to the parametric forcing. The parameters are given in Table 4.6.

Table 4. 6 Two regression parameters and nonlinear term

coefficient	1 st mode	2 nd mode
h	158	-704.48
k	640	1839.38
h/m	64892.69	-3863773.49

4.5 Boundary Condition Effect

In Section 4.3 and 4.4, the boundary condition of the beam was Clamped-Free. That is, at $x = 0$, the beam has the boundary condition [50]

$$\text{Deflection} = w = 0, \text{ Slope} = \frac{\partial w}{\partial x} = 0.$$

Moreover, at $x = l$, the beam has the condition becomes

$$\text{Bending moment} = EI \frac{\partial^2 w}{\partial x^2} = 0, \text{ Shear force} = \frac{\partial}{\partial x} \left[EI \frac{\partial^2 w}{\partial x^2} \right] = 0.$$

Through the numerical simulation we found that the boundary condition is a crucial factor for the coefficient α . Figures 4.8 and 4.9 are the dimensionless frequency responses when the boundary condition of the beam is Clamped-Clamped and the dimensions are the same as those of the case simulated in Section 4.3 through 4.4. In this case, the boundary conditions are

$$\text{Deflection} = w = 0, \text{ Slope} = \frac{\partial w}{\partial x} = 0$$

at $x = 0$ and $x = l$. The ALGOR critical buckling load analysis gives the buckling load to be 392,752,000 dyn when the beam has a distributed axial load.

As shown in the figures, while we have a linear relationship between the square of the natural frequency and the applying axial force with clamped-free boundary condition, the relationship between the two is nonlinear with clamped-clamped boundary condition. It is to say that a clamped-free boundary condition may allow the system to be simpler and more predictable than clamped-clamped one for the parametric excitation.

We didn't introduce the other boundary condition cases such as a clamped-pinned

and a clamped-slide because these boundary conditions are not suitable for the design of micro vibratory gyroscopes.

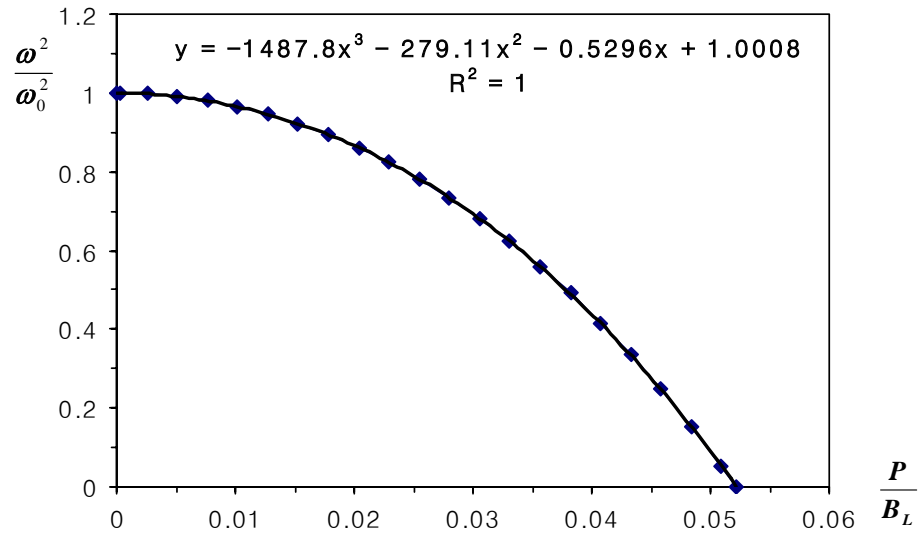


Figure 4. 8 Relationship between natural frequency and axial force for the 1st mode of the beam with clamped-clamped boundary condition

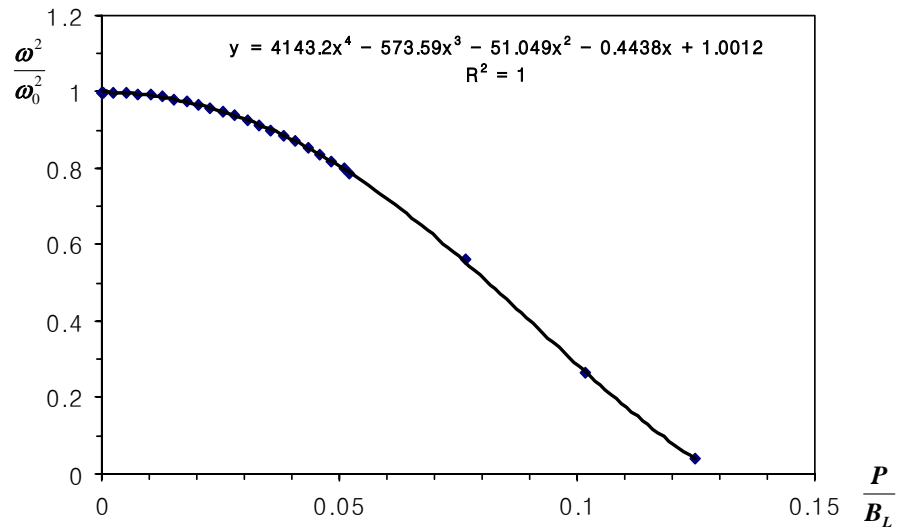


Figure 4. 9 Relationship between natural frequency and axial force for the 2nd mode of the beam with clamped-clamped boundary condition

4.6 Comparison of Averaging Method and Simulation

In the study of dynamical systems, the method of averaging is used to study certain time-varying systems by analyzing easier, time-invariant systems which is obtained by averaging the original system. The idea of averaging as a computational technique has been formulated very clearly by Lagrange in 1788. Ferdinand Verhulst [51] describes the method of averaging effectively in his book. When we have a weakly nonlinear system with small parameter ε

$$\ddot{x} + \omega^2 x + \varepsilon f(x, \dot{x}, t) = 0, \quad (4.6.1)$$

its averaged equations become as follows;

$$\dot{r} = \left\langle \left(\frac{\varepsilon}{\omega} \right) f \sin \Phi \right\rangle \quad r\dot{\Phi} = \left\langle \left(\frac{\varepsilon}{\omega} \right) f \cos \Phi \right\rangle, \quad (4.6.2)$$

where $\Phi = \omega t + \varphi$, and $\langle \rangle$ denotes an average over one cycle of Φ .

From the previous section, the coefficients of the beam equation have been obtained by regression analysis in SPSS program. The equation with a cubic nonlinearity would be

$$\ddot{\delta} + 2\zeta\omega_0\dot{\delta} + \omega_0^2(1 - \alpha \frac{P}{B_L})\delta + \omega_0^2\tilde{h}\delta^3 = 0 \quad (4.6.3)$$

where, $\tilde{h} = \frac{h}{k}$ and $P = 4a\omega^2 \cos 2\omega t$.

For the averaging method, let us assume the following:

$$\zeta = \varepsilon \cdot d, \quad \tilde{h} = \varepsilon \cdot \bar{h}, \quad \alpha \frac{P}{B_L} = \varepsilon \cdot 4\bar{a} \cos 2\omega t, \quad \omega^2 - \omega_0^2 = \varepsilon \cdot \omega_0^2 \sigma, \quad \text{where } \varepsilon \ll 1.$$

Equation (4.6.3) can be written as

$$\ddot{\delta} + \omega^2 \delta + \varepsilon \{-\omega_0^2(\sigma + 4\bar{a} \cos 2\omega t)\delta + 2d\omega_0\dot{\delta} + \omega_0^2\bar{h}\delta^3\} = 0 \quad (4.6.4)$$

From the equations (4.6.1) and (4.6.4), we have

$$f = -\omega_0^2(\sigma + 4\bar{a} \cos 2\omega t)\delta + 2d\omega_0\dot{\delta} + \omega_0^2\bar{h}\delta^3. \quad (4.6.5)$$

Now, let's assume $\delta = r \cos \Phi$ and substitute (4.6.5) into (4.6.2), we get

$$\begin{aligned} \dot{r} &= \left(\frac{\varepsilon}{\omega}\right) \{-\omega_0^2(\sigma + 4\bar{a} \cos 2\omega t)r \cos \Phi + 2d\omega_0(-\omega r \sin \Phi) + \omega_0^2\bar{h}r^3 \cos^3 \Phi\} \sin \Phi > \\ &= \left(\frac{\varepsilon}{\omega}\right) (-4\omega_0^2\bar{a}r \cos 2\omega t \cos \Phi \sin \Phi - d r \omega_0 \omega) > \end{aligned} \quad (4.6.6)$$

Recall that the integration over one period of oscillation becomes:

$$\begin{aligned} \frac{1}{T} \int_0^T \sin \omega t \cos \omega t dt &= 0 \\ \frac{1}{T} \int_0^T \sin^2 \omega t dt &= \frac{1}{T} \int_0^T \cos^2 \omega t dt = \frac{1}{2}. \end{aligned} \quad (4.6.7)$$

Equation (4.6.7) and the trigonometric formula lead to

$$\begin{aligned} \cos \Phi \sin \Phi \cos 2\omega t &= \frac{1}{2} \sin 2\Phi \cos 2\omega t = \frac{1}{4} \{\sin(2\Phi - 2\omega t) + \sin(2\Phi + 2\omega t)\} \\ &= \frac{1}{4} \{\sin 2\varphi + \sin(4\omega t + 2\varphi)\}, \text{ where } \Phi = \omega t + \varphi. \end{aligned}$$

Equation (4.6.6) becomes

$$\dot{r} = \frac{\varepsilon}{\omega} (-\omega_0^2\bar{a}r \sin 2\varphi - d r \omega_0 \omega) \quad (4.6.7)$$

Since $\omega = \sqrt{\omega_0^2 + \varepsilon \omega_0^2 \sigma} = \omega_0 + \frac{\varepsilon \omega_0 \sigma}{2} + O(\varepsilon^2)$ and ε is small, high order terms of ε

may be disregarded. Therefore equation (4.6.7) can be written as

$$\dot{r} = \frac{\varepsilon}{\omega} (-\bar{a} \sin 2\varphi - d) \omega_0^2 r \quad (4.6.8)$$

In the same way, substitute (4.6.5) into (4.6.2) and we get

$$\begin{aligned}
 r\dot{\varphi} &= \left(\frac{\varepsilon}{\omega}\right)\{-\omega_0^2(\sigma + 4\bar{a}\cos 2\omega t)r\cos\Phi + 2d\omega_0(-\omega r\sin\Phi) + \omega_0^2\bar{h}r^3\cos^3\Phi\}\cos\Phi > \\
 &= \frac{\varepsilon}{\omega}\left(-\frac{\omega_0^2}{2}\sigma r - 4\omega_0^2\bar{a}r\cos 2\omega t\cos^2\Phi + \frac{3}{8}\omega_0^2\bar{h}r^3\right) > .
 \end{aligned} \tag{4.6.9}$$

Recall the trigonometric formula again, which says

$$\begin{aligned}
 \cos\Phi\cos\Phi\cos 2\omega t &= \frac{1}{2}\cos 2\Phi\cos 2\omega t = \frac{1}{4}\{\cos(2\Phi - 2\omega t) + \cos(2\Phi + 2\omega t)\} \\
 &= \frac{1}{4}\{\cos 2\varphi + \cos(4\omega t + 2\varphi)\}, \text{ where } \Phi = \omega t + \varphi.
 \end{aligned}$$

Equation (4.6.9) yields

$$r\dot{\varphi} = \frac{\varepsilon}{\omega}\left(-\frac{\sigma}{2} - \bar{a}\cos 2\varphi + \frac{3}{8}\bar{h}r^2\right)\omega_0^2r \tag{4.6.10}$$

For the fixed points, equations (4.6.8) and (4.6.10) should satisfy the condition, $\dot{r} = 0$ and $\dot{\varphi} = 0$. The equations yield

$$-\bar{a}\sin 2\varphi - d = 0 \tag{4.6.11}$$

$$-\frac{\sigma}{2} - \bar{a}\cos 2\varphi + \frac{3}{8}\bar{h}r^2 = 0 \tag{4.6.12}$$

From Eqs. (4.6.11) and (4.6.12), we get

$$\bar{a}^2 = d^2 + \left[\frac{3}{8}\bar{h}r^2 - \frac{\sigma}{2}\right]^2 \tag{4.6.13}$$

The solution of Eq. (4.6.13) yields

$$r^2 = \left[\frac{\sigma}{2} \pm \sqrt{\bar{a}^2 - d^2}\right] / \frac{3}{8}\bar{h} \tag{4.6.14}$$

Note that the nonlinear coefficient \bar{h} is in the denominator. That is, the response amplitude is indeterminate if \bar{h} is not known. This is why it is essential to determine the

nonlinear term in predicting parametric responses of the beam. As shown in Fig. 4.10, the response of the equation has two branches. It is well-known that the top branch is stable and the bottom branch is unstable

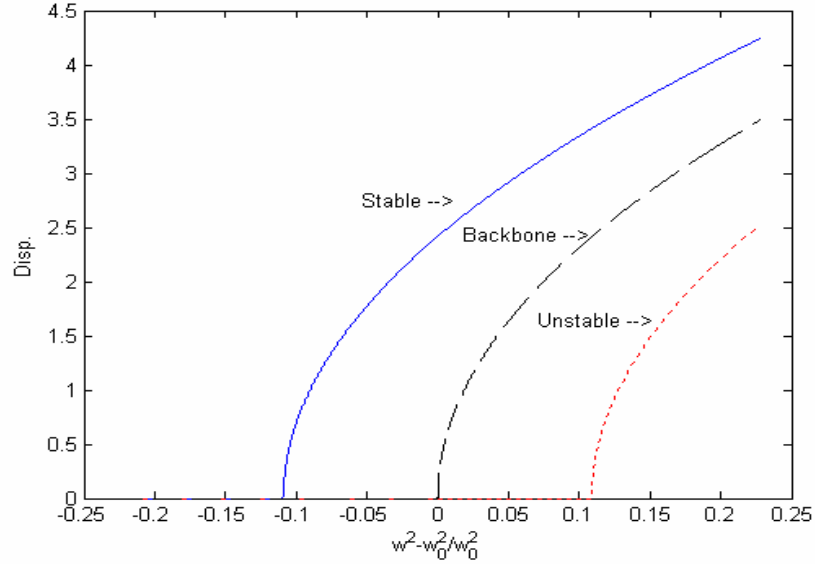


Figure 4. 10 Results of averaging method of the beam

Now let's discuss the critical parametric forcing amplitude \bar{a} for the equation. Setting the part inside the square root to zero, we get

$$\bar{a}^2 - d^2 = 0 ,$$

which gives the critical forcing amplitude $\bar{a} = d$. As shown in Fig. 4.11, when applied force crosses the threshold of the system, the system has nontrivial solutions as well as trivial one. In other words, when $\bar{a} \geq d$, the parametric excitation is possible. In Fig. 4.11, the lower pitch fork, $-r$, represents the response which has the same amplitude as r but the phase angle differs by $\pi \text{ rad}$.

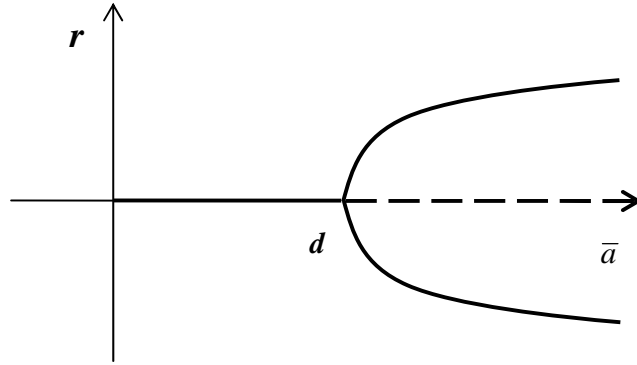


Figure 4. 11 pitchfork bifurcation at $\bar{a} = d$

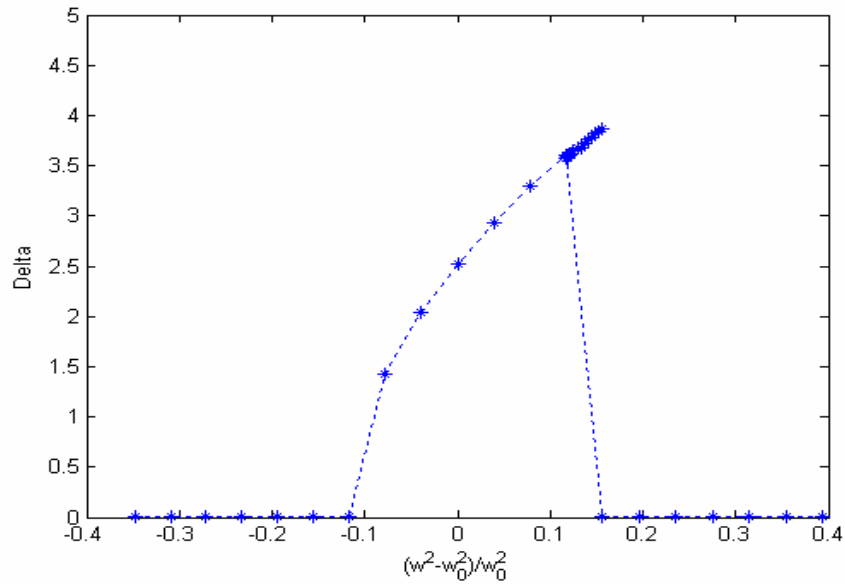


Figure 4. 12 Displacement of the beam : Simulation result using Runge Kutta method

Figure 4.12 is the numerical simulation results of Eq. (4.6.1) obtained by Runge-Kutta method, which is widely used in numerical integration of ordinary differential equations by using a trial step at the midpoint of an interval to cancel out lower order error terms. The second order formula, known as RK2, is

$$k_1 = h f(x_n, y_n)$$

$$k_2 = hf(x_n + \frac{1}{2}h, y_n + \frac{1}{2}k_1)$$

$$y_{n+1} = y_n + k_2 + O(h^3)$$

and the fourth-order formula is

$$k_1 = h f(x_n, y_n)$$

$$k_2 = h f(x_n + \frac{1}{2}h, y_n + \frac{1}{2}k_1)$$

$$k_3 = h f(x_n + \frac{1}{2}h, y_n + \frac{1}{2}k_2)$$

$$k_4 = h f(x_n + h, y_n + k_3)$$

$$y_{n+1} = y_n + \frac{1}{6}k_1 + \frac{1}{3}k_2 + \frac{1}{3}k_3 + \frac{1}{6}k_4 + O(h^5)$$

From Eq. (4.6.1), if we let $x_1 = \delta$, $x_2 = \dot{\delta}$, we get two equations such that

$$\dot{x}_1 = x_2$$

$$\dot{x}_2 = -2\zeta \omega_0 x_2 - \omega_0^2 (1 - \alpha \frac{P}{B_L}) x_1 - \omega_0^2 \tilde{h} x_1^3.$$

As shown in the figure, the response of the beam shows a hardening nonlinearity; the response becomes much bigger when the excitation frequency is greater than twice of the natural frequency of the beam. With the increase of the forcing frequency, the response drops down to zero at certain point. Now the trivial solution is also stable. We can see that parametrically excited solution remains stable by selecting steady-state at a lower frequency as initial condition.

Figures 4.10 and 4.11 show that the results from the analytical method and the numerical simulation are in good agreement. Recall that numerical simulation can only locate stable steady-state.

4.7 Summary

In this chapter, we used the finite element method to obtain parameters which are crucial in designing parametrically excited gyroscopes. Effectiveness of the parametric excitation obtained using the critical buckling load analysis and the natural frequency with load stiffening analysis in commercial ALGOR program. Moreover, the nonlinearity of the system was obtained by using FEM and simple dynamics between applying force and displacement. The equation obtained by this method was simulated analytically and numerically.

We used parametrically excited cantilever beam as an example. However, since the simplified model is based on calculations using finite element methods, our approach can be applied to gyro design with more complex structures.

Chapter 5

Experiments with a Tuning Fork Beam

In this chapter, we investigated the feasibility of the new operational method using a fork type aluminum beam. 3D Motion analysis camera system was employed to capture the motion of the beam in real time. We describe in detail the usage of a 3D motion analysis system to characterize nonlinear dynamics of the beam. We begin with a detailed description of the experimental set-up and the data acquisition devices. Then the experimental procedure is presented and discussed. In the result, frequency response curves are obtained for several different parametric excitation amplitudes.

5.1 Experimental Setup

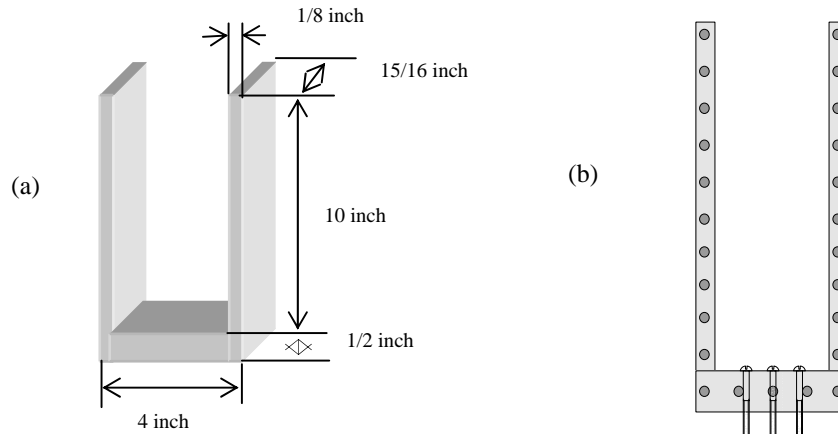


Figure 5. 1 Experimental model: (a) tuning fork type beam (b) reflection marks on the model

As shown in Fig. 5.1, a fork shaped aluminum beam was used to investigate the parametric excitation effect. The dimension of each tine is $10in \times 15/16in \times 1/8in$ and

two tines are connected to the base beam, whose dimension is $4in \times 15/16in \times 1/2in$. The tuning fork beam was built in a whole structure using a general machine tool. The reason we used a relatively large size of beam for the experiment is to magnify the parametric force effect.

Because the 3D motion analysis system uses reflection signal from the retro reflective marker adhered to the model, twenty-five $4mm$ diameter retro-reflective markers were adhered to the beam and were distributed equally through whole beam. As shown in Fig. 5.1, the end markers, #1 and #25, were put close to the tip of the tines of the beam.

5.2 Natural Frequencies and Mode Shapes

The natural frequency of the structure can be calculated by the formula which is derived from the cantilever beam whose boundary condition is clamped-free. The formula is given by;

$$\omega_n = b_n^2 \sqrt{EI / \rho A}$$

Where ω_n denotes the n^{th} natural frequency, b_n is the n^{th} coefficient at the specific boundary conditions, E is Young's modulus, I is the moment of inertia, ρ is the mass density, and A is the area of the beam.

Table 5. 1 Material property of Aluminum 6061-T651 [52]

Mass Density (kg/m^3)	2,700
Modulus of Elasticity (N/m^2)	68,947,000,000
Poisson's Ratio	0.33
Thermal expansion coefficient ($1/^\circ C$)	0.00002358
Shear Modulus (N/m^2)	26,000,000,000

Aluminum 6061-T651 is used for the experiment. The material properties of the tuning fork beam are shown in Table 5.1.

First of all, finite element modeling and analysis of the tuning fork beam was performed to obtain its Natural frequencies. The 3D model was built in line drawing, and the model was then meshed and the boundary conditions specified in ALGOR. Through the finite element analysis in ALGOR, natural frequencies and mode shapes of the tuning fork were obtained as shown in Fig. 5.2.

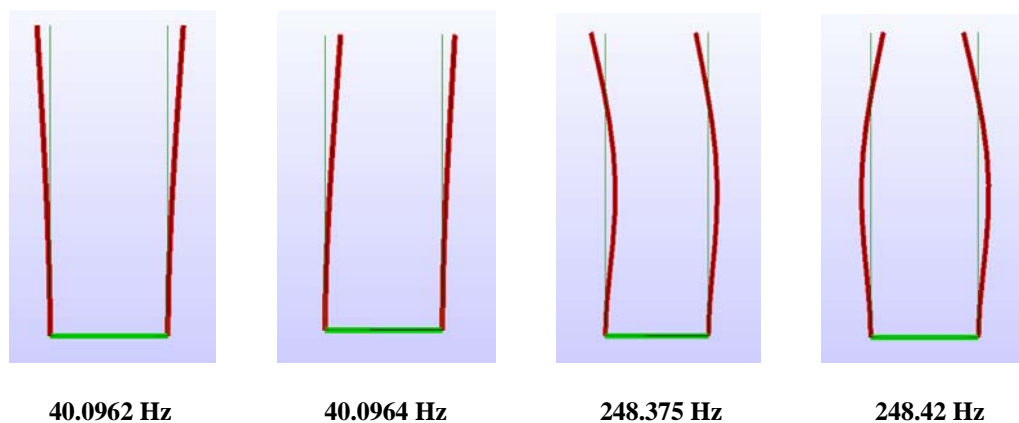


Figure 5. 2 Natural frequencies and mode shapes

The tuning fork beam is clamped on a shaker head with a metal bolt. Furthermore, two metal washers were used between the tuning fork beam and the shaker head to obtain a point fixed boundary condition. The bottom area of the beam applied a fixed boundary condition except vertical movement. Table 5.2 gives a comparison of natural frequencies between the results from finite element analysis and theoretical calculation to predict its parametric resonance. The natural frequency of the beam yields 40.16 Hz by the theory. In other words, if we assume the structure has the same boundary condition as the clamped-free beam, the resonance occurs when the parametric excitation frequency is around 80.32 Hz by the theory.

Table 5. 2 Comparison of natural frequencies

	Theory (Hz)	FEM (Hz)	Difference (%)
1 st mode	40.1591	40.0962	0.156
	-	40.0964	-
2 nd mode	251.6729	248.375	1.31
	-	248.42	-

5.3 Experiment Method

5.3.1 The 3D Motion Analysis System

The 3 D Motion Analysis System is a non contacting vibration measurement device [53]. It consists of several high-resolution CMOS (complementary metal-oxide-semiconductor) digital cameras, the Eagle Hub, and EVaRT software. In our experiment, 3 digital cameras were used. Figure 5.3 shows an experimental set up using Eagle-500 digital real-time motion analysis system.



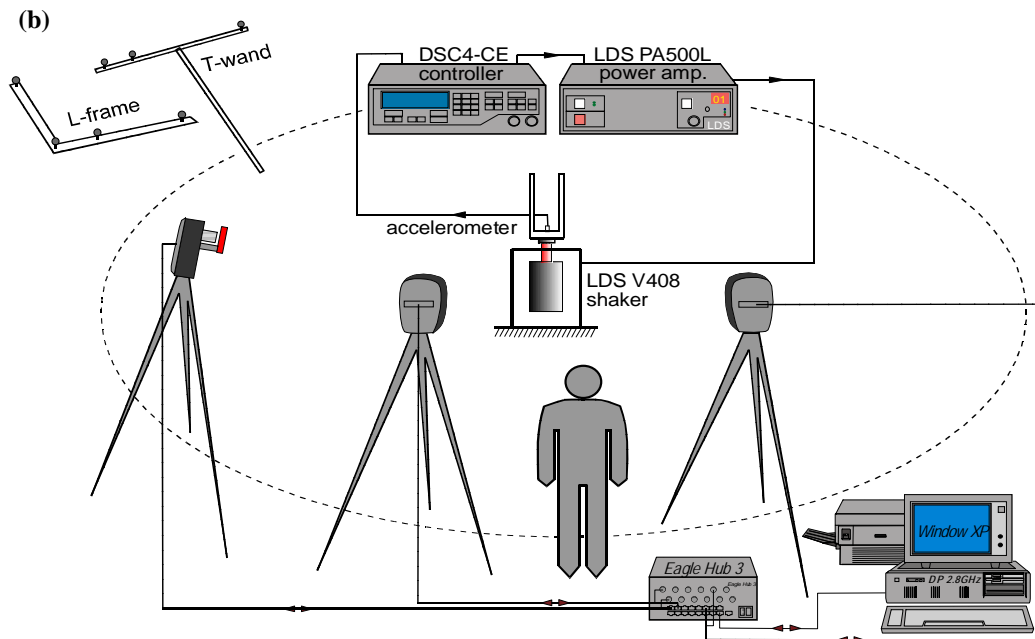


Figure 5. 3 Experimental set up using EAGLE-500 digital real-time motion analysis system:

(a) actual experimental set up (b) schematic set up of experiment

This system uses triangulation techniques. A calibration is performed using an L-frame with four markers and a T-wand with three markers. After the calibration, the camera system automatically computes and records the instant 3D coordinates of the center of each retro-reflective marker that is seen by at least two cameras using the Eagle real-time software EVaRT 4.1. The recording time length is effectively infinite and up to 600 markers can be simultaneously traced. Since the 3D coordinates of each marker are checked and calibrated when more than two cameras see the marker, the measurement accuracy is very high. For instance, when the measurement volume is $2 \times 2 \times 2 \text{ m}^3$, the measurement error is less than 1.0 mm. Because this system has many benefits such as high measurement capability, easy operation, and simple set up, it becomes a new standard for motion capture.

5.3.2 Eagle Digital Camera

The Eagle digital cameras can capture images of a structure when the visible red LED strobes light up the retro-reflective markers which are put on the structure already. Each camera can capture up to 500 frames per second with a 1280×1024 full resolution, 1000 frames per second with a 1280×512 resolution, 2000 frames per second with a 1280×256 resolution. In addition, their processing rate reaches up to 600 million pixels per second. Signals from an Eagle digital camera go directly to the tracking computer via an Ethernet connection. This streamlined system of motion capture from camera to computer allows less hardware and less potential problems. Moreover, the Field Programmable Gate Array (FPGA) built into the Eagle is upgradeable via the Internet. The features of Eagle cameras are listed below [54]:

- The frame rates are selectable from 1 to 2000 Hz.
- Two suitcases allow bringing up to 8 cameras.
- Built-in zoom provides more visual options.
- For low optical distortion, the camera uses a high quality 35mm lens.
- Visible red, near red, or infrared ringlights are available.
- Through the LED display panel on camera, one can notice the status of the cameras.
- The light output and electronic shutter can be controlled by the software.

Camera placement is one of the most important aspects of setting up the motion analysis system. If we place the cameras in good positions, the results will be accurate

and the editing time will be greatly reduced. There are several things to be considered, when deciding the number of cameras to be used.

First, there should be sufficient number of cameras to insure that at least two cameras can capture all markers at all times. Generally, when the motion of the subject becomes less restrained and the capture volume is increased, the number of cameras must be increased.

Second, when more cameras are used, each camera should view only a portion of the capture volume to achieve higher accuracy. One should prevent too many cameras capture the same marker. The only requirement is that all 4 markers on the calibration square should be visible in at least half of the cameras used. If too many cameras see the same marker such as 5 or 6, the accuracy of tracking is not increased and the computation time is increased.

Third, to ensure the highest possible spatial resolution, camera views should not include areas outside the capture volume.

5.3.3 Eagle Hub

The Eagle hub consists of multi-port Ethernet switch (100Mbps) and provides power for the cameras. For all signals and power between the camera and the Eagle hub, a single Ethernet Cat 5 cable is used.

5.3.4 EVaRT

The EVa real-time software (EVaRT) provides the user with a simple and powerful interface. Under a single software environment, the user can set up, calibrate, capture motion in real-time, capture motion for post processing, and edit and save data in a

chosen format.

5.3.5 Ling Dynamics LDS V408 Shaker

The beam is excited using a Ling Dynamics LDS V408 shaker, which has a maximum output force of 196 N and a frequency range of 5 to 9000 Hz, to supply the oscillatory boundary condition at the base of the beam. We assumed the shaker-head motion is same as the base of the beam because the beam is securely attached on the shaker-head. The motion was monitored by means of an accelerometer mounted to the base of the beam.

5.4 Experiment Procedure

Because the nonlinear vibration may depend on the initial conditions, if the tests are carried out by continuously varying parameters, either the excitation frequency or amplitude, we may mistake nonlinear transient vibration as a steady-state response. Therefore, for the steady-state response, we need to change only one parameter value at a time.

In our experiments, we stop each test before changing the parameter (frequency or amplitude) for the next test. Each test starts with zero initial conditions, and hence the tests are direction independent. Once we get the steady state, we disturb the vibration and then check other possible steady state solutions. By this way, we simulate vibrations starting with different initial conditions and hopefully will not miss possible multiple solutions.

At the beginning, we use a sweeping method, which uses the continuously varying frequency, to find out the parametric resonance range. Once we notice a rough range

where parametric resonance occurs, we carry out the experiment with the excitation frequency change while the excitation amplitude is held constant. The procedure is repeated with the different forcing frequencies. For every parameter changing, the transient motion dies out and so the steady state is reached before the response is captured. In general, a steady state will be attained in half to one minute after the excitation reaches the specified amplitude. Normally, it takes longer time for the response to reach a steady state for tests with parameters around where the multiple solutions exist. For example, it takes longer time to reach a steady state at the boundary frequency where the parametric resonance starts.

Theoretically, the step size of increase or decrease of the parameter depends on the closeness of the excitation frequency to the bifurcation frequencies. When it is close to the resonant frequency, the increase step needs to be small because various nonlinear phenomena exist in a small frequency range. In our experiments, we increase the excitation frequency by 0.05Hz when it is close to the resonant frequency in order to observe possible important phenomena. Actually, the appropriate increase or decrease step size practically depends on experience. The total number of excitation frequency increments and the number of excitation amplitude increments depend on the frequency range we want to investigate and also the capacity of our experimental apparatus.

5.5 Excitation Force Amplitude Scale

We used the excitation force in dB unit. Normally, we use dB units to express the ratio of the power between the output and the input. The relationship among dB, power, and voltage is as follows.

$$dB = 10 \log_{10} \frac{P_o}{P_i} = 10 \log_{10} \frac{V_o^2}{V_i^2} = 20 \log_{10} \frac{V_o}{V_i} \quad (5.5.1)$$

Where, P_o and P_i denotes the output and input electric power, respectively, and V_o and V_i are the output and input voltage. For the open loop, the LDS DSC4 controller provides 1.5 V rms at 0 dB compression.

We carried out the experiments for which the amplitudes of excitations are 0 dB , -1.5 dB , -3.0 dB , -4.5 dB , and -6.0 dB . The ratio of the output voltage to the input voltage can be expressed as shown in Table 5.3 by the formula (5.5.1). Note that the output voltage becomes a half the input voltage when we used -6.0 dB level.

Table 5. 3 The ration of the output voltage to the input voltage

dB	Ratio(out/in)	dB	Ratio(out/in)
0	1	-4.5	0.5957
-1.5	0.8414	-6	0.5012
-3	0.7079	-9	0.3548

5.6 Experimental Results

5.6.1 Parametric Resonance Phenomenon

Using a frequency sweeping method, we could find the region where the resonance phenomenon occurs. We took several frequencies with step 0.05 Hz from the region, and the steady state response was obtained for each case. Figure 5.5 shows the vertical displacements from node #13 (where the beam is connected to the shaker) and its FFT(Fast Fourier Transformation). Furthermore, the time trace of the lateral displacements from node #1 (the tip of the tine) and its FFT are illustrated in Fig. 5.6. For

both cases, 400 reflective data within 1 second were collected and recorded using 3D motion analysis system. For the experiment, -3.0 dB excitation force amplitude and 80.40 Hz frequency were used.

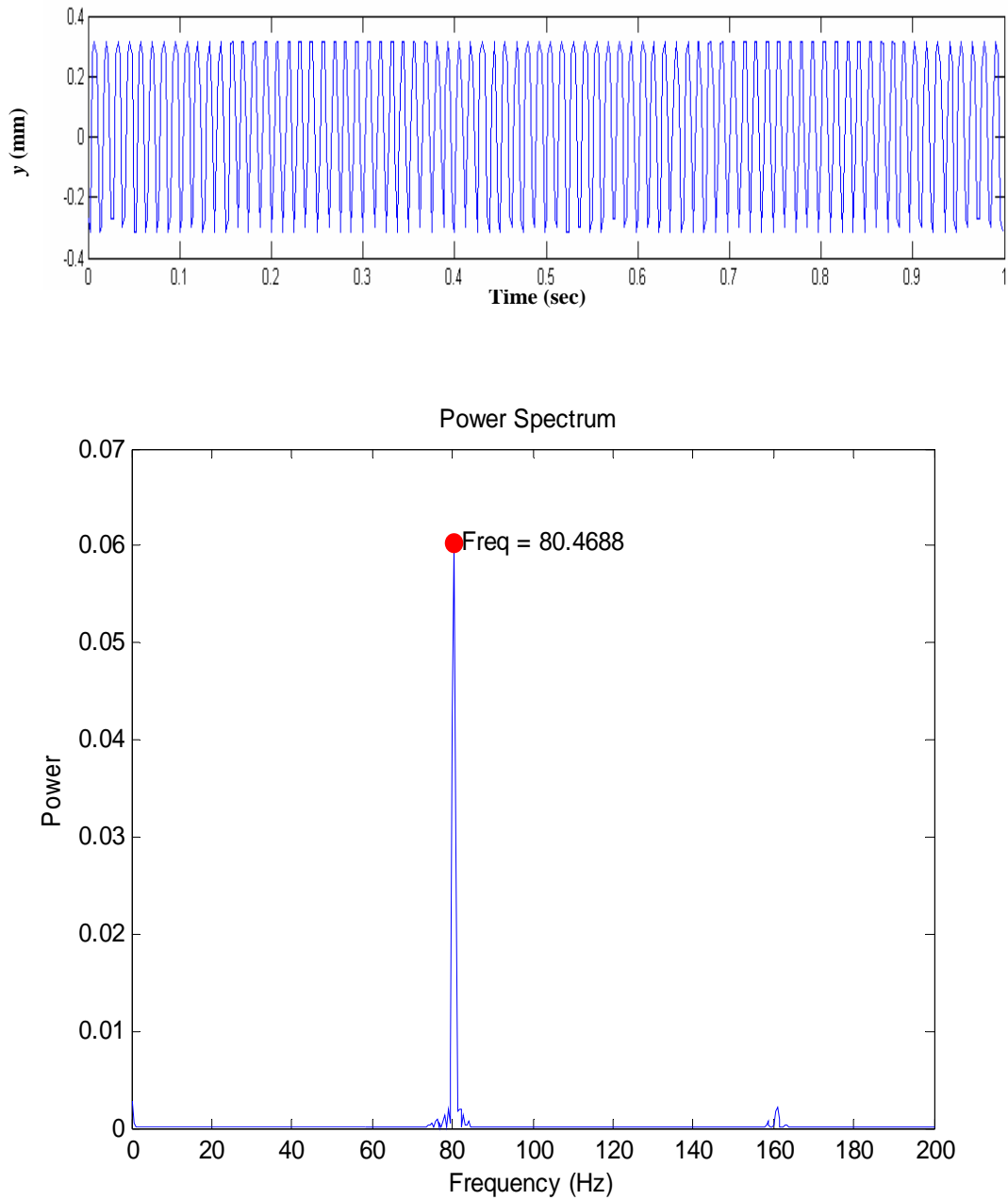


Figure 5. 4 Response at node #13 in vertical direction when $\Omega = 80.40$ Hz and $a = -3$ dB
(a) time trace (b) FFT

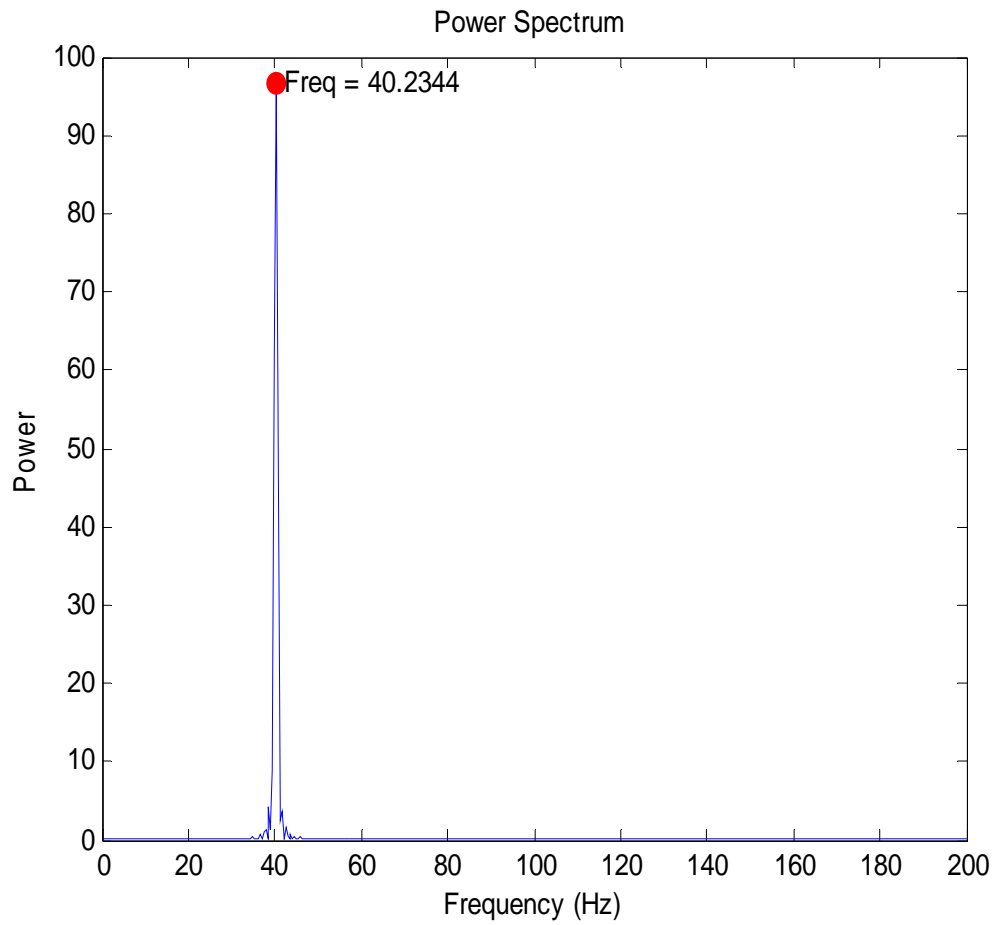
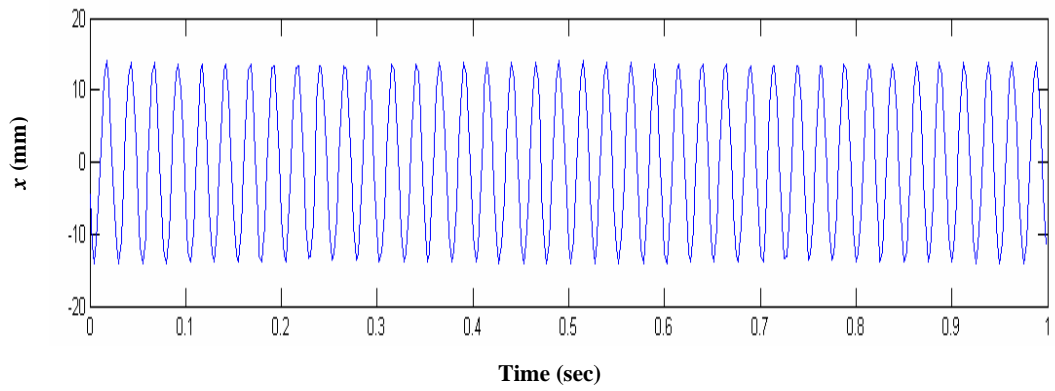


Figure 5. 5 Response at node #13 in horizontal direction when $\Omega = 80.40$ Hz and $a = -3$ dB
 (a) time trace (b) FFT

As shown in Figs. 5.4 and 5.5, the frequency of the lateral movement at the tines of the tuning fork beam is about half that of the longitudinal parametric force. The frequency of the vertical direction excitation at node #13 was 80.47 Hz , while the frequency of the lateral movement at node #1 was 40.23 Hz .

5.6.2 Swing in Symmetric Motion

Figure 5.6 shows the vibration pattern of two tines of the beam. The response time traces at two nodes, #1 which is the tip of the left tine and #25 which is the tip of the right tine, are presented in one figure to compare the vibrating direction of two tines. The solid line is the time trace at node #1 and dotted line is the time trace at node #25.

As shown in the figure, the two tines vibrate in opposite direction. The response is very stable with the same displacements. This result has a good agreement with our previous simulation with two pendulums in which two pendulums swing in opposite horizontal direction when the pendulums are excited in vertical direction [55].

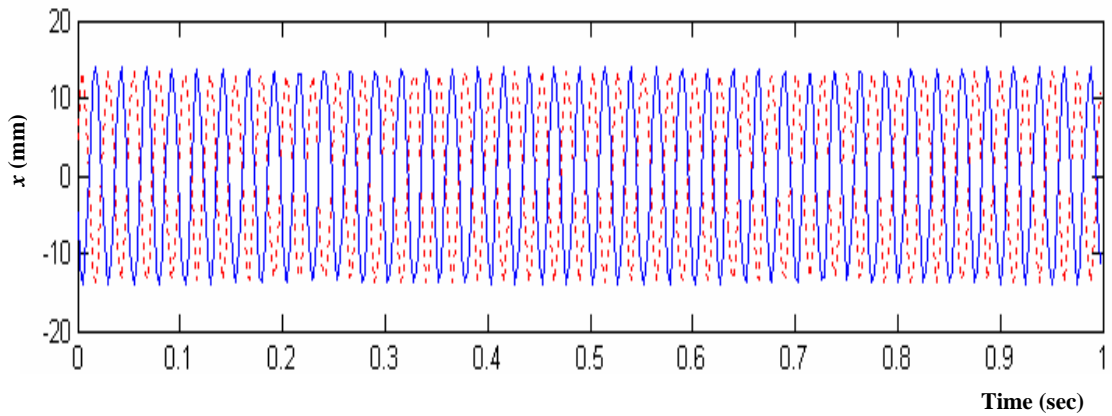


Figure 5. 6 Time trace of the response at node #1 and # 25 when $\Omega = 80.40 \text{ Hz}$ and $a = -3 \text{ dB}$

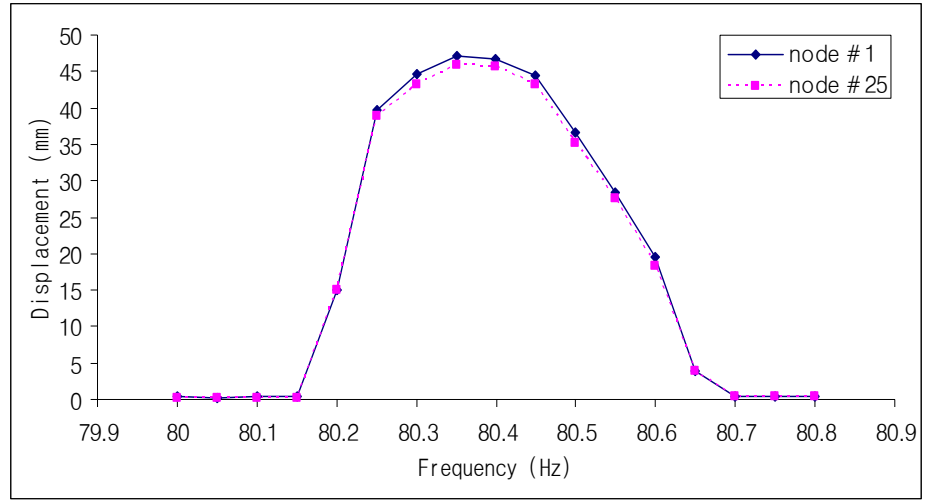


Figure 5. 7 Response curves at node #1 and # 25 when $a = 0$ dB

On the other hand, the steady state response of the beam with excitation force -0.0 dB is shown in Fig. 5.7. As mentioned earlier, node #1 and #25 are in the different tines but with the same level. They have the same amplitude with a few *mm* range difference. It seems to have some errors due to the marker's level or the camera system resolution.

In Fig. 5.8, the pictures captured by digital camera show the swing patterns of the tuning fork beam with parametric excitation more clearly.

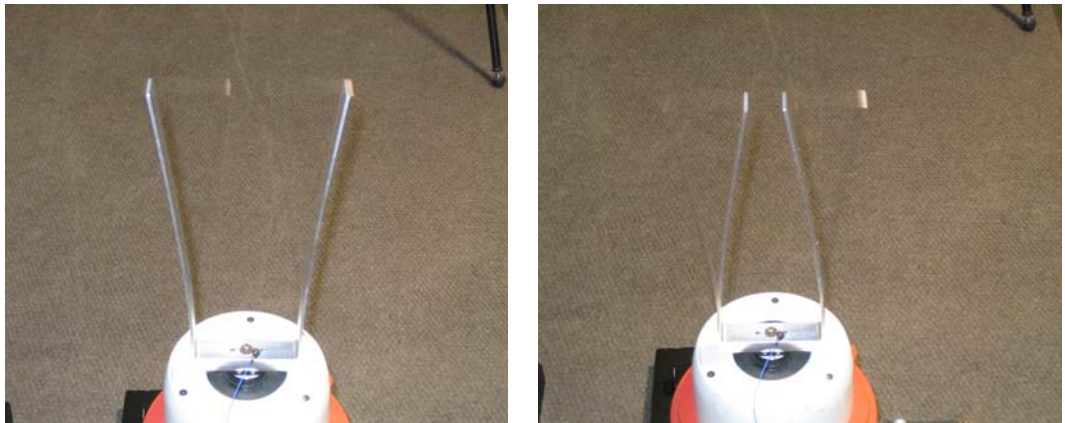


Figure 5. 8 The swing patterns captured by a digital camera when the parametric force $a = 0$ dB

5.6.3 Softening Nonlinearity

An interesting phenomenon with the response curve shown in the figure is that the left side of the curve is steeper than the other side. When the frequency is increased from 80 Hz , the displacement of the beam remains zero until the frequency reaches 80.20 Hz . Once the frequency becomes $80.20 - 80.25\text{ Hz}$, there is a big jump to the big displacement. The response then gradually increase up to the frequency of 80.35 Hz , and decreases slowly all the way to 80.70 Hz . The whole resonance region is so narrow that it is less than 0.5 Hz width. In other words, it is very sensitive to the frequency change of the parametric excitation. We also experienced a long transient phenomenon at the boundary frequency, 80.20 Hz , of the parametric resonance. It seems to have two different steady state solutions, trivial and non-trivial.

In this experiment, we could get high amplitude of displacement of the beam with parametric excitation. As shown in Fig. 5.9, when the shaker displacement is 1 mm , the amplitude of the beam reaches up to 48 mm at the resonance. If we recall that the main focus on this experiment is to check the feasibility of parametric excitation for the tuning fork micro gyroscope as an operating method, the parametric response may be a good method for the tuning fork micro gyroscope.

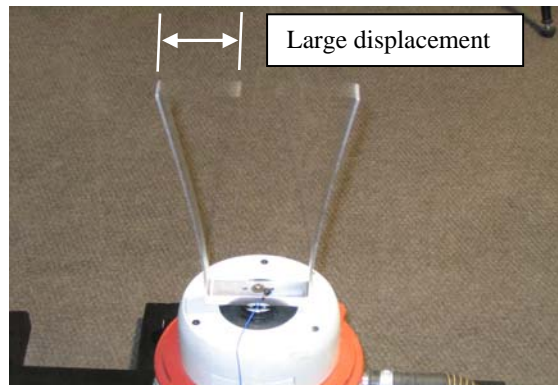


Figure 5. 9 Experimental capture showing large displacement when 1 mm excitation is applied

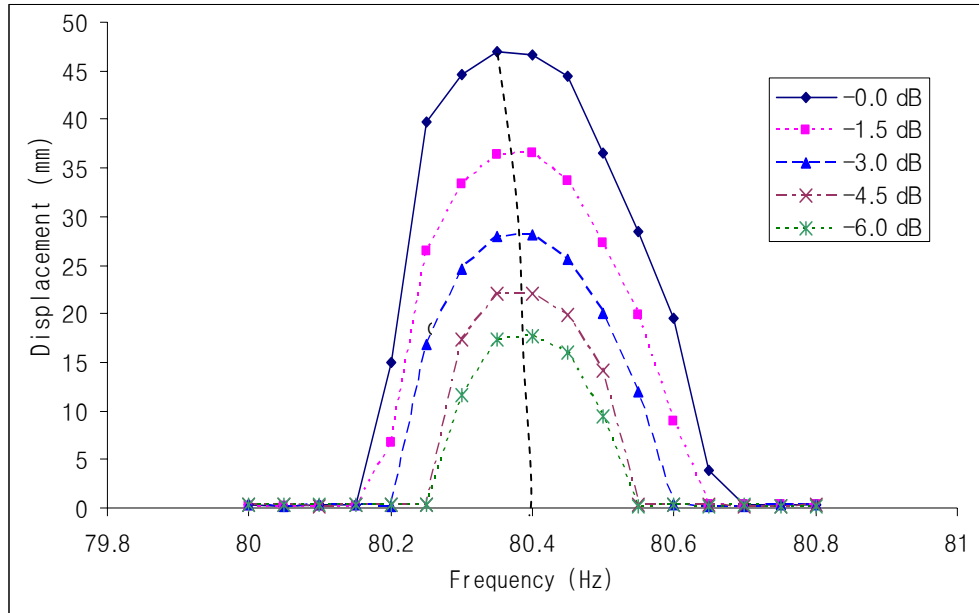


Figure 5. 10 Response of the beam with different excitation amplitude at node #1

Figure 5.10 shows the lateral displacement at the tip of the tines with different parametric forces: -0 dB, -1.5 dB, -3.0 dB, -4.5 dB, and -6.0 dB. As shown in the figure, the response curves are tilting to the left side more clearly when the forcing amplitude increases. In other words, when the forcing amplitude is -6.0 dB, the response curve is near symmetric; however, when the forcing amplitude is 0 dB, it is clearly asymmetric with bending to the left side.

This phenomenon is pretty interesting. Nayfeh and Pai showed the response curve of a clamped-free single cantilever beam is bent to the right for the first mode since the non-linear geometric terms dominate the response [56]. In this experiment we used a tuning fork type beam which has two tines and a connecting rectangular beam. The experimental results show that the response curve is bent to the left and it seems to be softening effect. We will discuss this phenomenon in the next chapter.

5.6.4 Damping Effect to the Base Beam

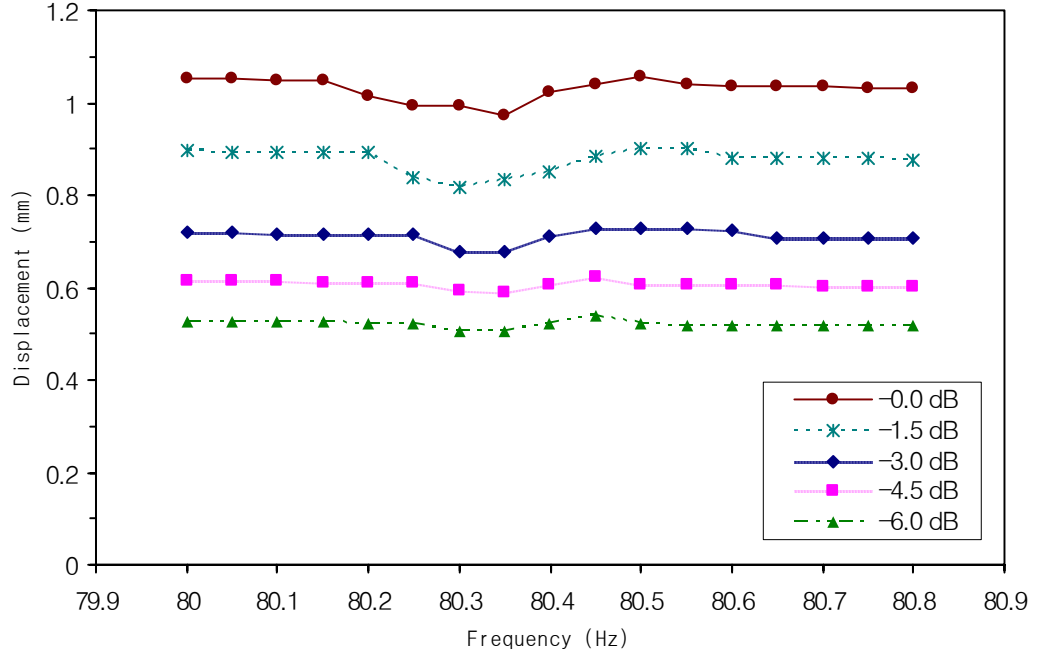


Figure 5. 11 Displacement of the base of the beam with different force amplitudes

Figure 5.11 shows the vertical displacements at node #13, where the beam is connected to the shaker. For the measurement, an accelerometer was attached to the base of the beam. Its sensitivity was 8.85 mV/g or 0.902 mV/m/s².

Recall that the fundamental kinematic properties of a particle moving in one dimension are displacement, velocity, and acceleration. For the harmonic motion, these are given by

$$\begin{aligned}
 \text{Displacement} & : x(t) = A \sin(\omega t + \phi) \\
 \text{Velocity} & : \dot{x}(t) = \omega A \cos(\omega t + \phi) \\
 \text{Acceleration} & : \ddot{x}(t) = -\omega^2 A \sin(\omega t + \phi)
 \end{aligned} \tag{5.6.1}$$

As shown in equation (5.6.1), displacement, velocity, and acceleration have close relationship by a factor of ω and ω^2 respectively. Therefore, using these relationships, we

can easily calculate the displacement from the corresponding acceleration.

In Fig. 5.11, we see the excitation of the base beam is not perfectly consistent. As shown in the figure, the amplitude of the base beam decreased while the tines vibrate laterally. Furthermore, the change of the amplitude of the base beam becomes big when relatively large force amplitude is applied. For this reason, we would say that the lateral vibration of the beam induces the shaker head to decrease the amplitude. In other words, it acts like a simple absorber so that the shaker head amplitude decreases. We will discuss this phenomenon in more details in Chapter 6.

Chapter 6

Practical Problems

In Chapter 5, we implemented the experiment for the tuning fork beam with parametric excitation. The result showed that the parametric force may be a very effective way when we apply it to a tuning fork gyroscope because it can induce larger response than electro static force or direct excitation. To apply to a real gyroscope, however, more detailed study is necessary.

In this chapter, limited shaker power and the effect of gravity will be studied. We solve the governing equation in an analytical way and compare the solution with the experimental results as well. Moreover, we discuss the effect of gravity to explain the softening nonlinear phenomenon shown in the experiment. Since the research for the cantilever beam including previous work done by other researchers and our own work has some discrepancies in the nonlinear tendency, more detailed explanation is necessary.

6.1 Limited Shaker Power

Non-ideal energy source is well known problem in mechanical systems. Evan-Iwanowski [30] gave a good explanation for the problem. A normal assumption used in analysis of many mechanical systems is that the energy source is unlimited. It allows the analysis to be greatly simplified since the coupling effect of system and energy source are ignored. In this section, we discuss the relationship between the lateral response of the

beam and the amplitude of excitation. We will study the beam equation, which was obtained in Chapter 4, with variable amplitude of excitation to see the effect. Recall Eq. (4.6.1), which generally describes beam vibrations.

$$\ddot{\delta} + 2\zeta \omega_0 \dot{\delta} + \omega_0^2 \left(1 - \alpha \frac{P}{B_L}\right) \delta + \omega_0^2 \tilde{h} \delta^3 = 0 \quad (6.1.1)$$

where α represents the efficiency of parametric excitation, \tilde{h} denotes nonlinearity of the system, P is the parametric force applied to the system, and B_L is the critical buckling load. As shown in chapter 4, the averaged equations for Eq. (6.1.1) are as follows.

$$\dot{r} = \frac{\varepsilon}{\omega} (-\bar{a} \sin 2\varphi - d) \omega_0^2 r \quad (6.1.2)$$

$$r\dot{\varphi} = \frac{\varepsilon}{\omega} \left(-\frac{\sigma}{2} - \bar{a} \cos 2\varphi + \frac{3}{8} \bar{h} r^2\right) \omega_0^2 r \quad (6.1.3)$$

It is worthy to recall the parameters which have been used for the calculation;

$$\tilde{h} = \frac{h}{k} = \varepsilon \cdot \bar{h}, \quad \zeta = \varepsilon \cdot d, \quad \alpha \frac{P}{B_L} = \varepsilon \cdot 4\bar{a} \cos 2\omega t, \quad \omega^2 - \omega_0^2 = \varepsilon \cdot \omega_0^2 \sigma, \text{ where } \varepsilon \ll 1,$$

also, h and k are the coefficients obtained in Chapter 4, representing nonlinearity of the system. We obtained the steady state solution for Eqs. (6.1.2) and (6.1.3) given by

$$r^2 = \left[\frac{\sigma}{2} \pm \sqrt{\bar{a}^2 - d^2} \right] / \frac{3}{8} \bar{h} \quad (6.1.4)$$

Solution of Eq. (6.1.4) totally depends on parameter \bar{h} , that is, it is hardening when $\bar{h} > 0$ and is softening when $\bar{h} < 0$ since \bar{h} is closely related to cubic nonlinearity of the system. They show different nonlinearity, however, the common factor of both cases is that the steady state response is a monotonic function of the frequency detuning parameter σ . Figure 6.1 shows the response curve obtained by averaging method when

$\bar{h} = -0.25$. It is gradually increasing without dropping when the excitation frequency is decreased. It is obvious the damping term d does not limit the amplitude of response in parametric system as long as the applied parametric force overcomes the threshold.

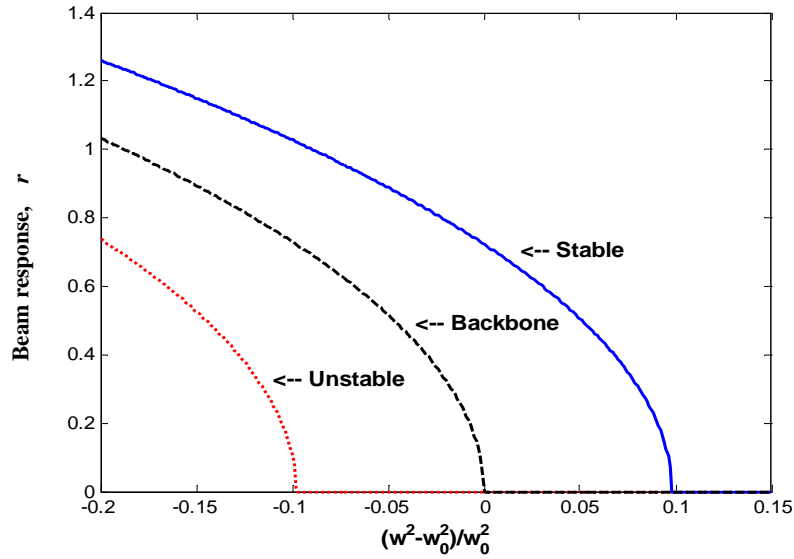


Figure 6. 1 Results of averaging method of the beam : $\bar{a} = 0.05$, $d = 0.01$, $\bar{h} = -0.25$

However, in the practical system, our experimental result shows the steady state response has finite amplitude as shown in Fig. 5.11. Furthermore, in the figure, we notice that the response curves show more nonlinearity, showing asymmetric response curve, when the bigger amplitude of excitation is applied. In other words, the response curve seems to be a symmetric semicircle when -6.0 dB amplitude of excitation is applied, while the response curve bends to the left with 0 dB amplitude of excitation.

This might be caused by the uneven excitation force amplitude. When a shaker is operated without closed-loop control, the shaker head displacement amplitude cannot be maintained at a constant. When the power to the shaker is held fixed, the forcing amplitude on the shaker head can be approximated as constant. Since the lateral vibration

of the beam has damping effect on the shaker head, the shaker head displacement amplitude is affected by the beam vibration. Similar phenomenon was reported by Anderson and Nayfeh in 1996 [57]. They obtained asymmetric curves experimentally and attributed the phenomenon to arbitrary quadratic damping. The results showed good agreement.

Recall the equations again from Chapter 4.

$$-\bar{a} \sin 2\varphi - d = 0 \quad (6.1.5)$$

$$-\frac{\sigma}{2} - \bar{a} \cos 2\varphi + \frac{3}{8} \bar{h} r^2 = 0 \quad (6.1.6)$$

As shown in Chapter 4, the above two equations can be solved for the beam response r and the phase φ . In particular, the amplitude is determined by the following equation:

$$\bar{a}^2 = d^2 + \left[\frac{3}{8} \bar{h} r^2 - \frac{\sigma}{2} \right]^2 \quad (6.1.7)$$

If we assume that the lateral vibration at the parametric resonance reduces the base beam excitation, the force input into the beam is also reduced at certain amount. We let c be the coefficient which determines the base movement.

$$\bar{a}^2 = \bar{f}^2 - cr^2 \quad (6.1.8)$$

Substituting (6.1.8) into (6.1.7) leads to

$$\begin{aligned} \frac{9}{64} \bar{h}^2 r^4 - \left(\frac{3}{8} \bar{h} \sigma - c \right) r^2 + \frac{\sigma^2}{4} + d^2 - \bar{f}^2 &= 0 \\ r^2 &= \frac{\frac{3}{8} \bar{h} \sigma - c \pm \sqrt{\left(\frac{3}{8} \bar{h} \sigma - c \right)^2 - \frac{9}{16} \bar{h}^2 \left(\frac{\sigma^2}{4} + d^2 - \bar{f}^2 \right)}}{\frac{9}{32} \bar{h}^2} \end{aligned}$$

$$= \frac{\frac{\bar{h}\sigma}{2} - \frac{4c}{3} \pm \sqrt{-\frac{4}{3}\bar{h}\sigma + \frac{16}{9}c^2 - \bar{h}^2d^2 + \bar{h}^2\bar{f}^2}}{\frac{3}{8}\bar{h}^2} \quad (6.1.9)$$

6.1.1 Dependence on parameter c

Now let us explore the effects of the parameters included in the equation. Figure 6.2 shows that the response of the beam depends on parameter c . In this case, we used arbitrary parameters, $\bar{f} = 0.02$, $d = 0.01$, and $\bar{h} = -0.35$. When $c = 0.001$, the response curve shows the unstable branch, which is illustrated in red dotted line, as well as the stable one. When parameter c is increased, the response curve is getting close to the symmetric semicircle. Moreover, the parameter c is much more sensitive to the change when it has a small value. In other words, the change of the response curve is much bigger when it is increased from 0.001 to 0.005 than when it is increased from 0.01 to 0.02 as shown in Fig. 6.2.

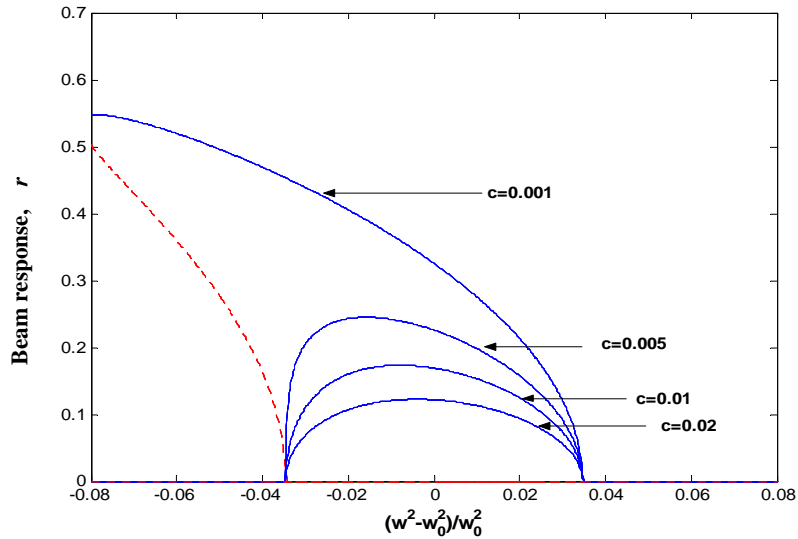


Figure 6. 2 Dependence of the beam response on parameter c : $\bar{f}=0.02$ $d=0.01$ $\bar{h}=-0.35$

6.1.2 Dependence on parameter \bar{h}

Parameter \bar{h} is a nonlinear term as mentioned earlier. Therefore, parameter \bar{h} has also close relationship with the system as shown in Fig.6.3 and Fig.6.4. If $\bar{h} > 0$, as shown in Fig.6.3, the response curve bends more to the right side showing more hardening nonlinearity as \bar{h} is increased. On the other hand, when $\bar{h} < 0$, the response curve bends to the left side, which means the system shows more softening nonlinearity, as \bar{h} is decreased as illustrated in Fig. 6.4. However, both cases show that the amplitude of the response keeps the same regardless of the change of \bar{h} .

We notice that the tendency of the response is more sensitive with a small c . As shown in Fig. 6.3, the change of the response is not too big when \bar{h} increased by 1.6 with $c = 0.02$; however, it is considerably big when \bar{h} changed by 1 with $c = 0.005$ in Fig. 6.4.

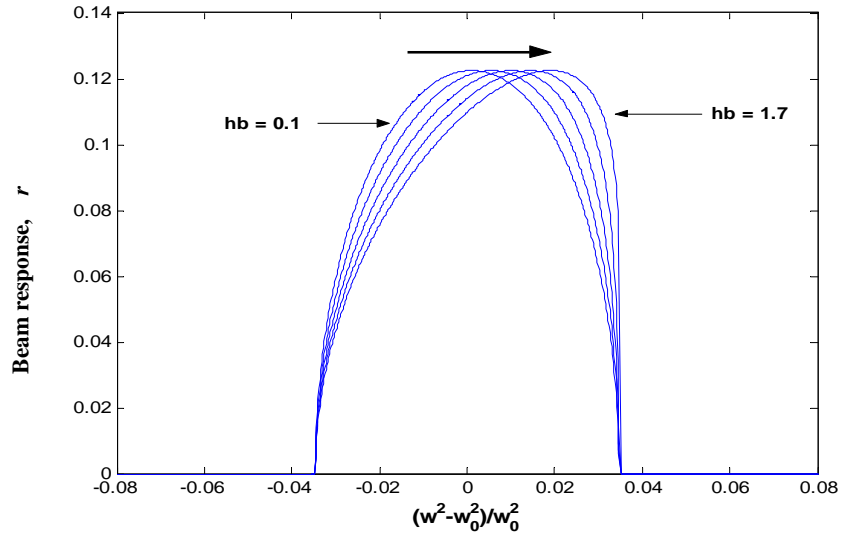


Figure 6.3 Dependence of the beam response on parameter \bar{h} (when $\bar{h} > 0$):
 $\bar{f} = 0.02, d = 0.01, c = 0.02$

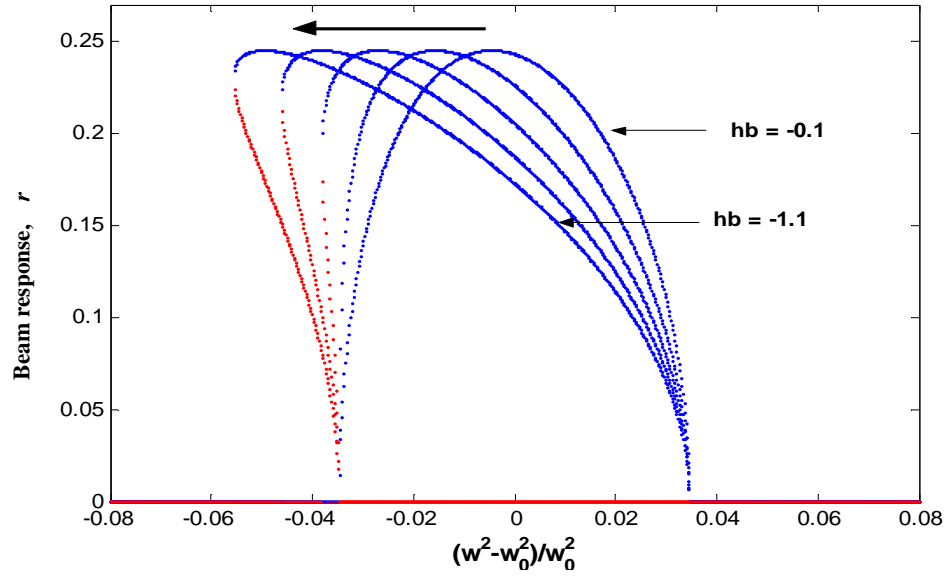


Figure 6. 4 Dependence of the beam response on parameter \bar{h} (when $\bar{h} < 0$) :
 $\bar{f} = 0.02, d = 0.01, c = 0.005$

6.1.3 Dependence on parameter d

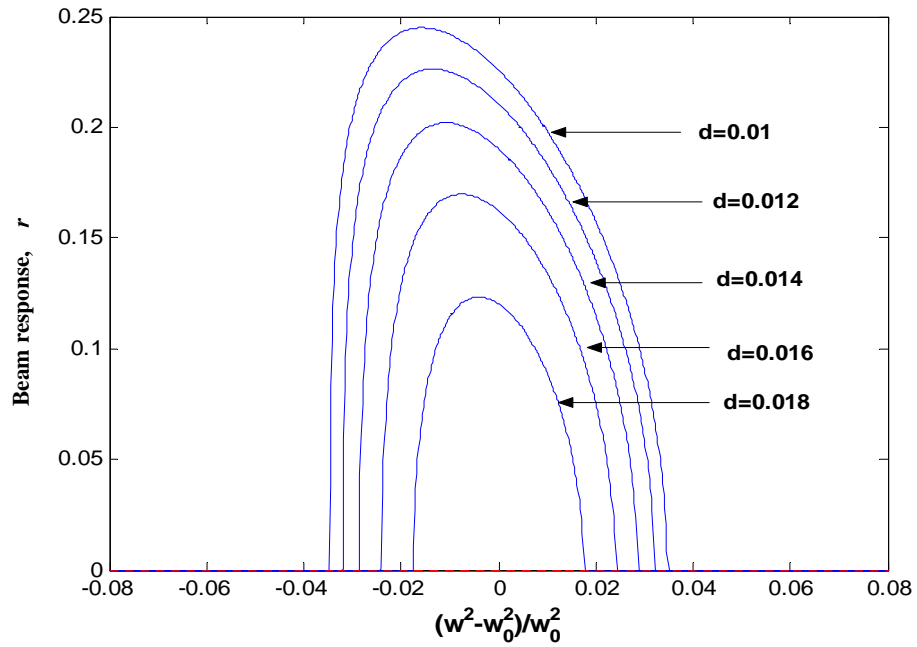


Figure 6. 5 Dependence of the beam response on parameter d : $\bar{f} = 0.02, c = 0.005, \bar{h} = -0.35$

Parameter d plays an important role in the system. As we know, the parametric excitation must exceed the threshold of the system. In other words, the parametric resonance occurs when the following condition is met:

$$(\frac{3}{8}\bar{h}\sigma - c)^2 - \frac{9}{16}\bar{h}^2(\frac{\sigma^2}{4} + d^2 - \bar{f}^2) > 0. \quad (6.1.3)$$

As shown in Fig. 6.5, parameter d is one of the main factors to affect the amplitude of the response. Unlike other parameters, parameter d affects not only the amplitude response but also the bandwidth of the resonance. Even though the fixed force amplitude is applied as shown in Fig. 6.5, the width of the frequency range where the beam response is not zero changes by parameter d . However, it does not affect the tendency of the response curve, hardening or softening. We assumed only linear damping in this simulation.

6.1.4 Comparison between experiment and theory

By now, we explored the parameter dependence of the system and noticed that there are many parameters to affect the system directly or indirectly. We discussed the dependence of the system on the parameters in qualitative aspect; however, still remaining challenge is how we can quantify the parameters to apply to real systems. Figures 6.6 through 6.10 show the comparison between our experimental results and the theory. For the analytical result, we used arbitrary parameters which can fit the response the best to the experiment. The symbols (*) used in the figures represent the results from the experiments, while the curves in solid line show the results from our theory.

We found that the results are in good agreement qualitatively. In Table 6.1, the ratio

of \bar{a} to \bar{h} means the ratio of the actual force amplitude to the applied force before being reduced by parameter c . Furthermore, the ratio of the force amplitudes used in simulations is kept the same as in the experiment. In other words, the force amplitude for the simulation in Fig. 6.6 is half the force amplitude used in Fig. 6.10. Also, the force amplitude applied for the experiment in Fig. 6.6 is half the force amplitude used in Fig. 6.10.

Table 6.1 parameters used in experiment and the analytical result

Experiment	Theory					
Force amplitude	\bar{f}	c	d	\bar{h}	\bar{a}/\bar{h}	
-6.0 dB	0.0040	0.0012	0.0038	-0.1500	0.9500	Fig. 6.6
-4.5 dB	0.0048	0.0015	0.0045	-0.1500	0.9375	Fig. 6.7
-3.0 dB	0.0056	0.0014	0.0052	-0.1500	0.9286	Fig. 6.8
-1.5 dB	0.0068	0.0013	0.0063	-0.1500	0.9265	Fig. 6.9
0.0 dB	0.0080	0.0011	0.0074	-0.1500	0.9250	Fig. 6.10

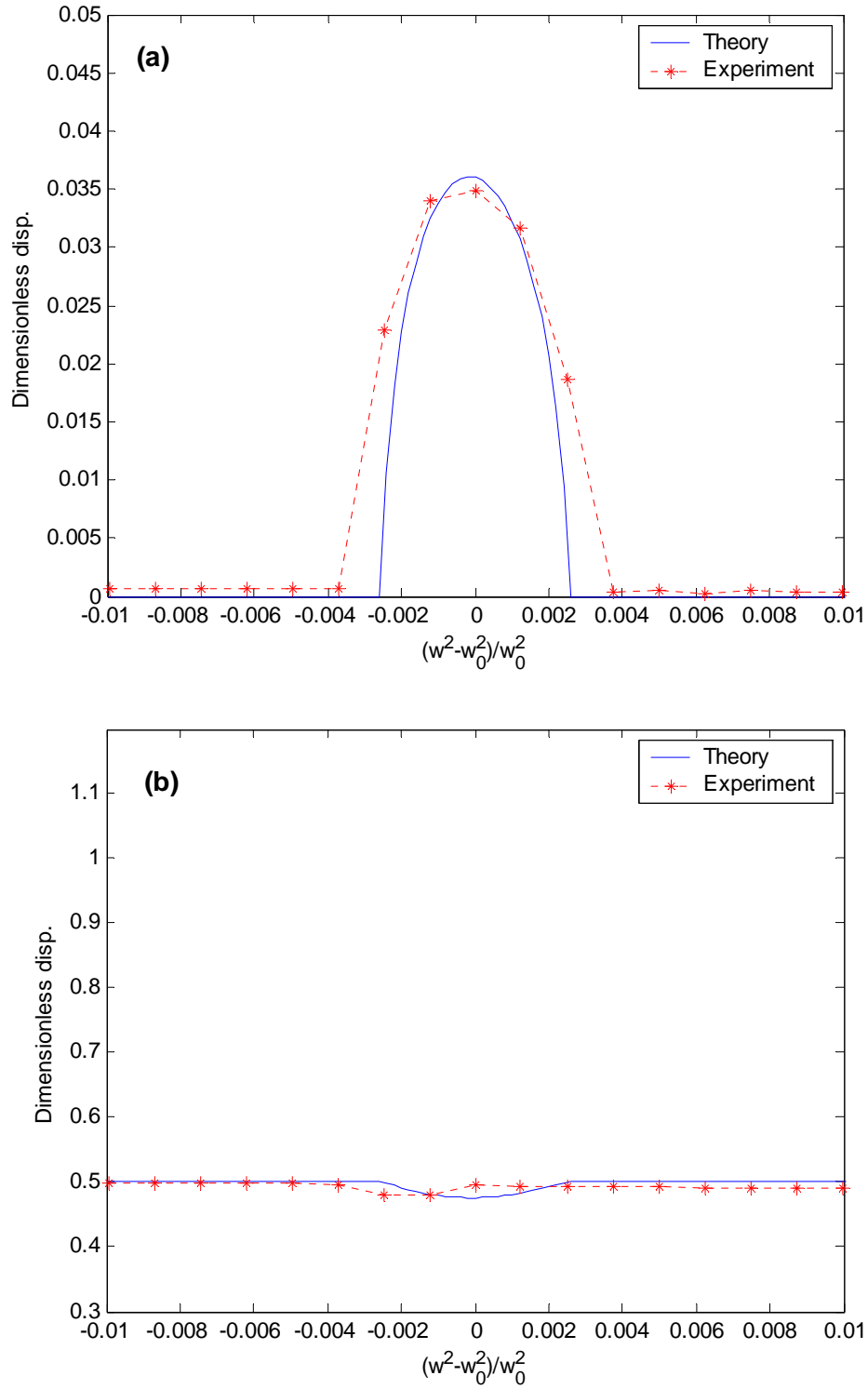


Figure 6. 6 Lateral vibration at the tip of the tine (a) and corresponding base excitation (b)
when experimental force -6.0 dB and $\bar{f}=0.0040$

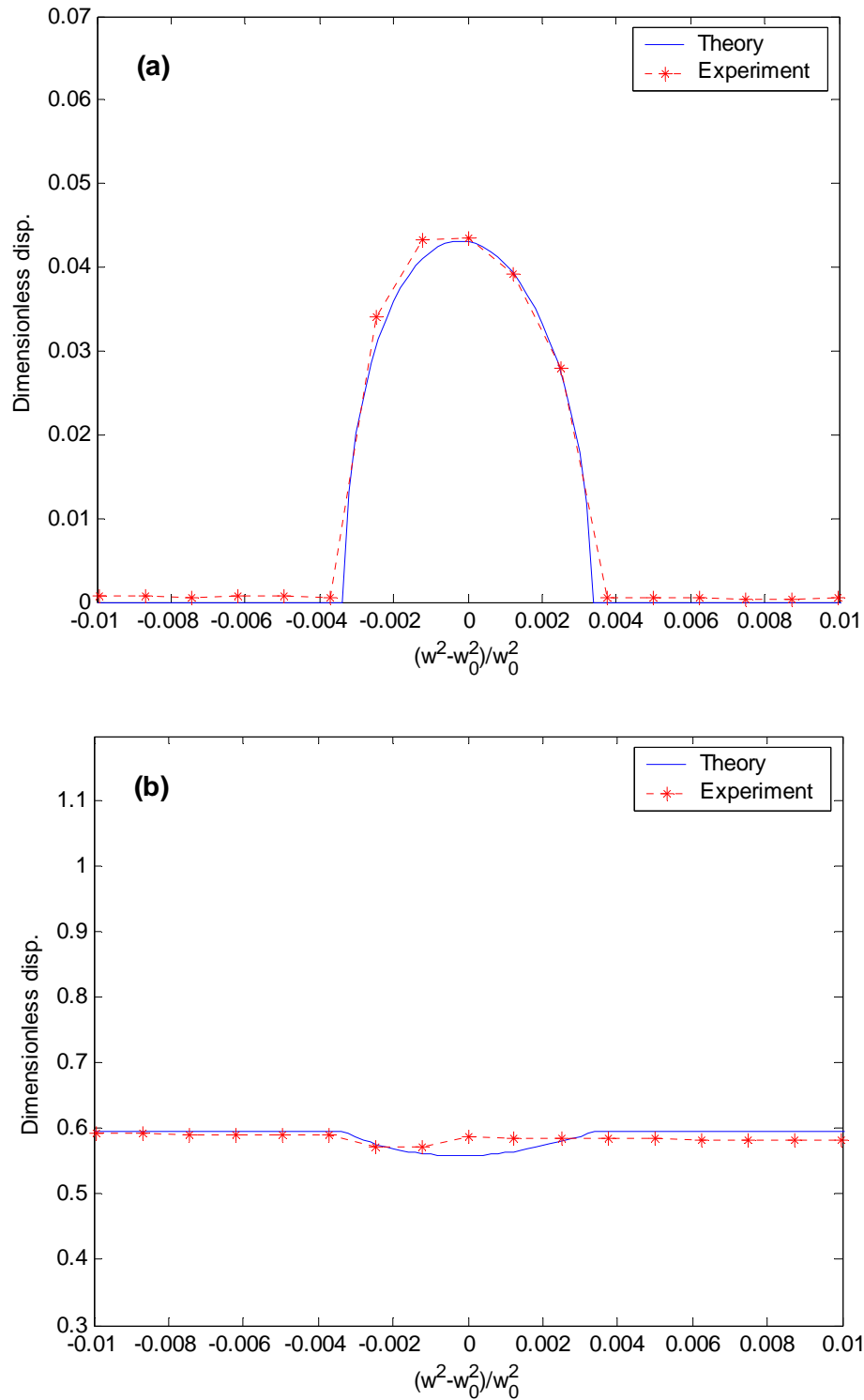


Figure 6.7 Lateral vibration at the tip of the tine (a) and corresponding base excitation (b) when experimental force -4.5 dB and $\bar{f} = 0.0048$

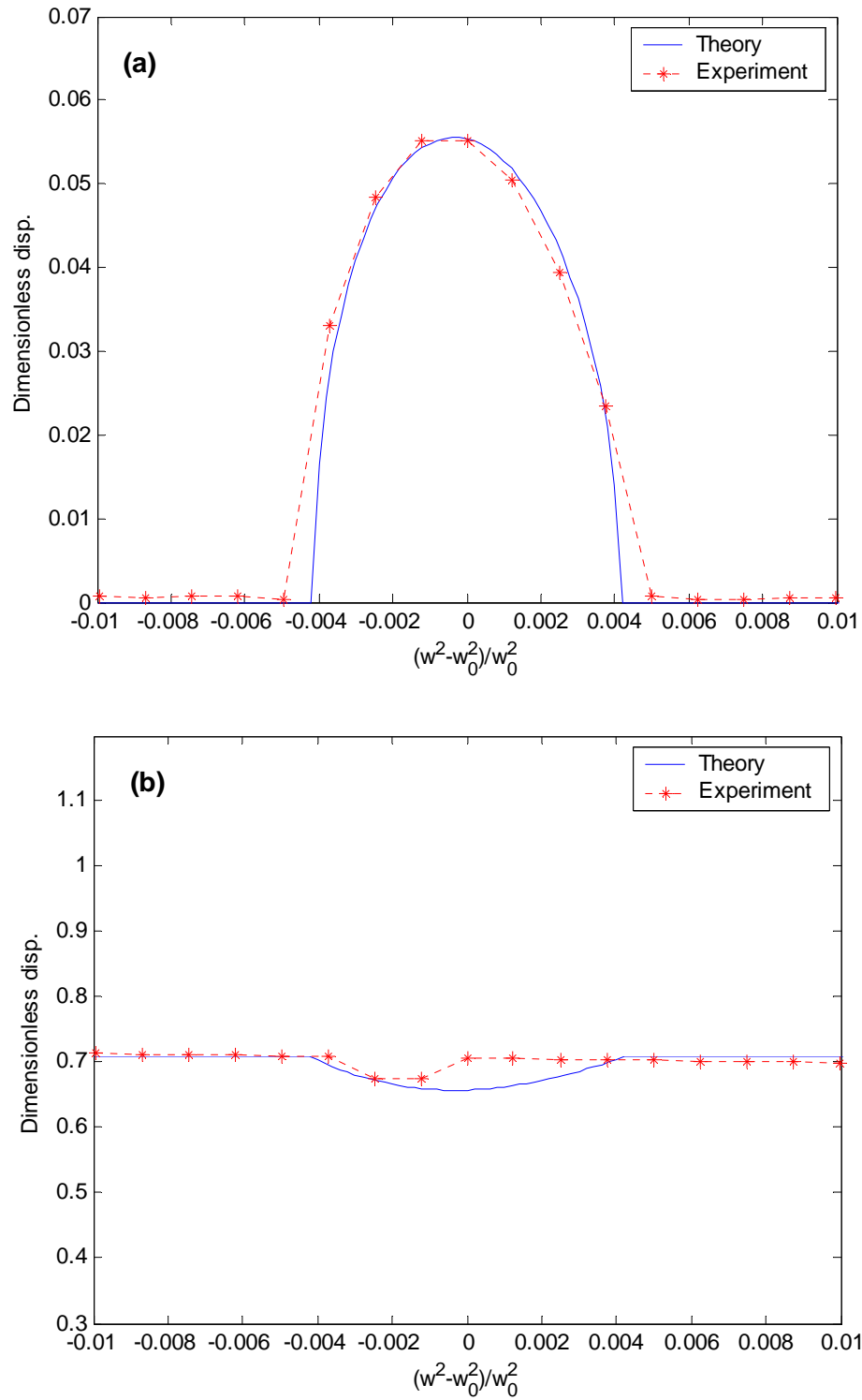


Figure 6. 8 Lateral vibration at the tip of the tine (a) and corresponding base excitation (b) when experimental force -3.0 dB and $\bar{f} = 0.0056$

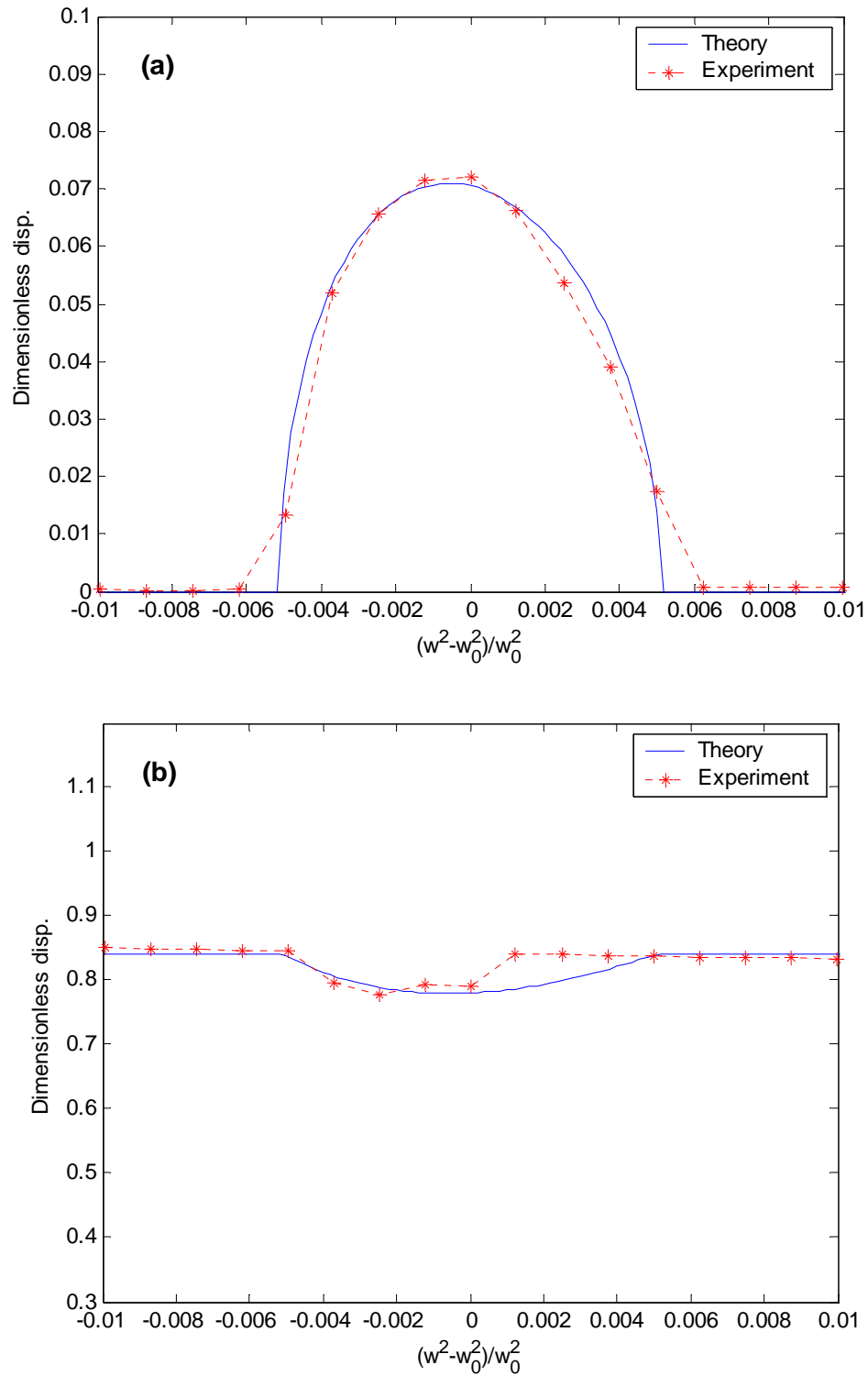


Figure 6. 9 Lateral vibration at the tip of the tine (a) and corresponding base excitation (b) when experimental force -1.5 dB and $\bar{f} = 0.0068$

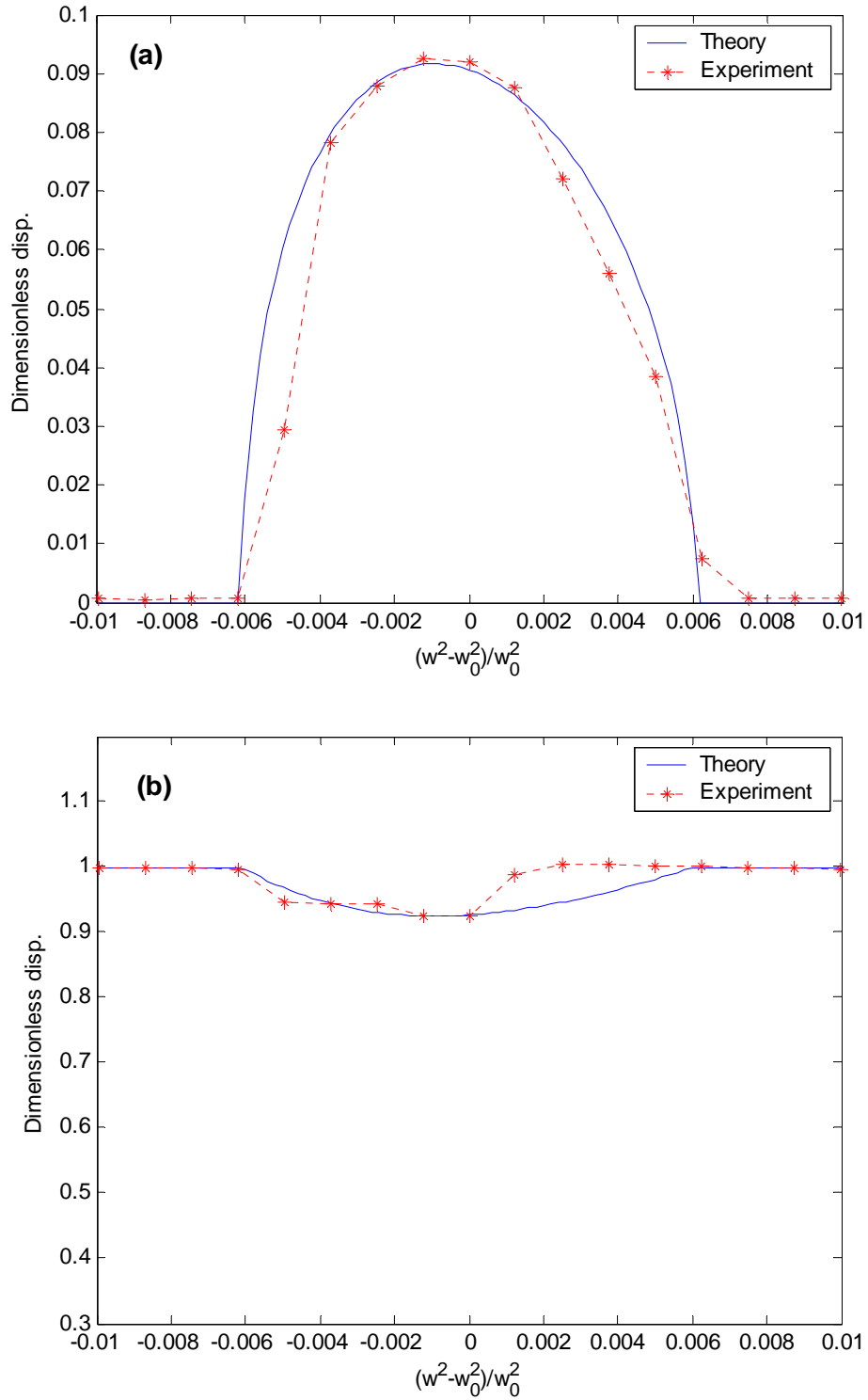


Figure 6. 10 Lateral vibration at the tip of the tine (a) and corresponding base excitation (b)
when experimental force 0 dB and $\bar{f} = 0.0080$

6.2 Gravity Effect

In this section, we discuss nonlinear phenomenon of the first mode response of the cantilever beam, which has boundary condition clamped and free. Many researchers already explored this field and they have made a great progress to reveal the nonlinearities of the cantilever beam.

J. Dugundji and V. Mukhopadhyay [58] carried out an experiment under parametric excitation using a $24\text{ in} \times 3\text{ in} \times 0.02\text{ in}$ Aluminum 6061-T6 and got slightly hardening nonlinear effect in 1973.

Furthermore, A. H. Nayfeh and P. F. Pai [55] studied an inextensional beam with parametric excitation in 1989. They explored using the perturbation method and numerical simulations and noticed that the effective nonlinearity of the first mode is of the hardening type because of the geometric nonlinearity, so one should have to include the geometric nonlinearity for the right result.

Recently, P. F. Pai et al. [59] carried out an experiment using $496.8\text{ mm} \times 52.07\text{ mm} \times 0.4699\text{ mm}$ vertically cantilevered titanium alloy beam. They noticed that the first mode response of the beam showed a softening effect, which means the response is dominated by cubic nonlinearity. They concluded this phenomenon was caused by the initial condition in which the beam was slightly tilted to the left in 2007.

On the other hand, in our research, the first mode response in the experiment showed a softening nonlinearity. According to prior research and our experiment, the nonlinear effect for the first mode of the beam was not consistent. For that reason, we devote this section to explore this phenomenon in more detail.

6.2.1 Downward Pendulum

We assume that there is a pendulum with a spring hanging downward as shown in Fig. 6.11. The particle of mass m is connected to a massless rod of length l and suspended from a platform. The torsional spring has nonlinear characteristics, $k_t = k_0 + h\theta^2$.

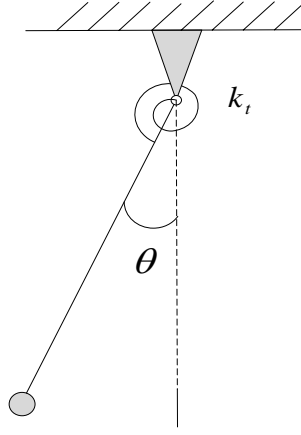


Figure 6. 11 Pendulum with spring

The kinetic energy T and the potential energy V of the pendulum become

$$T = \frac{1}{2} m (l \dot{\theta})^2, \quad V = \frac{1}{2} (k_0 + h\theta^2) \theta^2 - m g l \cos \theta. \quad (6.2.1)$$

where g denotes the gravity.

Recall the Lagrange Equation

$$\frac{d}{dt} \left(\frac{\partial L}{\partial \dot{q}_i} \right) - \frac{\partial L}{\partial q_i} = Q_i \quad i = 1, 2, 3, \dots, n. \quad (6.2.2)$$

where $\dot{q}_i = \partial q_i / \partial t$ is the generalized velocity, L is the difference between the kinetic and potential energies, to be $L = (T - V)$, and Q_i represents all the non-conservative forces corresponding to q_i . In Eq. (6.2.2), the equation with different number of i represents one equation for each generalized coordinate. Lagrangian L becomes

$$L = T - V = \frac{1}{2}m(l\dot{\theta})^2 - \frac{1}{2}(k_0 + h\theta^2)\theta^2 + mgl \cos \theta \quad (6.2.3)$$

Substituting equation (6.2.3) into (6.2.2) leads to

$$ml^2 \ddot{\theta} + k_0 \theta + 2h\theta^3 + mgl \sin \theta = Q \quad (6.2.4)$$

Assuming free oscillation and using Taylor series for the sine function,

$$\sin \theta = \theta - \frac{\theta^3}{3!} + \frac{\theta^5}{5!} - \frac{\theta^7}{7!} + \dots, \quad (6.2.5)$$

equation (6.2.4) can be rewritten by

$$\ddot{\theta} + \left(\frac{k_0}{ml^2} + \frac{g}{l}\right)\theta + \left(\frac{2h}{ml^2} - \frac{g}{6l}\right)\theta^3 = Q. \quad (6.2.6)$$

In Eq. (6.2.4), the linear natural frequency of the pendulum will be $\omega = \sqrt{\frac{k_0}{ml^2} + \frac{g}{l}}$.

Moreover, there is cubic nonlinearity, $\left(\frac{2h}{ml^2} - \frac{g}{6l}\right)\theta^3$, which determines the bending direction of the response curve whether softening or hardening. If we consider damping term, and equation (6.2.6) can be rewritten as

$$\ddot{\theta} + \omega_0^2 \theta + 2\zeta\omega_0 \dot{\theta} + \bar{h} \theta^3 = 4a\omega^2 \cos 2\omega t \theta \quad (6.2.7)$$

where $\omega_0^2 = \frac{k_0}{ml^2} + \frac{g}{l}$, $\bar{h} = \frac{2h}{ml^2} - \frac{g}{6l}$, and $Q = 4a\omega^2 \cos 2\omega t \theta$. (6.2.8)

For the method of averaging, we let the parameters as follows;

$$\zeta = \varepsilon \cdot d, \quad \tilde{h} = \frac{\varepsilon \cdot \bar{h}}{\omega_0^2}, \quad a = \varepsilon \cdot \bar{a}, \quad \omega^2 - \omega_0^2 = \varepsilon \cdot \omega_0^2 \sigma, \quad \text{where } \varepsilon \ll 1.$$

After several steps of algebraic calculation, we have the averaged equations such as

$$\dot{r} = \frac{\varepsilon}{\omega} (-\bar{a} \sin 2\varphi - d) \omega_0^2 r \quad (6.2.9)$$

$$r\dot{\varphi} = \frac{\varepsilon}{\omega} \left(-\frac{\sigma}{2} - \bar{a} \cos 2\varphi + \frac{3}{8} \tilde{h} r^2 \right) \omega_0^2 r \quad (6.2.10)$$

And the steady state response at the fixed point becomes

$$r^2 = \left[\frac{\sigma}{2} \pm \sqrt{\bar{a}^2 - d^2} \right] / \frac{3}{8} \bar{h} \quad (6.2.11)$$

This solution has the same format as solution (4.6.14). As shown in (6.2.8), gravity increases the linearized natural frequency but has a softening effect. The nonlinear phenomenon is decided by the sign of cubic nonlinearity in the cantilever beam; that is

$$\begin{aligned} \bar{h} = \frac{2h}{ml^2} - \frac{g}{6l} > 0 : \text{Hardening} \\ \bar{h} = \frac{2h}{ml^2} - \frac{g}{6l} < 0 : \text{Softening} \end{aligned} \quad (6.2.12)$$

6.2.2 Inverted Pendulum

On the other hand, let us consider the pendulum standing on the ground in upward as shown in Fig. 6.12. We assume that the particle of mass m is connected to a massless rod of length l and standing on the ground. The rod is stabilized by a torsional spring, which has nonlinear characteristics, $k_t = k_0 + h\theta^2$. In the same manner, we can derive the governing equation for the inverted pendulum. The equation is similar to Eq. (6.2.4) except the sign of $\sin \theta$. We have

$$\ddot{\theta} + \left(\frac{k_0}{ml^2} - \frac{g}{l} \right) \theta + \left(\frac{2h}{ml^2} + \frac{g}{6l} \right) \theta^3 = 0. \quad (6.2.13)$$

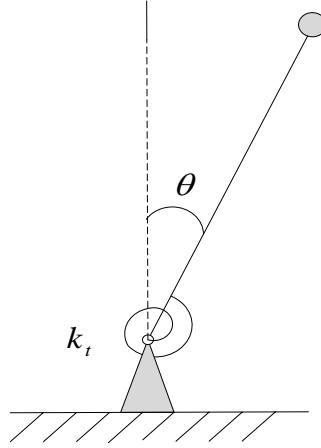


Figure 6. 12 Inverted pendulum with spring

As shown in Eqs. (6.2.6) and (6.2.13), the differences between two cases are the signs in the linear natural frequency and nonlinearity. The linear natural frequency of the

inverted pendulum will be $\omega = \sqrt{\frac{k_0}{ml^2} - \frac{g}{l}}$, while that of the downward pendulum is

$\omega = \sqrt{\frac{k_0}{ml^2} + \frac{g}{l}}$. Furthermore, the nonlinearity of the inverted pendulum is $(\frac{2h}{ml^2} + \frac{g}{6l})\theta^3$,

while that of the downward pendulum is $(\frac{2h}{ml^2} - \frac{g}{6l})\theta^3$.

In the same way as the downward pendulum case, we can derive averaged equation and the final form is exactly the same as that of the inverted pendulum case except the parameter denomination:

$$\omega_0^2 = \frac{k_0}{ml^2} - \frac{g}{l} \quad \text{and} \quad \bar{h} = \frac{2h}{ml^2} + \frac{g}{6l}. \quad (6.2.14)$$

On the contrary, for the inverted pendulum case, gravity reduces the linearized natural frequency but has a hardening nonlinear effect. The effects are opposite for a downward pendulum case.

6.3 Summary

In this chapter, we explored more practical issues related to parametric excitations. Non-ideal energy source due to the limited shaker power was studied. We found that the lateral vibration of the tines affects the base beam and reduces its amplitude by certain amount. We assumed the relationship between the forces, original and reduced, to be $\bar{a}^2 = \bar{f}^2 - cr^2$ and got a good qualitative agreement between the theory and the experiment except for some discrepancies in the frequency range which is larger than the parametric resonance frequency.

For the nonlinear phenomenon, we compared the previous work done by other researchers with our own work and noticed that there still exist some discrepancies too. The gravity effect using pendulum was given, and the relationship between the gravity and the other parameters was described to explain the nonlinear phenomenon. We noticed that, normally, a downward pendulum shows softening nonlinearity, and an inverted pendulum does hardening nonlinearity. However, by the dominating factor in the governing equations, the opposite phenomenon is also possible.

Chapter 7

Conclusions and Recommendation for Future Work

In this dissertation, we studied the characteristics of a parametric excitation and the feasibility of applying it to the MEMS gyroscope through experiments as well as the analytical calculation. We found that the parametric excitation has several advantages when it is applied to the MEMS gyroscope.

First of all, it can generate larger responses compared to electro static force or a direct excitation. It may be a valuable work for the MEMS gyroscope industry because it is experiencing the limitation of the accuracy due to small vibrating amplitude in drive mode.

Secondary, it may be feasible to apply to the MEMS gyroscopes because two tines of the tuning fork beam vibrate in opposite direction. It may have two different vibration patterns, in phase and out of phase. According to the experiment, the opposite direction vibration, we call it *out of phase* or *symmetric motion*, is dominating the vibration pattern so that one can get the pattern easily. Moreover, the out of phase vibration is robust to the imperfection which is unavoidable in MEMS fabrication process.

Next, a coupling problem is another main issue in MEMS gyroscopes. In the conventional MEMS gyroscopes, the frequency of the drive mode and the sense mode should be in close match for high accuracy. However, even small imperfection may cause

a coupling problem between the drive and the sense modes, and it finally prevents high precision of the gyroscope. For the parametric excitation we use the drive frequency away from the sense frequency and it may reduce the coupling problem.

Consequently, the parametric excitation can be applied to the MEMS tuning fork gyroscope design. We expect this method can reduce the fabricate costs and increase the precision of the MEMS tuning fork gyroscope.

However, we found that there are some practical problems to be solved before applying to the real system. Non-ideal energy source is one of the main issues to be solved, and the characteristics of the parameters need to be studied in more detail to guarantee the reliability of the gyroscope. Another issue to be studied is that the nonlinear phenomenon which is different from the result of the single cantilever beam case. We gave a brief explanation for the reason, but it still needs more detailed relationship among the parameters. For the future work, more research should be performed in this field to reveal the hidden secrets in the tuning fork beam.

APPENDIX

Parametrically excited pendulum by prescribed force amplitude

A.1 Equation of motion

In Chapter 6, we compared the experimental results with the theory including limited shaker power effect. The assumption that the limited shaker power induces a damping effect by the parametric resonance of the tines of the tuning fork beam is in good qualitative agreement with the experiment results. However, we noticed that there still exist some discrepancies between the theory and the experiment regarding the base movement. As shown in (b) figures from Figs. 6.6 to 6.10, there are some discrepancies between the theory and the experiment when the excitation frequency becomes higher than 80.40 Hz, the frequency inducing the parametric resonance. In this section, we discuss the relationship between the base excitation amplitude and the forcing amplitude using simplified pendulum model.

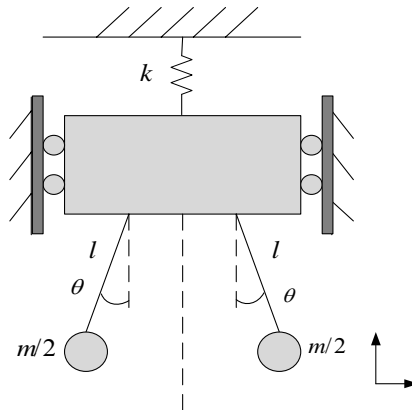


Figure A. 1 Simplified pendulum model

The illustration in Fig. A.1 shows the simplified pendulum model. Since we are interested in the relationship between the pendulum swing in horizontal direction and the corresponding displacement of the base mass in vertical direction, we assume the two pendulums are hung by the same rods, and they have the same masses for simplification. In addition, the two pendulums are assumed to swing in the opposite direction which is 180 degree out-of-phase. In other words, each pendulum swing motion can be expressed by a simple substitution for angle θ with $-\theta$. This assumption is needed because assuming that the x -direction movement is fully constrained, shown in Fig.1, makes the two pendulums decoupled.

By the same methods in Chapter 3, we can derive the kinetic Energy T and the potential energy V .

$$T = \frac{1}{2} M \dot{y}^2 + \frac{1}{2} m [\dot{y}^2 + (l \dot{\theta})^2 + 2 \dot{y} l \sin \theta \dot{\theta}] \quad (\text{A.1.1})$$

$$V = Mgy + mg(y + l - l \cos \theta) \quad (\text{A.1.2})$$

From Lagrange equation, we get the governing equations regarding y and θ variables

$$\left(\frac{m+M}{m} \right) \left(\frac{\ddot{y}}{l} \right) + \sin \theta \ddot{\theta} + \cos \theta \dot{\theta}^2 + \tilde{c} \left(\frac{\dot{y}}{l} \right) + k \left(\frac{y}{l} \right) = Q_y \quad (\text{A.1.3})$$

$$\sin \theta \left(\frac{\ddot{y}}{l} \right) + \ddot{\theta} + \tilde{c} \dot{\theta} + \frac{g}{l} \sin \theta = 0 \quad (\text{A.1.4})$$

where \tilde{c} denotes the damping coefficient.

If we assume $Y = \left(\frac{y}{l} \right)$, $\frac{m+M}{m} = 1 + \rho$, and $\frac{g}{l} = \omega_\theta^2 = 1$, we get the simplified

dimensionless equations as follows:

$$(1 + \rho) \ddot{Y} + \sin \theta \ddot{\theta} + \cos \theta \dot{\theta}^2 + \tilde{c} \dot{Y} + kY = \tilde{Q}_y \quad (\text{A.1.5})$$

$$\sin \theta \ddot{Y} + \ddot{\theta} + \tilde{c} \dot{\theta} + \sin \theta = 0 \quad (\text{A.1.6})$$

where \tilde{Q}_y represents the sinusoidal parametric excitation force. For simplification, we let $\sin \theta \approx \theta$ and $\cos \theta \approx 1$ for the combined terms with derivatives and $\sin \theta \approx \theta - \frac{\theta^3}{6}$ for the remained sine term. We get the simplified equations of motion as follows:

$$(1 + \rho) \ddot{Y} + \theta \ddot{\theta} + \dot{\theta}^2 + \tilde{c} \dot{Y} + kY = \tilde{Q}_y \quad (\text{A.1.7})$$

$$\theta \ddot{Y} + \ddot{\theta} + \tilde{c} \dot{\theta} + \theta - \frac{\theta^3}{6} = 0 \quad (\text{A.1.8})$$

A.2 Steady state response

In this section, we discuss the steady state response using harmonic balance method. The method has a long history, to interpret the behavior of many engineering applications. The standard harmonic balance method for approximating periodic solutions of a nonlinear ordinary differential equation involves the following steps:

First, select a trial solution which is a truncated Fourier series, either with terms $a_n \cos(n\omega t)$ alone, n up to N , or with both sine and cosine terms, as appropriate. Substitute this solution into the equation, and ignore any higher harmonics generated by the nonlinear terms.

Second, set equal to zero the coefficients of the retained harmonics, thus obtaining a set of coupled nonlinear equations for the frequency ω and the amplitude a_n in the trial solution. Solve these equations.

Since we are interested in the amplitude of the base motion and the pendulum motion, we let the trial solutions for the base excitation and the pendulum motion as follows:

$$Y = \frac{A}{4\omega^2} \cos 2\omega t \quad \text{and} \quad \theta = c \cos \omega t + d \sin \omega t, \quad (\text{A.2.1})$$

where, A is the acceleration amplitude of Y direction and 2ω is the parametrically excited force frequency. The force considering phase lag can be expressed by $\tilde{Q}_y = a \cos 2\omega t + b \sin 2\omega t$. Thus, the derivatives of Eq. (A.2.1) become

$$\begin{aligned} \dot{Y} &= -A \sin 2\omega t / (2\omega), \quad \ddot{Y} = -A \cos 2\omega t \\ \dot{\theta} &= -c\omega \sin \omega t + d\omega \cos \omega t, \quad \ddot{\theta} = -c\omega^2 \cos \omega t - d\omega^2 \sin \omega t \end{aligned} \quad (\text{A.2.2})$$

The coefficient of $\cos 2\omega t$ after substituting Eqs. (A.2.1) and (A.2.2) into Eq. (A.1.7) leads to

$$a = Ak - 4A\omega^2 - 4A\rho\omega^2 - 4c^2\omega^4 + 4d^2\omega^4 / (4\omega^2) \quad (\text{A.2.3})$$

Moreover, the coefficient of $\sin 2\omega t$ in Eq. (A.1.7) after the same procedure becomes

$$b = -2A\tilde{c}\omega - 8cd\omega^4 / (4\omega^2) \quad (\text{A.2.4})$$

For the θ equation, we get the simplified form by substituting Eqs. (A.2.1) and (A.2.2) into Eq. (A.1.8). After the calculation, we disregard the high frequency terms such as $\sin 3\omega t$ and $\cos 3\omega t$, then the coefficient of $\cos \omega t$ yields

$$\frac{1}{24} (24c - 12Ac - 3c^3 - 3cd^2 - 24c\omega^2 + 48d\omega\zeta) = 0 \quad (\text{A.2.5})$$

and the coefficient of $\sin \omega t$ becomes

$$\frac{1}{24} (24d + 12Ad - 3c^2d - 3d^3 - 24d\omega^2 - 48c\omega\zeta) = 0 \quad (\text{A.2.6})$$

Recall that the coefficients c and d represent the response of the pendulum. We use

algebraic techniques to get the coefficients. First, we use Eq.(A.2.5) $\times r \cos \phi$ + Eq.(A.2.6) $\times r \sin \phi$, and it gives us

$$-\frac{1}{8}r^2(r^2 + 8(-1 + \omega^2) + 4A \cos 2\phi) = 0 \quad (\text{A.2.7})$$

Next, we perform Eq.(A.2.5) $\times r \sin \phi$ - Eq.(A.2.6) $\times r \cos \phi$, and we get

$$r^2(2\omega\zeta - A \cos \phi \sin \phi) = 0 \quad (\text{A.2.8})$$

Solving Eqs. (A.2.7) and (A.2.8), we get

$$\cos 2\phi = \frac{r^2 + 8\omega^2 - 8}{4A} \quad (\text{A.2.9})$$

$$\sin 2\phi = \frac{4\omega\zeta}{A} \quad (\text{A.2.10})$$

If we raise Eqs. (A.2.9) and (A.2.10) to the second power and sum up together, we have

$$A^2 = \frac{r^4}{16} + r^2(-1 + \omega^2) + 4\{1 + \omega^4 + \omega^2(-2 + 4\zeta^2)\} \quad (\text{A.2.11})$$

Equation (A.2.11) gives the relationship between the amplitude of the base motion and the amplitude of the pendulum.

On the other hand, let us bring the force equation (A.2.3) and (A.2.4) and apply some algebraic techniques. We raise Eqs. (A.2.3) and (A.2.4) to the second power, let $c = r \cos \phi$ and $d = r \sin \phi$, and substitute Eqs. (A.2.9) and (A.2.10), we get

$$\begin{aligned} a^2 + b^2 = & \frac{1}{16\omega^4} [A^2 \{k^2 - 8k(1 + \rho)\omega^2 + 4\omega^2 \{\tilde{c}^2 + 4(1 + \rho)^2 \omega^2\}\} + \\ & 2r^2 \omega^4 \{k \{r^2 + 8(\omega^2 - 1)\} + 4\omega^2 \{r^2(2\omega^2 - \rho - 1) - 8(\omega^2 + \rho\omega^2 - \tilde{c}\zeta - \rho - 1)\}\}] \end{aligned} \quad (\text{A.2.12})$$

Equation (A.2.12) gives the relationship between the forcing amplitude $\sqrt{a^2 + b^2}$

and the base acceleration amplitude A . Therefore, if we subtract Eq. (A.2.12) from the square of the y -direction acceleration, we get the second power of the differences between the applied force and the real acceleration response as the different frequencies. On the other hand, if we assume the pendulums rest in the original location without swinging, $r = 0$, equation (A.2.12) becomes

$$a^2 + b^2 = A^2[k^2 - 8k(1 + \rho)\omega^2 + 4\omega^2\{\tilde{c}^2 + 4(1 + \rho)^2\omega^2\}]/(16\omega^4) \quad (\text{A.2.13})$$

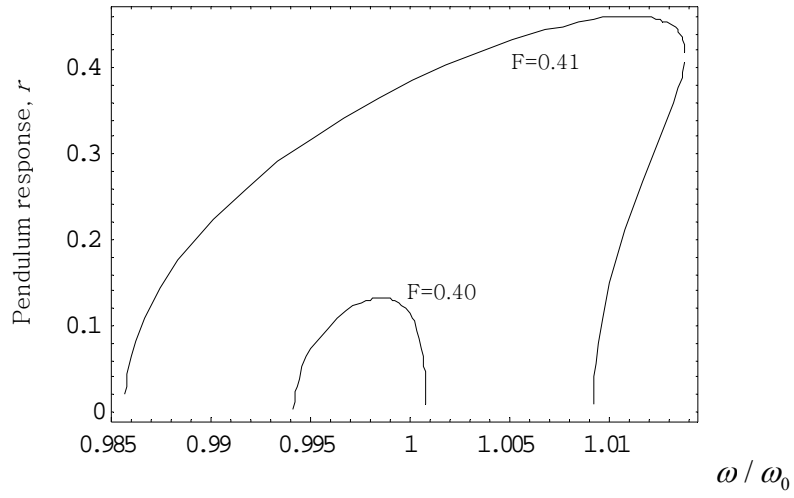


Figure A. 2 the response of the pendulum with a large pendulum mass:

$\rho=1$, $\zeta=0.05$, $\tilde{c}=0.1$, $k=0.01$, force amplitude =0.40 and 0.41

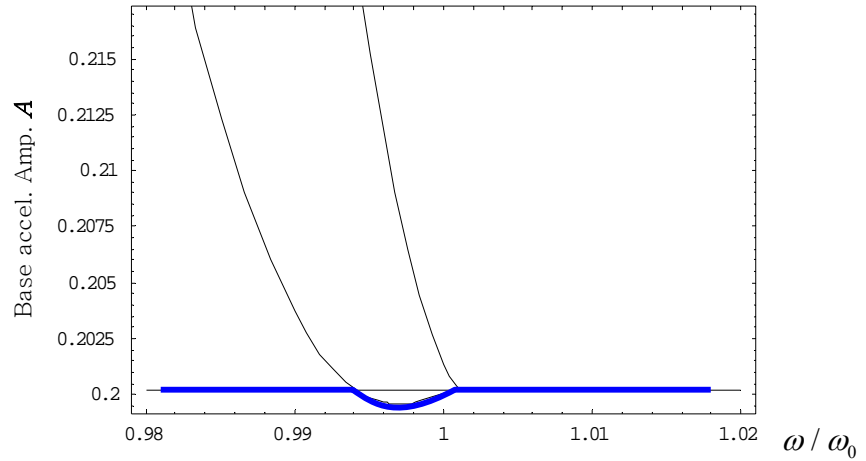


Figure A. 3 the base acceleration amplitude when pendulums are swinging with a large pendulum

mass: $\rho=1$, $\zeta=0.05$, $\tilde{c}=0.1$, $k=0.01$, force amplitude =0.40

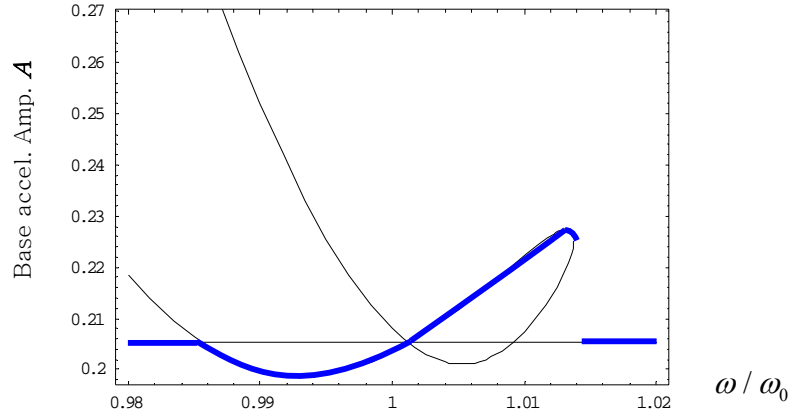


Figure A. 4 the base acceleration amplitude when pendulums are swinging with a large pendulum mass: $\rho=1$, $\zeta=0.05$, $\tilde{c}=0.1$, $k=0.01$, force amplitude =0.41

Figure A.2 shows the responses of the pendulums with two different force amplitudes, and their corresponding base acceleration amplitudes are illustrated in Figs. A.3 and A.4. Both the cases, large pendulum masses are used, $\rho = 1$, which means the total pendulum mass is the same as the base mass. As illustrated in Fig. A.3, when the force amplitude is 0.40, we see the amplitude of the base response is reduced during the pendulums swing. However, when the force amplitude is 0.41, as shown in Fig. A.4, we see the amplitude of the base excitation is not reduced in all the frequency range even though the pendulums are swinging.

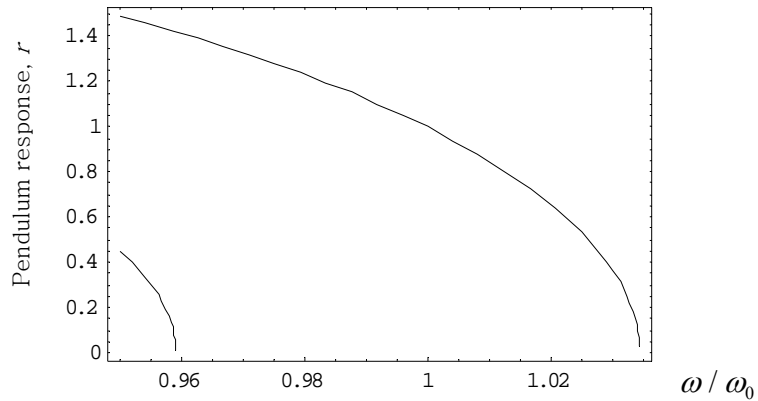


Figure A. 5 the response of the pendulum with a small pendulum mass: $\rho=9$, $\zeta=0.05$, $\tilde{c}=0.1$, $k=0.01$, force amplitude =2.5

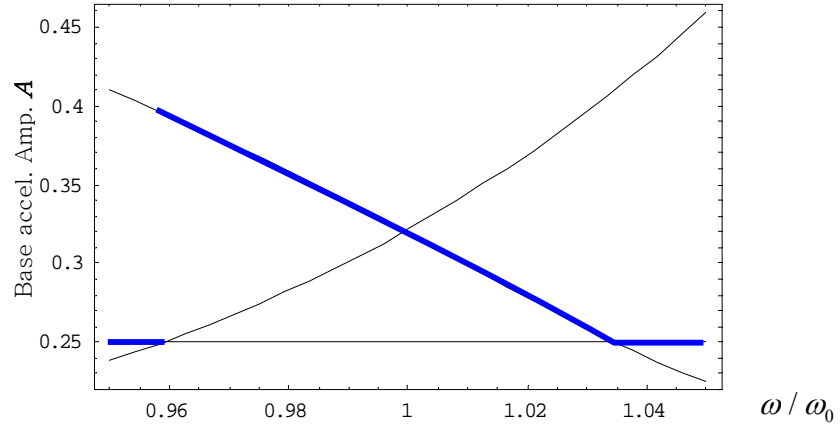


Figure A. 6 the base acceleration amplitude when pendulums are swinging with a small pendulum mass: $\rho=9$, $\zeta=0.05$, $\tilde{c}=0.1$, $k=0.01$, force amplitude =2.5

Figs. A.5 and A.6 show the simulation results with small pendulum masses, $\rho = 9$, which means the base mass is greater than the total pendulum mass by 9 times. In this case, the pendulum response shows softening nonlinearity as shown in Fig. A.5. The corresponding amplitude of the base acceleration is illustrated in Fig. A.6. As shown in the figure, the amplitude of the base acceleration becomes even larger while the pendulums are swinging. We obtained the same result from the numerical simulation by MATLAB program.

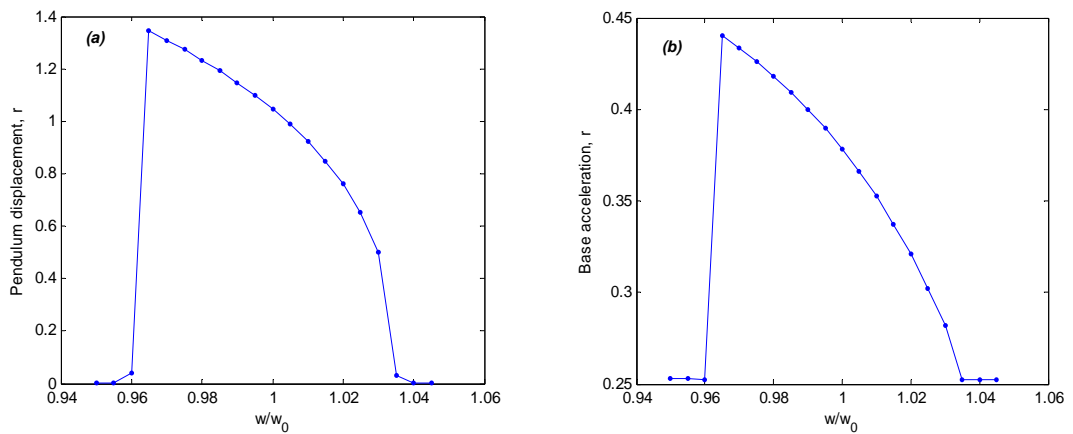


Figure A. 7 the MATLAB simulation results from the original equations used in Chapter 3; (a) pendulum displacement (b) base acceleration: $\alpha = \beta = 0.09$, $\zeta = 0.05$, $A = 0.25$

Figure 7 is the MATLAB simulation results for which we used the original pendulum equations used in Chapter 3. For the simulation, a large mass ratio was used; each pendulum has the mass $1/10$ of the base mass. In addition, the amplitude of the force used for the simulation was 0.25. Since the equations for Mathematica is simplified, it is not the same as original MATLAB program used in Chapter 3 so that it is hard to find exact matching parameters; however, the results show qualitatively good agreement.

This result is not exactly same as our experiment because our experiment carried out for a tuning fork beam instead of the pendulum model. As shown in Figs. A.2 through A.4, the pendulum response shows hardening nonlinearity with a large pendulum mass, while our experiment with tuning fork beam shows softening nonlinearity as shown in Chapters 5 and 6. However, at least, we noticed that the damping effect on the base excitation from the pendulum or the tines of the tuning fork beam is not always consistent. This is little new phenomenon from well known non-linear vibration absorbers; Vyas and Bajaj [41] studied auto-parametric vibration absorbers using multiple pendulums and got a conclusion that the pendulums can reduce the base vibration in all the range in which the pendulums swing. However, our work shows that there exists certain range in which the amplitude of the base acceleration gets increased. Furthermore, with a small pendulum mass, the base acceleration gets increased in all the frequency range in which the pendulums are still swinging. In other words, the absorber may not reduce the amplitude of vibration properly; the situation may be worse. Because of this reason, both the cases, a tuning fork beam and a pendulum, should be studied more in the future to apply to real system such as gyroscopes or absorbers.

A.3. Programs used in the simulation

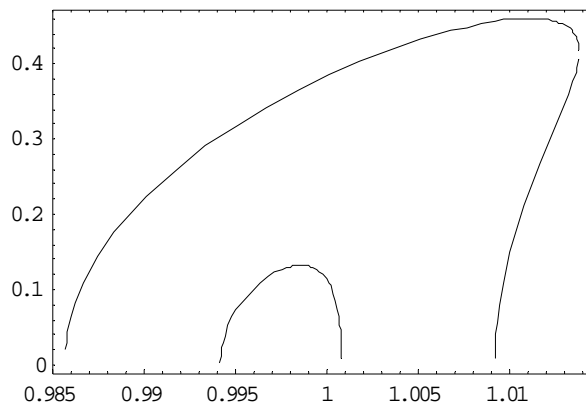
A.3.1 Mathematica program for the analytic solution

```
k=.; c=.;  
y=A Cos[2 w t]/(4w^2); th=C Cos[w t]+ D Sin[w t];  
sinth=th-th^3/6; costh=1; thd=D[th,t]; thdd=D[thd,t];  
yd=D[y,t]; ydd=D[yd,t];  
yeq=TrigReduce[(1+rho)ydd+c yd+k y+(th thdd+costh thd^2)-a Cos[2 w t]-b Sin[2 w t]]  
eq1=Coefficient[yeq,Cos[2 t w]]  
eq2=Coefficient[yeq,Sin[2 t w]]  
theq=TrigReduce[thdd+ydd th+sinth+2zeta thd]  
eq3=Coefficient[theq,Cos[t w]]  
eq4=Coefficient[theq,Sin[t w]]  
eqq3=Simplify[eq3*C+eq4*D/.{C→r Cos[phi],D→r Sin[phi]}]  
eqq4=Simplify[eq3*D-eq4*C/.{C→r Cos[phi],D→r Sin[phi]}]  
temp1=eqq3/.{Cos[2phi]→xc}  
temp2=eqq4/.{Cos[phi] Sin[phi]→xs/2}  
so2=Solve[temp2==0,xs][[1,1]]  
so1=Solve[temp1==0,xc][[1,1]]  
Eq=Expand[A^2(xs^2+xc^2-1)/. {so1,so2}]  
A2=Simplify[A^2+Eq];(* A^2 *)  
eqa=TrigReduce[a+eq1/.{C→r Cos[phi],D→r Sin[phi]}]/. {Cos[2phi]→xc}  
eqb=TrigReduce[b+eq2/.{C→r Cos[phi],D→r Sin[phi]}]/. {Sin[2phi]→xs}  
amp2=Simplify[Simplify[Expand[eqa^2+eqb^2]/. {xc^2→1-xs^2}]/. {so1,so2}]  
ampA20=Simplify[amp2/.r→0]
```

```

tem=ampA20/.A^2→aa2
sol=Solve[tem==forceamp^2,aa2]
BaseAmp0=forceamp*Sqrt[A^2/ampA20]
ampr=Simplify[amp2/.{A^2→A2}]
Eqr2=ampr-forceamp^2/.{r^2→r2,r^4→r2^2}
sl=Solve[Eqr2==0,r2];
ampr1=Sqrt[r2/.sl[[1]]];
ampr2=Sqrt[r2/.sl[[2]]];
g1=Plot[ampr1/.{rho→1,zeta→0.05,c→0.1,k→0.01,forceamp→0.40},{w,0.98,1.02}];
g2=Plot[ampr2/.{rho→1,zeta→0.05,c→0.1,k→0.01,forceamp→0.40},{w,0.98,1.02}];
g21=Plot[ampr1/.{rho→1,zeta→0.05,c→0.1,k→0.01,forceamp→0.41},{w,0.98,1.02}];
g22=Plot[ampr2/.{rho→1,zeta→0.05,c→0.1,k→0.01,forceamp→0.41},{w,0.98,1.02}];
Show[g1,g2,g21,g22,Axes→False,Frame→True];

```



```

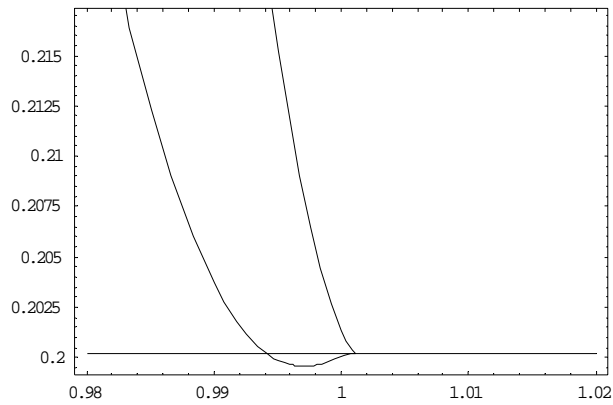
A22=A2/.{r^2→r2,r^4→r2^2}
BaseAmp1=Sqrt[A22/.sl[[1]]];
BaseAmp2=Sqrt[A22/.sl[[2]]];
gr1=Plot[BaseAmp1/.{rho→1,zeta→0.05,c→0.1,k→0.01,forceamp→0.40},{w,0.98,1.02}];
gr2=Plot[BaseAmp2/.{rho→1,zeta→0.05,c→0.1,k→0.01,forceamp→0.40},{w,0.98,1.02}];
gr3=Plot[BaseAmp0/.{rho→1,zeta→0.05,c→0.1,k→0.01,forceamp→0.40},{w,0.98,1.02}];

```

```

gr21=Plot[BaseAmp1/.{rho→1,zeta→0.05,c→0.1,k→0.01,forceamp→0.41},{w,0.98,1.02}];
gr22=Plot[BaseAmp2/.{rho→1,zeta→0.05,c→0.1,k→0.01,forceamp→0.41},{w,0.98,1.02}];
gr23=Plot[BaseAmp0/.{rho→1,zeta→0.05,c→0.1,k→0.01,forceamp→0.41},{w,0.98,1.02}];
Show[gr1,gr2,gr3,Axes→False,Frame→True];

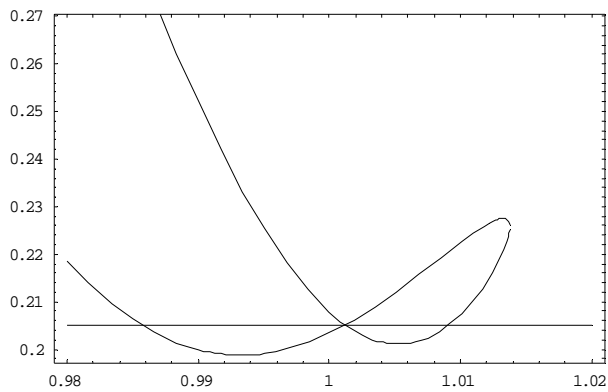
```



```

Show[gr21,gr22,gr23,Axes→False,Frame→True];

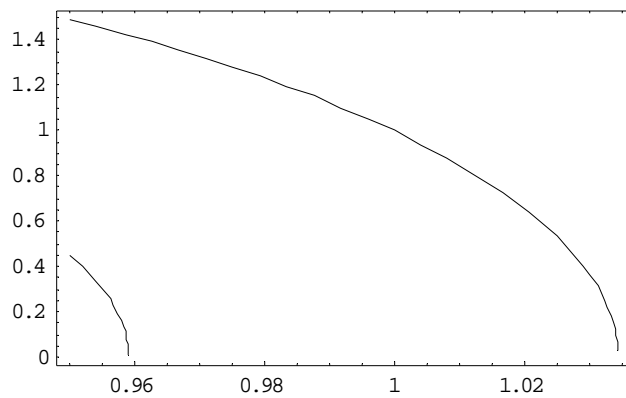
```



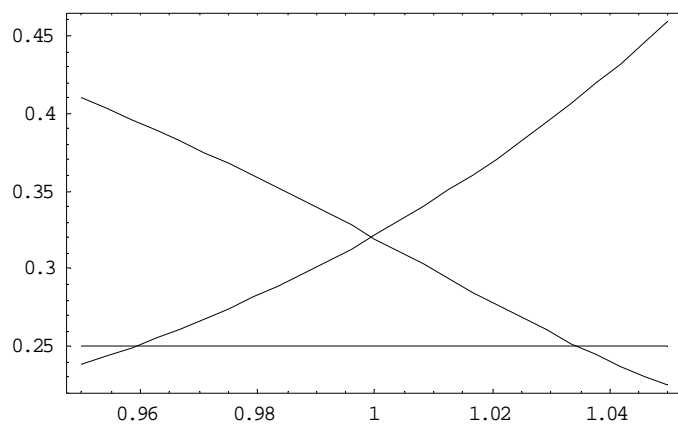
```

g1=Plot[ampr1/.{rho→9,zeta→0.05,c→0.1,k→0.01,forceamp→2.5},{w,0.95,1.05}];
g2=Plot[ampr2/.{rho→9,zeta→0.05,c→0.1,k→0.01,forceamp→2.5},{w,0.95,1.05}];
Show[g1,g2,Axes→False,Frame→True];

```



```
gr1=Plot[BaseAmp1/.{rho→9,zeta→0.05,c→0.1,k→0.01,forceamp→2.5},{w,0.95,1.05}];
gr2=Plot[BaseAmp2/.{rho→9,zeta→0.05,c→0.1,k→0.01,forceamp→2.5},{w,0.95,1.05}];
gr3=Plot[BaseAmp0/.{rho→9,zeta→0.05,c→0.1,k→0.01,forceamp→2.5},{w,0.95,1.05}];
Show[gr1,gr2,gr3,Axes→False,Frame→True];
```



A.3.2 MATLAB programs for the numerical solution

A.3.2.1 Main program

```
clear all
close all
global alpa beta gamma jeta A wr w12 w1x w1y; % w12=w2/w1, w1x=wx/w1, w1y=wy/w1

alpa=0.09; beta=0.09; gamma=1; jeta=0.05;
A=0.25;

w12=1; w1x=10; w1y=0.2;
t=0;

fn=20;
for n=1:fn
    wr=1-0.05+0.005*(n-1)
    Mwr(n)=wr;
    y=[0 0 0 0 0.01 0 -0.01 0]; % initial condition
    tfinal=4000;
    totalsteps=tfinal*10;
    tstep=tfinal/totalsteps;
    for i=1:totalsteps;
        tspan=[(i-1)*tstep i*tstep];
        [t, sol]=ode45('nondimenoriginalsub', tspan,y);
        y=sol(length(sol),:);
        T(i)=t(length(t));
        Y(i,:)=y;
        effi=39000;
        if i>effi
            ydisp(i-effi)=y(3)*4*wr^2;
            theta(i-effi)=y(5);
        end
    end
end

maxy(n)=max(ydisp);
miny(n)=min(ydisp);
```

```

        yptp(n)=(maxy(n)-miny(n))/2;
        maxtheta(n)=max(theta);
        mintheta(n)=min(theta);
        thetaptp(n)=(maxtheta(n)-mintheta(n))/2;
figure(n)
subplot(4,1,1);
plot(T,Y(:,1)); xlabel('Time(sec)') ; ylabel('displacement(x)');
subplot(4,1,2);
plot(T,Y(:,2)); xlabel('Time(sec)') ; ylabel('x-prime');
subplot(4,1,3);
plot(T,Y(:,3)); xlabel('Time(sec)') ; ylabel('displacement(y)');
subplot(4,1,4);
plot(T,Y(:,4)); xlabel('Time(sec)') ; ylabel('y-prime');

figure(n+20)
subplot(4,1,1);
plot(T,Y(:,5)); xlabel('Time(sec)') ; ylabel('displacement(theta1)');
subplot(4,1,2);
plot(T,Y(:,6)); xlabel('Time(sec)') ; ylabel('th1-prime');
subplot(4,1,3);
plot(T,Y(:,7)); xlabel('Time(sec)') ; ylabel('displacement(theta2)');
subplot(4,1,4);
plot(T,Y(:,8)); xlabel('Time(sec)') ; ylabel('th2-prime');
end

figure(100)
plot(Mwr,yptp)
figure(101)
plot(Mwr,thetaptp)

```

A.3.2.1 Sub program

```

function sol=nondimenoriginalsub(t,y)

global alpa beta gamma jeta A wr w12 w1x w1y

```

```

M=[ 1  0  alpa*cos(y(5))  beta*gamma*cos(y(7)) ;
    0  1  alpa*sin(y(5))  beta*gamma*sin(y(7));
    cos(y(5))  sin(y(5))  1  0;
    cos(y(7))  sin(y(7))  0  gamma ];

C=[2*jeta*w1x  0  -alpa*sin(y(5))*y(6)  -beta*gamma*sin(y(7))*y(8);
    0  2*jeta*w1y  alpa*cos(y(5))*y(6)  beta*gamma*cos(y(7))*y(8);
    0  0  2*jeta  0 ;
    0  0  0  2*jeta*gamma*w12];

K=[w1x^2*y(1); w1y^2*y(3); sin(y(5)) ; sin(y(7)) ];

Q=[0;-A*cos(2*wr*t);0;0];

Coord=[y(2);y(4);y(6);y(8)];

Dd=-inv(M)*C*Coord-inv(M)*K+inv(M)*Q;

s1=y(2); s2=Dd(1); s3=y(4); s4=Dd(2); s5=y(6); s6=Dd(3); s7=y(8); s8=Dd(4);

sol=[s1;s2;s3;s4;s5;s6;s7;s8];

```


REFERENCES

1. Yazdi, N., Ayazi, F., and Najafi, K. "Micro machined inertial sensors." Proceedings of IEEE, Vol. 86, No. 8. 1998. pp 1640-1659
2. Lefevre, H. "The Fiber Optic Gyroscope". Norwood, MA: Artech House. 1993
3. Lawrence, A. "Modern Inertial Technology: Navigation, Guidance, and Control". New York: Springer Verlag. 1993
4. Titterton, D.H. and Weston, J.L. "Strapdown inertial navigation technology second edition" The American institute of aeronautics and astronautics, 2004
5. Boxenhorn, B. "A vibratory micromechanical gyroscope." AIAA Guidance and Control Conference, Minneapolis, MN. Aug. 15-17. 1988. pp 10-33
6. Greiff, P., Boxenhorn, B., King, T. and Niles, L. "Silicon monolithic micromechanical gyroscope." Transducers 91 Technical Digest, 1991 International Conference on Solid State Sensors and Actuators. June 24. 1991. pp 966-968
7. Bernstein, J., Cho, S., King, A.T., Kourepenis, A., Maciel, P., and Weinberg, M. "A micro machined comb-drive tuning fork rate gyroscope." in Proc. IEEE Micro Electro Mechanical Systems Workshop (MEMS'93), Fort Lauderdale, FL. Feb. 1993. pp 143-148
8. M. Weinberg, J. Bernstein, S. Cho, A. T. King, A. Kourepenis, P. Ward, and J. Sohn. "A micro machined comb-drive tuning fork gyroscope for commercial applications." Proc. Sensor Expo, Cleveland, OH. 1994. pp 187-193
9. K. Maenaka and T. Shiozawa. "A study of silicon angular rate sensors using anisotropic etching technology." Sensors Actuators A, vol. 43. 1994. pp 72-77
10. M. W. Putty and K. Najafi. "A micro machined vibrating ring gyroscope." Tech. Dig. Solid State Sens. Actuator Workshop, Hilton Head Island, SC. June. 1994. pp 213-220
11. H. Xie and G. K. Fedder. "A CMOS MEMS lateral axis gyroscope." Proc. 14th IEEE Int. Conf. Micro electro mechanical Systems, Interlaken, Switzerland. Jan. 2001. pp 162-165
12. J.A. Geen. "A Path to Low Cost Gyroscope." Solid State Sensor and Actuator Workshop, HiltonHead, SJ. 1998. pp 51-54

13. Y. Mochida, M. Tamura, and K. Ohwada. "Micro machined Vibrating Rate Gyroscope with Independent Beams for Drive and Detection Modes." *Sensors and Actuators A*, Vol. 80. 2000. pp 170-178
14. M. Niu, W. Xue, X. Wang, J. Xie, G. Yang, and W. Wang. "Design and Characteristics of Two Gimbals Micro Gyroscopes Fabricated with Quasi LIGA Process." *International Conference on Solid State Sensor and Actuators*. 1997. pp 891-894
15. U. Breng, W. Guttman, P. Leinfelder, B. Ryrko, S. Zimmermann, D. Billep, T. Gessner, K. Hillner, and M. Weimer. "Bulk Micro machined Gyroscope Based on Coupled Resonators." *International Conference on Solid State Sensor and Actuators*, Japan. 1999. pp 1570-1573
16. S.E. Alper, and T. Akin. "A Symmetric Surface Micromachined Gyroscope with Decoupled Oscillation Modes." *Sensors and Actuators A*, Vol. 97. 2002. pp 347-358
17. H. Guerrero. "Evolution and trends in micro sensors." *Micromachine devices*, 4. 1999. pp 12-14
18. Clark, W. A., Howe, R. T., and Horowitz, R. "Surface micro machined Z axis vibratory rate gyroscope." *Technical Digest. Solid State Sensor and Actuator Workshop*, Hilton Head Island, S.C. June. 1996. pp 283-287
19. Juneau, T., Pisano, A. P., and Smith, J. H. "Dual axis operation of a micro machined rate gyroscope." *Proc., IEEE 1997 Int. Conf. on Solid State Sensors and Actuators (Transducers `97)*, Chicago. June. 1997. pp 883-886
20. M. Lutz, W. Golderer, J. Gerstenmeier, J. Marek, B. Maihofer, S. Mahler, H. Munzel, and U. Bischof. "A precision yaw rate sensor in silicon micromachining." *Transducers 1997*, Chicago, IL. June. 1997. pp 847-850
21. R. Voss, K. Bauer, W. Ficker, T. Gleissner, W. Kupke, M. Rose, S. Sassen, J. Schalk, H. Seidel, and E. Stenzel. "Silicon angular rate sensor for automotive applications with piezoelectric drive and piezo resistive readout." *Tech. Dig. 9th Int. Conf. Solid State Sensors and Actuators (Transducers `97)*, Chicago, IL. June. 1997. pp 879-882
22. A. Kourepenis, J. Bernstein, J. Connely, R. Elliot, P. Ward, and M. Weinberg. "Performance of MEMS inertial sensors." *Proc. IEEE Position Location and Navigation Symposium*. 1998. pp 1-8
23. Mochida, Y., Tamura, M., and Ohwada, K. "A micro machined vibrating rate gyroscope with independent beams for the drive and detection modes." *Proc., Twelfth IEEE Int. Conf. on Micro Electro Mechanical Systems (MEMS `99)*, Orlando, FL. Jan. 1999. pp 618-623

24. Park, K. Y., Jeong, H. S., An, S., Shin, S. H., and Lee, C. W. "Lateral gyroscope suspended by two gimbals through high aspect ratio ICP etching." Proc., IEEE 1999 Int. Conf. on Solid State Sensors and Actuators (Transducers '99), Sendai, Japan. June. 1999. pp 972-975
25. S. Lee, S. Park, J. Kim, and D. Cho. "Surface/bulk micro machined single crystalline silicon micro gyroscope." IEEE/ASME Journal of Micro electromechanical Systems, Vol.9, No.4. Dec. 2000. pp 557-567
26. W. Geiger, W.U. Butt, A. Gaisser, J. Fretch, M. Braxmaier, T. Link, A. Kohne, P. Nommensen, H. Sandmaier, and W. Lang. "Decoupled Microgyros and the Design Principle DAVED." Sensors and Actuators (Physical), Vol. A95, No.23. Jan. 2002. pp 239-249
27. J. A. Geen, S. J. Sherman, J. F. Chang, and S. R. Lewis. "Single chip surface micromachining integrated gyroscope with 50 deg/hour root Allan variance". Dig. IEEE Int. Solid State Circuits Conf., San Francisco, CA. Feb. 2002. pp 426-427
28. H. Xie and G. K. Fedder. "Fabrication, Characterization, and Analysis of a DRIE CMOS MEMS Gyroscope." IEEE Sensors Journal, Vol. 3, No. 5. 2003. pp 622-631
29. A. H. Nayfeh and D. T. Mook. "Nonlinear Oscillations." Wiley-Interscience. New York. 1979
30. R.M. Evan-Ivanowski. " Resonance oscillations in Mechanical systems." Elsevier Scientific Publishing Company. Oxford, New York. 1976
31. M. Faraday. "On a peculiar class of acoustical figures and on certain forms assumed by a group of particles upon vibrating elastic surfaces." Philosophical Transactions of the Royal Society of London. 1831. pp 299-318
32. Stephenson, A. "On a new type of dynamical stability." Mem. Proc. Manch. Lit. Phil. Soc., 52. 1908. pp 259-267
33. Beliaev, N. M. "Stability of prismatic rods, subject to variable longitudinal forces." Collection of papers: Eng. Construct. Struct. Mech., Leningrad.1924. pp 149-167,259,267
34. McLachlan, N. W. "Theory and Application of Mathieu Functions." Oxford University press. New York. 1947
35. Bondarenko, G. V. "The Hill Differential Equation and its uses in Engineering Vibration Problems." Akademiia Nauk SSSR. Moscow. 1936. pp259-295
36. Magnus, W., and S. Winkler "Hill's Equation." Wiley, New York. 1966

37. Bolotin, V. V. "The Dynamic Stability of Elastic systems." Holden Day. San Francisco. 1964
38. Shtokalo, I. Z. "Linear Differential Equations with Variable Coefficients." Gordon and Breach. New York. 1961
39. R. A. Ibrahim. "Parametric Random Vibration." Wiley-Interscience. New York. 1985
40. M. Gürgöze. "Parametric vibrations of a restrained beam with an end mass under displacement excitation." Journal of Sound and Vibration 108. 1986. pp 73-84
41. A. Vyas and A. K. Bajaj. "Dynamics of autoparametric vibration absorbers using multiple pendulums." Journal of Sound and Vibration, 246(1). 2001. pp 115-135
42. Eugene I. Butikov. "Parametric Resonance in a Linear Oscillator at Square wave modulation." Institute of Physics Publishing, Eur. J. Phys. 26. 2005. pp 157-174
43. Mandelstam, L., and N. Papalexi. "On the establishment of vibrations according to a resonance of the nth form." J. of Tech. Phys., 4. 1934. pp 67-77
44. Moon, F. C. "Chaotic Vibrations-An Introduction for Applied Scientists and Engineers." Wiley. New York. 1987.
45. Pramod Malatkar. "Nonlinear vibrations of cantilever beams and plates." Ph. D. thesis, Virginia Polytechnic Institute and State University, Blacksburg Virginia. 2003
46. A. H. Nayfeh and P. Frank Pai. "Non-linear non-planar parametric responses of an inextensional beam." Int. J. Non-linear Mechanics, Vol. 24, No. 2. 1989. pp 139-158
47. Stephen P. Timoshenko. "Theory of Elastic Stability." McGRAW-Hill. New York. 1961
48. www.algor.com
49. www.spss.com
50. Daniel J. Inman. "Engineering Vibration." Prentice hall, Englewood Cliffs, New Jersey. 1996
51. Ferdinand Verhulst. "Nonlinear Differential Equations and Dynamical Systems." Springer. 1996
52. International Alloy Designations and Chemical Composition Limits for Wrought Aluminum and Wrought Aluminum Alloys (Revised 2001)

- 53. EVaRT 4.0 user's Manual. Santa Rosa, CA.
- 54. www.motionanalysis.com
- 55. Yongsik Lee and Z. C. Feng. "Feasibility study of parametric excitations of a tuning fork microgyroscope." Proceedings of IMECE 2004.
- 56. A. H. Nayfeh and P.F. Pai. "Non-linear non-planar parametric responses of an inextensional beam." Int. J. Non-linear Mechanics, Vol. 24. No. 2. 1989. pp 139-158
- 57. T.J. Anderson, A.H. Nayfeh, and B. Balachandran. "Experimental verification of the importance of the nonlinear curvature in the response of cantilever beam." Journal of Vibration and Acoustics, Vol. 118. 1996. pp 21-27
- 58. J. Dugundji and V. Mukhopadhyay. "Lateral bending-torsion vibrations of a thin beam under parametric excitation." Journal of applied Mechanics. Sept. 1973. pp 693-698
- 59. P. Frank Pai, Lu Huang, Jiazhu Hu, and Dustin R. Langewisch. " Time-frequency method fro nonlinear system identification and damage detection." In proceeding of Journal of Structural Health Monitoring. 2007

VITA

Yongsik Lee was born on June 10, 1970 in Danyang, Korea. He graduated from Chung-ju high school in 1988 and went Korea Military Academy(KMA) to become a military officer. He received a B.S. degree at Korea Military Academy in 1992 in physics. After graduating, he served for 7 years as an active duty officer until he was selected for overseas study. He started his M.S. program in the Department of Mechanical and Aerospace Engineering at the University of Missouri-Columbia in 1999, and received his M.S. degree in 2001. Two years after M.S. degree, he was again sent to study for his Ph. D. program in the same department in 2003 and received a Ph. D. degree in 2007.